POLITECNICO DI TORINO

Dipartimento di Energia

Corso di Laurea in Ingegneria Energetica e Nucleare
progetto $Poly^2Nuc$

Tesi di Laurea Magistrale

AlF_3-moderated neutron flux characterization by means of experiments and Monte Carlo simulations for BNCT applications

POLITECNICO
DI TORINO

Relatori
prof.ssa Sandra Dulla, Politecnico di Torino
prof. Stefano Agosteo, Politecnico di Milano
prof. Saverio Altieri, Università di Pavia

Gabriele Parisi

Luglio 2019

Ringraziamenti

Vorrei ringraziare per primi la musica, il teatro e l'atletica: le mie fedeli compagne di viaggio che colorano ogni mia giornata e senza le quali sarebbe stata estremamente dura arrivare fino a questo punto "illeso". La musica per avermi fatto compagnia negli innumerevoli viaggi fra Torino e Milano e nelle nottate di studio e di scrittura, per essere una fonte di ispirazione e per diventare un insostituibile sfogo emotivo ogni volta che prendo in mano la chitarra. Il teatro per essere una fonte di creatività e un mezzo di espressione meraviglioso e per avermi fatto pensare abbastanza a lungo da capire che non sto sbagliando strada, o per lo meno non di molto. L'altetica...per avermi insegnato a mettere tutto me stesso nelle cose a cui tengo, a tirare fuori il massimo quando bisogna dare il massimo e per essere stata abbastanza infame da insegnarmi ad accettare brutte delusioni e sconfitte ma a non arrendermi mai a nessun costo.
Il ringraziamento più importante però è per Stefano, Andrea, Davide, Davide, Giovanni, Saverio, Silva e Nicoletta. Per avermi insegnato tantissimo, per la fiducia che mi hanno dato e per avermi accolto nei rispettivi gruppi e aver dato un senso a tutti i miei viaggi a Milano e a Pavia. Per l'aiuto ed i consigli nel lavoro fatto per questa tesi, che sono stati preziosissimi. In particolare, ringrazio Stefano per avermi dato la possibilità di svolgere questa tesi. Di nuovo Stefano e Giovanni per essersi fatti due nottate in bianco insieme a me ai LNL per riuscire a fare delle buone misure nonostante i capricci dell'acceleratore. Andrea, Davide, Silva e Nicoletta per aver avuto la pazienza di seguirmi passo per passo. Ian e Chiara per essere venuti a dare sostegno la settimana di misure ai LNL ed essersi fatti, insieme a Silva, una nottata al mio posto. Ancora Silva, Stefano, Andrea e Davide per avermi consigliato durante la scrittura della tesi.
Grazie! Grazie per la fiducia e per avermi fatto sentire parte dei vostri gruppi.
Voglio poi ringraziare in modo speciale mia mamma e mio papà. Senza di voi non avrei potuto fare niente di tutto quello che faccio. Grazie per il vostro sostegno e i vostri consigli, grazie per avermi cresciuto così e per credere in me. Sempre un grazie speciale è per mio fratello, Fede, che mi sopporta, mi supporta e crede in me sempre. L'ultimo ringraziamento speciale è per Nomì, per l'ammirazione e per l'entusiasmo sorprendente che hai e che mi insegni ad avere per tutte le cose. Vi voglio bene.

Ringrazio Mana, Dani e Teo per aver sopportato i miei scleri e le mie crisi e sopratutto per esserci sempre. Ringrazio Paolo, Marco, Federico, Giuseppe, Lisa, Veronica, Alì, Rino e Giulia per avermi ospitato a dormire a casa vostra a Milano in più occasioni quest'anno. In particolare Paolo, a casa di cui ormai ho lasciato lo spazzolino, e Lisa, che mi ha dato ospitalità immediata salvandomi da una nottata sotto a un ponte. Ringrazio Daniè, Vinz e Samu per il bellissimo anno di coinquilinanza milanese.
Infine ringrazio Italo, le ferrovie italiane e la stazione senza panchine di Milano centrale. Grazie ai loro sempre puntuali ritardi di una ventina di minuti, per non parlare poi dei jackpot da un'ora, una e mezza e tre ore, mi sono assicurato diversi anni senza problemi alla circolazione del sangue nelle gambe.

alla mia mamma e al mio papà,

Contents

Chapter 1

Introduction

Radiation applicaton for medical purpose is a wide and interesting field of nuclear physics. Huge efforts are made by researcher all over the world to find new applications and develop either new or improved technologies allowing the use of radiation to be useful to improve our life and health. One of the most stimulating medical application of radiation is its use to treat cancer.
Cancer is one of the most struggling disease, being one of the major causes of death today. Radiation therapies are one of the three most used cancer treatment strategies with chemotherapy and surgery. Very often the whole treatment includes a combination of two or of all the three techniques. The most widely used radiation therapy is the *radiotherapy* exploiting γ or X rays to kill tumor cells. Another strategy, very fast growing in the last decade, is the *hadron therapy*, in which ions such as protons or carbon ions are used for the tumor treatment. Neoplastic cells are killed with much higher precision than in conventional radiotherapy thanks to the way charged particles release energy in tissues. Moreover, heavy ions have higher biological effectiveness in killing cells, if compared with photons. Another very interesting and promising therapy is the *Boron Neutron Capture Therapy* (*BNCT*). On of its main features is the selectivity with which it kills tumor while sparing healthy tissue. BNCT exploits the nuclear reaction ^{10}B(n,α)^{7}Li to deliver very high linear energy transfer (LET) particles (α and ^{7}Li) to tumor tissues directly from within the cancer cells. Boron is provided to neoplastic cells using a pharmaceutical borated compound able to selectively concentrate in tumor tissue. The patient is then irradiated by a low energy neutron beam to induce the reaction with ^{10}B. As the reaction cross-section is maximum for thermal energy range ($\sim 0.025\,\mathrm{eV}$), either a thermal or epithermal (1 eV to 10 keV) neutron beam is desired for superficial or deep seated tumors respectively. The neutron beam can be obtained from either a nuclear reactor or a particle accelerator. The latter are preferred because of several reasons among which the actual possibility to install them in hospitals. Today, research is therefore mainly focused on accelerator-based BNCT. Accelerators provide a charged particle beam on a proper target that generates neutrons

through some nuclear reaction. The most used target are ^{7}Li and ^{9}Be, exploiting the reactions ^{7}Li(p,n)^{7}Be and ^{9}Bep,n^{9}B or ^{9}Be(d,n)^{10}B respectively. Such neutrons have energy spectrum in the fast energy range. They have thus to be thermalized down to epithermal or thermal energy region before being used for BNCT. A beam shaping assembly (BSA), consisting in an ensamble of moderating and collimating materials, is therefore needed.
Knowledge of the neutron energy spectrum is of main importance. Nuclear spectrometry is the nuclear engineering field concerning with the neutron detection and energy measurement. Neutron spectrometers are constructed basing on a variety of methods, one of which are recoil-nuclei spectrometers. Neutron spectrometry is an important tool in radiotherapy, radiation protection, in nuclear physics and technology and in fusion plasma diagnostics.
This thesis sets in the design and optimization of an accelerator-based BNCT, in particular in the project of a BSA for the RFQ accelerator facility built at Legnaro National Laboratories (LNL) of Istituto Nazionale di Fisica Nucleare (INFN). The goal is to obtain an epithermal neutron beam for BNCT treatment of deep-seated tumors. Postuma in [30] carried out Monte Carlo simulations to design the beam through a BSA whose bulk is aluminum tri-fluoride AlF_3. The densified material, additioned with LiF, was produced for the first time in Pavia, but no measurements had ever been conducted so far.
This thesis aims at characterizing the neutron moderation properties of AlF_3 by measuring the neutron spectra emerging after AlF_3 bricks, using a neutron source of the same characteristic as the clinical beam from RFQ accelerator. Monte Carlo simulations are performed; their comparison with experimental results constitute the first validation of the Monte Carlo calculations involving this material. Experiments are carried out at the CN accelerator of LNL, with a 5 MeV proton beam coupled with a beryllium target. Measurements give the first experimental neutron spectra obtained by solid AlF_3 with LiF. Measurements are performed using two spectrometers: the *ACSpect* spectrometer and the *DIAMON*.
The *ACSpect* is an innovative active spectrometer based on a two-stages silicon telescope coupled through a collimator with an active converter acting as scintillator too. The spectrometer is unique in its kind as it is a high energy resolution spectrometer with a very simple response function that does not need any complicate unfolding technique and it is a compact instrument easy to transport. The *ACSpect* was first implemented by the Nuclear Measurements group of the Energy department of Politecnico di Milano (Agosteo et al. [6]) and a huge improvement is made in the framework of this thesis. Whereas, the *DIAMON* is a low energy resolution neutron spectrometer developed by the Nuclear Measurements group (Energy department, PoliMi) in collaboration with *RAYLAB*, an Italian innovative start-up, spin off of Politecnico di Milano [1]. It has a low resolution but it can measure the neutron energy spectrum in a wide energy range, from thermal to high energies, giving very precise integral informations. In this work it is used

for several measurements at LNL to have a further comparison with the ACSpect measurements and with Monte Carlo calculations for the integral fluence rate, of which DIAMON provides very reliable results.

The thesis is structured in three parts: introductions (chapter 2), materials and methods (chapters 3, 4 and 5) and results (chapter 6). Chapter 2 introduces and present the state of the art of the two main research fields involved in this thesis: the BNCT, focusing on the optimal BSA studied for the Italian RFQ accelerator, which bulk material is AlF_3 and neutron spectrometry.
Chapter 3 describes in detail the *ACSpect* spectrometer, its technology and its working principle as well as the elaboration process of the measured data.
Chapter 4 describes the measurement campaign at the CN accelerator at LNL, giving details on the measurements carried out and their experimental set-up.
Chapter 5 presents how the Monte Carlo simulation work is set and performed describing the model used for the calculations.
Chapter 6 finally presents, compare and discuss the results of experiments and Monte Carlo simulations.

The thesis work is realized in collaboration with the Nuclear Measurements group of the Energy department of Politecnico di Milano and with the BNCT group of Pavia (INFN and University of Pavia).

Chapter 2

Introduction to BNCT and to neutron spectrometry

2.1 Boron Neutron Capture Therapy, BNCT

Cancer has always existed but in the twentieth century the increasing longevity of the population causes a huge increase of tumors occurrences. The cancer healing is a very complicated issue and nowadays three main types of therapy are clinically used: surgery, chemotherapy and therapies using radiations to kill neoplastic cells. As an enormous variety of different tumor cases exists, the majority of patients with invasive cancers receive multi-modality therapy combining the three in such a way to receive the most effective therapy for their specific case.
The most widely used radiations therapy is the conventional *radiotherapy* which uses $Xray$ or γray radiations to kill tumor cells. However, *Hadrontherapy* importance and clinical use are very fast growing in the last decades as it brings several advantages with respect to the classical radiotherapy. Hadrontherapy uses hadron particles such as protons and carbon ions ^{12}C to kill cancer cells. Hadrontherapy results to be more accurate than radiotherapy in depositing dose to tumor cells and in sparing healthy tissues because of the in-depth dose distribution of particles. Moreover, heavy ions have higher biological effectiveness in killing cells if compared to photons. Anyway, selectivity for both radiotherapy and hadrontherapy depends on the irradiation beam and on the capacity to set a treatment plan to conform the dose distribution as better as possible in the tumour volume. In this respect, *boron neutron capture therapy* ($BNCT$) brings a huge advantage as its selectivity in appropriate conditions is unique, because it does not depend on the neutron beam [41].

Figure 2.1. BNCT facilities in the world for both research and clinical aims. Courtesy of prof. Silva Bortolussi.

2.1.1 Principles

BNCT is an experimental radiation therapy in which boron-10 ^{10}B is attached to a suitable tumor-seeking drug and is administered to the tumor which is subsequently irradiated with a low energy neutron beam [41, 40]. Absorbing neutrons, ^{10}B produces α particles (^{4}He) and ^{7}Li nuclei through the reactions:

$$^{10}\mathrm{B} + n \Rightarrow \begin{cases} ^7\mathrm{Li} + \alpha \quad E_{Li} = 1.01\,\mathrm{MeV}; E_\alpha = 1.78\,\mathrm{MeV} & 6\% \\ ^7\mathrm{Li} + \alpha + \gamma \quad E_{Li} = 0.84\,\mathrm{MeV}; E_\alpha = 1.47\,\mathrm{MeV}; E_\gamma = 0.48\,\mathrm{MeV} & 94\% \end{cases}$$

α and ^{7}Li nuclei have very high Linear Energy Transfer (LET), $150\,\mathrm{keV\mu m^{-1}}$ and $175\,\mathrm{keV\mu m^{-1}}$ respectively. Such high LET leads to very short ranges, about 10 µm for α and about 4.5 µm for ^{7}Li ion. These ranges are similar to the diameter of a mammalian cell enabling the dose to be delivered within or in the immediate neighborhood of the cell in which ^{10}B is located, thereby minimizing the dose to healthy tissues. The fact that only cells containing ^{10}B, most likely tumors cells, will be destroyed results in the therapy selectivity. Boron has a very high cross-section for thermal neutron, about 4000 barns. The ideal neutron beam for BNCT is therefore in the thermal energy range, ≈ 0.025 eV. At thermal energies neutrons are essentially non-ionizing as they are in thermal equilibrium with the surrounding environment. The problem of using thermal neutrons is their low penetration in tissue. Their half-path value is about 1.5 cm so in order to treat also deeper

seated tumor, an epithermal neutron beam (0.1 eV-10 keV) are used instead. As they have higher energy, epithermal neutrons penetrate deeper. They are thermalized passing through tissue and eventually captured by ^{10}B. The optimal neutron energy spectrum is therefore chosen according to the tumor depth: thermal energies are appropriate for shallow tumors while epithermal energies are suitable for deep seated cancers. Anyway, to keep the background as low as possible, the clinical beam should have low contamination of fast neutrons and γ rays, which are a source of non-selective dose deposition. Another beam characteristic required for a safe and effective therapy is a sufficient neutron fluence rate to deliver the therapeutic dose in reasonable time. In order to keep irradiation time below 1 h a fluence rate of about $1 \times 10^9\,\mathrm{cm^{-2}s^{-1}}$ must be achieved [5].
Thus, to increase the therapeutic effectiveness, research is focused on two main fields: the technological development to obtain intense neutron beams and the quest of the boron compound able to increase the intra-cellular boron concentration in tumor cells while minimizing its level in healthy tissue, i.e. to obtain the highest tumor to normal tissue (T/N) ratio. The clinically used boron carriers are sodium borocaptate (BSH), that needs to be administered about 12/18 h prior to the irradiation, and the boronophenylalanine (BPA), administered only 1/2 h before the irradiation. However, recent developments are focused on the formulation of new boron delivery compounds [11]. The ideal boronated drug for BNCT has:

- Low toxicity
- High selectivity for tumor cells
- Capacity to cross the cells membrane and penetrate inside them
- Rapid clearance from blood and normal tissues while persisting in tumors
- Capacity of accumulate in tumor a sufficient boron concentration

Even keeping the boron concentration in healthy tissues as low as possible, there is always an unavoidable background dose that is due to neutron interaction with hydrogen and nitrogen in tissues. Indeed, at thermal energies hydrogen and nitrogen present in tissues undergo the reactions ^{1}H(n,γ)^{2}H and ^{14}N(n,p)^{14}C respectively. Nevertheless, this dose can be kept below the tolerance limit and the T/N boron concentration ratio allows the deposition of therapeutic dose to tumour.

2.1.2 History and clinical use

Boron neutron capture therapy concept was first suggested in 1936 by Locher [24]. Its first clinical use was done in 1950s at the Brookhaven National Laboratory, in the USA [40]. From the late 1960s up to 1992, 120 patients with brain tumors had

been treated using BSH compound and epithermal beam at Hatanaka, in Japan. Resutls were very encouraging in patients with gliomas of grade III and IV. They report a 5 year survival rate of 19% compared to a 5% for conventional radiotherapy. According to [9], between October 2003 and September 2007, several BNCT clinical trials were performed for squamous cell carcinoma (SCC) and locally advanced non-squamous cell carcinoma without malignant melanoma (non-SCC) of the head and neck. An example in Japan is a trial where three patients with newly diagnosed non-SCC, seven patients with recurrent non-SCC and ten patients with recurrent SCC were treated with BNCT. Eleven patients showed complete remission and seven patients showed partial remission of irradiated site. No severe acute or chronic normal-tissue reactions were observed in any patients. The results of these clinical trials show that BNCT is effective and safe in the patients with recurrent SCC and locally advanced non-SCC. Brain tumors were also being treated with BNCT at the JRR-4 reactor, before the reactor closed after the earthquake and tsunami of 2011 in Japan. Studying clinical trials performed at the JRR-4 reactor, Nakai et al. in [29] observed that for newly diagnosed glioblastoma (GBM), median overall survival (OS) reached 25.7 months, and the one and two year OS rates were 85.7% and 45.5%, respectively. BNCT could prolong OS in selected cases. The Japanese tumour registry indicates that the 1-year survival rate for GBM is 55.1%, and the 5-year survival rate is 6.9%. Table 2.1 lists the BNCT clinical treatments for brain tumors until 2014 [29].

Two examples of recent clinical reactor BNCT facilities are the *VTT-BNCT center* in Finland that have treated 249 patients between years 1999 and 2012, and the *Kyoto-KURRI* in Japan that have treated more than 500 patients so far, for tumors like:

- head and neck;
- brain;
- lung and pleura;
- liver;
- skin;
- pelvis;
- bone.

Miyatake et al. in [28] describe the clinical BNCT trials for newly diagnosed Glioblastoma Multiforme: the mean survival time of patients receiving BNCT was significantly longer than the mean survival time of patients who have undergone surgical resection followed by X-radiotherapy and chemotherapy. Indeed, the mean survival time for the latter was 10.3 months (from the historical controls at Osaka

Medical College) while it was 15.6 months for patients who have undergone surgery followed by BNCT alone and 23.5 months for patients treated with BNCT with X-ray boost.

Accelerator-based BNCT

The neutron beam needed for BNCT can be obtained from either a nuclear reactor or from a particle accelerator through charged particles induced nuclear reactions. Different studies have been carried out about the feasibility of BNCT with beams from accelerator, for example, Herrera et al. in [20] show the potential applicability of accelerator based BNCT in the treatment if both superficial and deep-seated tumors. Clinical treatments were performed using a reactor nuclear beam so far, since there did not exist any accelerator-based facility with the required features to carry out optimized BNCT [23]. Research in the last decades focused on accelerator-based BNCT because, differently than reactors, it is possible to install them in health care environments. Furthermore, accelerators are preferred to reactors because their cost is significantly lower, they have higher social acceptability and their licensing, installation and maintenance are much easier [34].
In order to achieve a neutron fluence rate, thermal or epithermal, higher than $1 \times 10^9\,\mathrm{cm^{-2}s^{-1}}$, currents over the mA range of proton or deuteron of few MeV has to be delivered from the accelerator to a proper target which generate the neutron fluence rate through induced nuclear reactions. ^{7}Li(p,n)^{7}Be is the most popular reaction for accelerator based BNCT. It is an endothermic reaction with a Q-value of $-1.644\,\mathrm{MeV}$ and a threshold energy of $1.880\,\mathrm{MeV}$ for the proton to induce the reaction. If the proton energy is around the threshold the neutron has a kinetic energy of about $30\,\mathrm{keV}$, very close to the epithermal regime. For this reason, ^{7}Li target provides one of the best solutions to produce epithermal neutron beams. However, it has some problems related to its thermo-mechanical properties: lithium has low melting point and thermal conductivity ($180.5\,\mathrm{K}$ and $85\,\frac{\mathrm{W}}{\mathrm{mK}}$ respectively). The necessary cooling to dissipate the high power density deposited ($\sim 1\,\mathrm{kWcm^{-2}}$) is technically challenging. Another important issue is that the reaction product ^{7}Be is radioactive, implying risks associated to target activation and environmental contamination. Finally, lithium must be kept under vacuum. An alternative to ^{7}Li is using a target made of ^{9}Be, producing neutrons through the reactions ^{9}Be(p,n)^{9}B or ^{9}Be(d,n)^{10}B. The first is endothermic too and the proton threshold energy is $2.06\,\mathrm{MeV}$; the reaction yield at $2.5\,\mathrm{MeV}$ is much lower than the one of ^{7}Li. In order to achieve a similar production the proton energy must be higher, around $4\,\mathrm{MeV}$. At these proton energies the neutron energy is in the fast range as it get up to $2.1\,\mathrm{MeV}$. The reaction using deuteron as bombarding particles is instead exothermic with a Q-value of $4.36\,\mathrm{MeV}$; its advantages are the absence of an energy threshold for deuteron and a significant neutron production cross section at relatively low energies while its drawback is the significant production of fast

neutrons due to the high value of Q. Eventually, the two main advantages of using ^{9}Be target over ^{7}Li are its stable products (so no residual radioactivity) and its much better thermo-mechanical properties, since beryllium melting point is 1287 K and its thermal conductivity is $190\,\frac{\mathrm{W}}{\mathrm{mK}}$. The use of an appropriate *beam shaping assembly* (*BSA*) to shape and moderate the neutron fluence rate is always needed as the energy of neutrons emerging from the target is too high.
The accelerator device being proposed for BNCT are either electrostatic or radio-frequency (RF) electrodynamics accelerators. Table 2.2 lists the status of accelerators intended for BNCT applications worldwide.

The Italian National institute of Nuclear Physics (INFN) has designed and constructed a RFQ delivering a 5 MeV, 30 mA proton beam [19]. A beryllium target is used to generate neutrons.

2.1.3 Beam Shaping Assembly

In the framework of the INFN project to build a BNCT facility using the RFQ, Ian Postuma in [30] studied the most advantageous BSA configuration in terms of dose distribution in the patient through treatment planning calculations. The goal of the BSA design is the achievement of an epithermal neutron beam to treat deep seated tumors.
The candidate materials composing the BSA must have a high scattering cross-section for neutrons with energy greater than 10 keV while having a low cross-section for neutrons with energy between 0.5 eV and 10 keV in order to obtain the desired neutron peak at epithermal energy range. Furthermore, thermal neutrons must be absorbed and material producing γ rays through the interaction with neutrons should be avoided. The most common materials used are ^{19}F, ^{24}Mg, ^{27}Al and ^{28}Si. Indeed they are able to reduce the fast neutron component without removing neutrons in the epithermal range. Lithium instead, has a high cross-section for thermal neutrons and it does not produce any γ. Among other materials tested, AlF3 has proven the best performance in moderating neutrons to the desired energy range, allowing low fast contamination but still providing an epithermal neutron fluence rate well above $1 \times 10^{9}\,\mathrm{cm^{-2}s^{-1}}$. The final BSA configuration is therefore made of AlF_3 as bulk moderating material and other elements will be used to reduce the photon contamination and to shape finer the neutron energy distribution.
The optimal neutron beam has been designed selecting the 90° direction with respect to the proton beam. The 90° configuration reduces by a factor of 0.2 the fast neutron component compared to the 0° configuration. The final BSA configuration is shown in figure 2.2.

According to the simulations, the optimal BSA has a lead shield and it is covered with a layer of lithium loaded polyethylene. The reflector material is AlF_3 while the effective BSA cone is made as indicated in table 2.3. The parameters of interest achieved with this final configuration are listed in table 2.4.

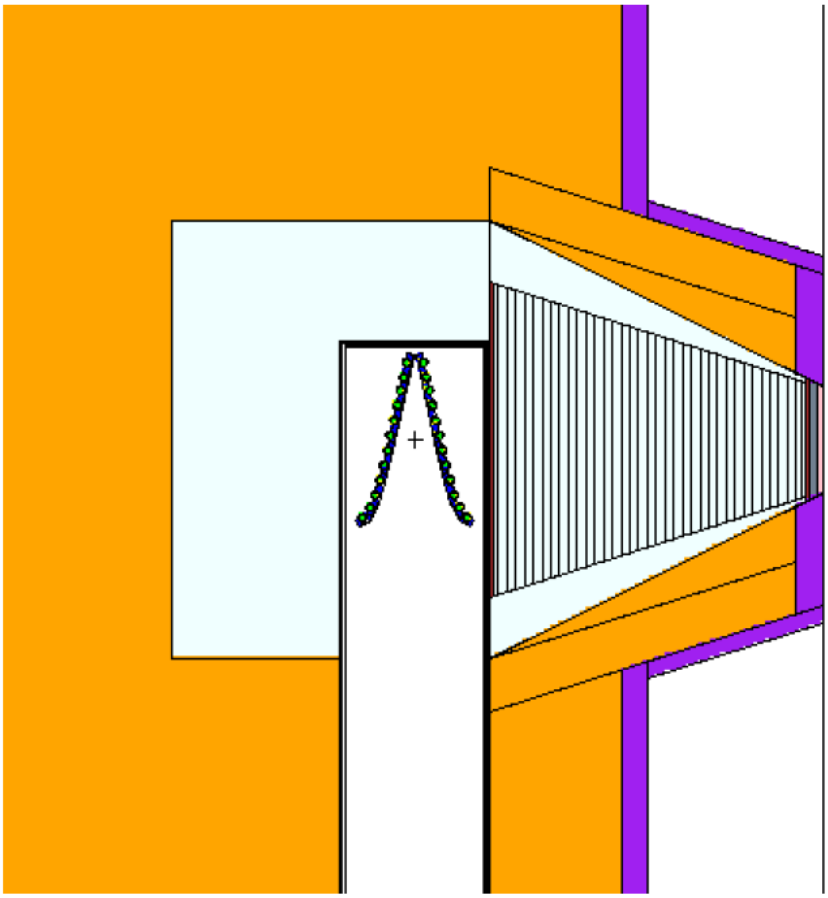

Figure 2.2. Schematic representation of the BSA final configuration, **??**.

2.1.4 Aluminum trifluoride (AlF_3)

Aluminum fluoride exists in powder, that would be very difficult to be used to build the BSA. These powders have a density three times lower than the nominal one, even if pressed inside a proper holder. This would require larger moderation volumes and the uniformity of the moderating material would not be ensured. It is possible, however, to obtain a solid material through sintering. An INFN experiment, in collaboration with University of Pavia, for the first time produced densified elements of AlF_3 mixed with LiF. Lithium removes the thermal part of the spectrum, allowing lower contamination in this part of the spectrum. This new material is being studied to characterize the impurities present in the powder, that

may constitute a source of induced radioactivity and to test its mechanical resistance. The most important characterization, however, is related to the moderation property of the densified material. In fact, simulations have been carried out to design the beam, but no measurements have ever been conducted.
This thesis aims at giving the first experimental neutron spectra obtained by solid AlF_3. By comparing them with simulations, experimental spectra constitute the first validation of Monte Carlo calculations involving AlF_3.

Beam	**Periods**	**Boron agents**	**Pathology**	**#**	**Median survival [months]**
Brookhaven Graphite Research Reactor					
Thermal	1951-1959	Borax	HMBT	10	3.2
		Sodium pentaborate iv	HMBT	9	4.9
		Sodium pentaborate ia	HMBT	9	3.2
Massachusetts Institute of Technology (MIT) Reactor					
Thermal	1959-1961	Carboxylphenylboronic acid	GBM	16	5.7
		Sodium decahydrocarborane	MB	1	
Brookhaven Medical Research Reactor					
Thermal	1959-1961	Sodium pentaborate	BT	18	2.9
Epithermal	1994-1999	Boronophenylalanine (BPA)	GBM	53	12.8
5 Japanese reactors: Hitachi Training Reactor, Japan Research Reactor No. 2, Japan Research Reactor No. 4, Musashi Institute of Technology Reactor, and Kyoto University Reactor					
Thermal	1968-1996	Sodium borocaptate (BSH)	GBM	NA	21.3
			AA	NA	60.4
MIT research reactor					
Epithermal	1996-1999	BPA	GBM	20	11.1
Finnish research reactor 1					
Epithermal	1999-2001	BPA (250 mg)	GBM	30	13.4
		BPA (450 mg)	GBM		21.9
	2001-2008	BPA	rGBM	20	7
Kyoto University Reactor(KUR)/JRR-4 (Osaka Medical School)					
Mixed & Epithermal	1997-2014	BPA+BSH	GBM	21	15.6
		BPA	rGBM	22	10.8
KUR/JRR-4 (Tokushima University)					
Mixed & Epithermal	1998-2002	BSH, BSH+BPA	GBM	23	19.5
JRR-4 (University of Tsukuba)					
Mixed & Epithermal	1998-2011	BSH, BSH+BPA	GBM	15	25.7
Studsvik Research Reactor					
Epithermal	2001-2003	BPA (900 mg)	GBM	29	14.2

Table 2.1. Clinical BNCT trials for patients with malignant brain tumors. GBM: Glioblastoma; rGBM: recurrent glioblastoma; MB: Medulloblastoma; BT: Brain tumor; MBT: HMBT: Highly malignant brain tumor; AA: Anaplastic astrocytoma.[29]

Location	Machine	Facility status	Target & reaction
Japan, University of Tsukuba	RFQ-DTL	Under development	Be(p,n)
Japan, KURRI, Osaka Med College, Tohoku Hospital	Cyclotron	Clinical trials on-going	Be(p,n)
Japan, NCCenter - CICS Tokyo	RFQ	Under development	Solid ^{7}Li(p,n)
Japan, Nagoya University	IBA Dynamitron	Purchased	Liquid (static) ^{7}Li(p,n)
Israel, Soreq	RFQ-DTL	Under development	Liquid (jet) ^{7}Li(p,n)
Russia, Budker Institute	Vacuum insulated Tandem	Under development	Solid ^{7}Li(p,n)
Argentina, CNEA	Single-ended ESQ	Under development	Be(d,n) thin & ^{13}C(d,n) thick
Finland+USA, HUCH-NT	Single-ended DC	Under commissioning	Solid ^{7}Li(p,n)
UK, Birmingham University	Dynamitron	Upgrade delayed	Solid ^{7}Li(p,n)
China, IHEP	RFQ	Under development	Be(p,n)
China+USA, NEUBORON+TAE	Tandem electrostatic		Solid ^{7}Li(p,n)

Table 2.2. Status of the accelerators intended for accelerator-based BNCT facilities worldwide. Courtesy of prof.ssa Silva Bortolussi.

	^{9}Be target
BSA material	0.5 cm LiF 36.5 cm AlF_3 0.5 cm LiF 1 cm Ti 0.5 cm Bi

Table 2.3. BSA materials configuration, from the beryllium target outward. Refer to figure 2.2.

ϕ_e	$\frac{\dot{D}_f}{\phi_e}$	$\frac{\dot{D}_\gamma}{\phi_e}$
10^{9} cm^{-2}s^{-1}	10^{-13} cm^{-2}s^{-1}	10^{-13} cm^{-2}s^{-1}
2.7	6.8	6.2

Table 2.4. BSA performances. $\dot{D}_f$ is the fast neutrons dose rate; $\dot{D}_\gamma$ is the γ dose rate; ϕ_e is the epithermal neutron fluence rate.

2.2 Neutron spectrometry: state of the art

Neutron spectrometry is a wide field to which a brief general introduction is given mainly focusing on those methods somehow related to this thesis work.
One of the main difficulties in the detection of neutrons is the fact that they do not ionize directly matter. Neutrons interact mainly with atomic nuclei leading to nuclear reactions. As their energy is transferred and shared among the reactions products, by measuring their energy deposition we can derive the neutrons spectrum. Another issue is that usually most of neutron spectra consist of broad energy distributions and mono-energetic lines are quite the exception [36]. This behavior brings the need of paying more attention to the background radiation than for γ spectrometry where γ-ray tend to exhibit one or more mono-energetic lines highly standing over the background continuum. Moreover, neutron spectra are likely to extend over a very wide energy range. They usually have, indeed, a thermal component in the region of eV as well as a fast component with energies up to MeV or GeV in the case of cosmic-ray neutron spectra. A high energy resolution is very difficult to be obtained over the whole spectrum and at present status does not exist any methods to do it. There exist methods to measure the whole spectra with low resolution in energy (for example the Bonner sphere spectrometer) or to measure with higher resolution narrower energy ranges, from 50/100 keV to about 10 MeV. Neutron spectrometers can be classified into seven groups based on the principle used to measure neutron energy [18]:

1. methods in which neutrons are scattered and the recoil nuclei energy is measured;

2. methods in which the energies of charged particles released in neutron-induced nuclear reactions are measured;

3. methods in which the neutron velocity is measured;

4. methods in which a minimum neutron energy is indicated by the appearance of a neutron-induced effect, threshold methods;

5. methods in which the energy spectrum is calculated by unfolding a set of readings of detectors which differ in the energy-dependence of their response to neutrons;

6. methods based on neutron diffraction;

7. methods in which the time-distribution slowing down of a short burst of high energy neutrons is measured.

Each of these methods has its own specific field of application. However, the techniques listed in items 1, 3 and 5 are used mostly. Table 2.5 gives an overlook on the

Group	Spectrometer	Energy range [MeV]			Resolution
1	Recoil proportional counter	0.05	to	5	high
1	Organic scintillator	2	to	150	high
1	Recoil proton telescope	1	to	250	high
2	^{3}He gridded ionization chamber	0.05	to	10	high
2	^{3}He-semiconductor sandwich	0.1	to	20	high
2	Diamond semiconductor	8	to	20	high
3	Time of flight	0.2	to	15	high
4	Super-heated drop (bubble)	0.1	to	20	low
5	Multi-sphere	1×10^{-8}	to	200	low

Table 2.5. Operative energy range of some neutron spectrometer [18].

operative energy range of some spectrometers. As it can be read, spectrometers of group 2 operate with high resolution in an interesting range of energies. The main nuclear reactions used in the neutron spectrometer of this group are ^{3}He(n,p)^{3}H, ^{6}Li(n,α)^{3}H, ^{10}B(n,α)^{7}Li, ^{12}C(n,α)^{9}Be and ^{28}Si(n,α)^{25}Mg [18]. In particular, the ^{3}He(n,p)^{3}H reaction is the leading method for neutron spectrometry in the energy range 50 keV to about 5 MeV. ^{3}He is used with different technologies such as proportional counters, gridded ionization chambers and sandwich spectrometers and their response function can be simulated accurately. Diamond and Silicon semiconductor crystals are particularly used for plasma diagnostics applications.

2.2.1 Neutron spectrometry by means of recoil nuclei

Two types of "recoil spectrometers" can be classified in this group:

- recoils at all angles contribute to the spectrum of energy deposition;
- only recoils at a given angle (preferably 0°) are accepted (*recoil telecope*).

Their response function consists of the recoil energy spectrum resulting from bombardment with monoenergetic neutrons, at different neutron energy, and it is usually a broad continuum for the first category while it is much narrower in the case of telescopes [18]. Recoil telescope spectrometers have therefore a simple response function which ideally approaches a single sharp peak at a pulse height uniquely related to the neutron energy. For general recoil spectrometers instead, since the recoil energy distribution will not resemble the neutron spectrum because of the broad continuum response function, experimental data unfolding is required. Unfolding techniques are usually complex and need accurate response functions. The most commonly used recoil-reaction is the (n,p) scattering where neutrons transfer

their energy to recoil protons by scattering with a Hydrogen nuclei [36]. Scattering occurs at different angles so the portion of energy transferred is variable, as described by the following equation:

$$E_p = E_n \cos^2 \theta \tag{2.1}$$

where θ is the angle between the proton emission direction and the neutron direction before the collision, E_p is the energy of the recoil proton and E_n is the energy of the neutron. Since the (n,p) cross section is well known, response matrices and detection efficiencies can be made accurately and neutron spectra can be reliably unfolded.
One of the most commonly used recoil spectrometers is the Hydrogen-filled proportional counter. It can operate with high resolution in energy in a range from $\sim 50\,\text{keV}$ up to $1.5\,\text{MeV}$ but it requires counters with three or more different gas pressures. Proton escape phenomena limit proportional counters for higher energies where organic scintillators are preferred instead. Stilbene crystals and liquid scintillators allow γ-neutron discrimination through pulse-shape analysis. γ discrimination contributes to limit the minimum detectable enrgy. Looking to the upper limit, ions produced by neutron interactions with carbon nuclei of the organic scintillator has to be accounted for above about $8\,\text{MeV}$, when their contributions to the response function become relevant. Above $15/20\,\text{MeV}$ response functions are increasingly difficult to simulate because of lack of accurate cross-section data. Moreover, the spectrometer calibration becomes an issue because of the lack of accurate calibration fields. A method was studied to build response matrices for the unfolding, being reliable up to about $70\,\text{MeV}$. The rapid increase of proton range with energy puts a serious upper energy limit.
An interesting spectrometer was first developed by Armishaw [10], the *Transportable Neutron Spectrometer*. It includes a scintillator and several Hydrogen recoil counters. Several attempts are being made to improve the TNS. Digital signal processing for $n - \gamma$ discrimination and miniaturized electronics will be included to reduce the TNS size and weight.

2.2.2 Time of flight

Time of Flight (ToF) technique works with a simple, but complex to set up, principle. The time taken by the neutron to fly a known distance is measured and its velocity is calculated. The neutron energy is then easily derived from its velocity. To carry out the measurement, two timing signals are needed, when the neutron is generated or leaves a particular point and when it arrives at a neutron detector some known distance away [36]. The start signal can be determined by:

- a pulsed source (for example an accelerator with beam pulsing capabilities);
- detecting the radiation generated together with the formation of the neutron (for example a γ associated with the neutron production);

- detecting the scattering of the neutron in a detector.

Neutrons can be detected with any suitable fast neutron detector, such as organic scintillators or Lithium glass detectors. It should be pointed out that the response function of the detector needs to be known and the timing electronics is obviously more complex than for simple counting experiments. Further ToF systems are very sophisticated and have very big dimensions. Sometimes the instrument is itself the experimental facility. Indeed, the quality of the spectrum depends mainly on the length of the flight path, the longer the better. Typical dimensions of flight path are from 4 to about 10/15 m. For short flight paths, the detector thickness becomes relevant too. Also the pulse width contributes to the spectrum quality, the sharper the better. ToF can measure high resolution neutron spectra in the fast neutrons range, from 0.2 keV to 15 MeV. Thanks to its reliability it is used at metrology laboratories to characterize the fields in which calibrations are performed. ^{252}Cf spectrum, which is one of the sources recommended by the International Organization for Standardization (ISO) for neutron calibration, has been determined using ToF. The measurement was performed incorporating the ^{252}Cf in a pulse fission chamber that provides the start pulse while the end pulse is obtained using a liquid scintillator.

2.2.3 Multi-sphere systems

The first multi-sphere system was proposed by Bramblett, Ewing and Bonner [17] in the sixties. The original *Bonner Sphere Spectrometer* (BSS) was made up of five spheres of different diameters having different response functions. Each sphere comprises a small thermal neutron detector (^{6}LiI(Eu) cylindrical crystal, 4 mm in diameter and 4 mm in length) at the center of a polyethylene sphere [18]. The most modern versions of BSS are typically constituted by 10-12 spheres [36]. Despite the bigger number of different spheres leads to the bigger amount of data available for the measurements, the amount of extra info provided decreases from a certain number of spheres on because of the similarity of the response functions. The neutron spectrum is determined by measuring the count rate for each detectors and unfolding them using the proper response matrix. BSS operate on very wide energy range, from thermal to fast neutrons regions, providing low resolution spectra and reliable integral information. BSS are therefore often used in radiation protection applications. Another advantage of Bonner Spheres is that they allow a good discrimination between neutrons and γ. Whereas, other than their time-consuming measurements and their bulky equipment, the main BSS drawback is the uncertainty in spectrum unfolding. Generating the neutron spectrum from the recorded count data is a indeed an underdetermined process because the number of spheres used is much lower than the number of energy bins of the final spectrum [22]. Most codes carry out a least squares iterative search, attempting to find the spectrum that best matches the observed counting rate for all spheres. Additional external

information are used for the unfolding. A useful additional item is a "guess spectrum" based on some a-priori information usually from Monte Carlo simulations. New designs are being studied for the BSS evolution. One of the most interesting uses a single block of moderator containing either several position-sensitive thermal neutron detectors or a number of small thermal neutron detectors set at different positions. The different positions of neutron detectors becomes the variable in the response matrix instead of the sphere diameters. In this way all measurements can be made simultaneously [12].

2.2.4 DIAMON, Direction-aware Isotropic and Active MONitor with spectrometric capabilities

DIAMON is a smart and innovative low resolution neutron spectrometer implemented by the nuclear measurements group of Politecnico di Milano in collaboration with Raylab [1], an Italian start-up spin off of Politecnico di Milano. It is the first all-in-one portable detection system capable of performing neutron spectrometry, to reconstruct neutron direction distributions and to properly derive field, integral and operational quantities in real-time. It is made up of multiples neutron detectors placed in different positions inside the moderator and its innovative design leads to an isotropic response and to an optimized energy dependence. The embedded proprietary unfolding code *UNCLE* allows a real-time assessment of the neutron spectrum and a subsequent derivation of the spectrum from thermal neutron energies to 20 MeV the low energy version, and to 5 GeV the high energy version. Dosimetric, radiation protection and field quantities (such as fluence, H*(10), field fraction, ...) are directly calculated from the spectrum and a proprietary method and algorithm give real-time information about the 3D direction distribution of neutrons.

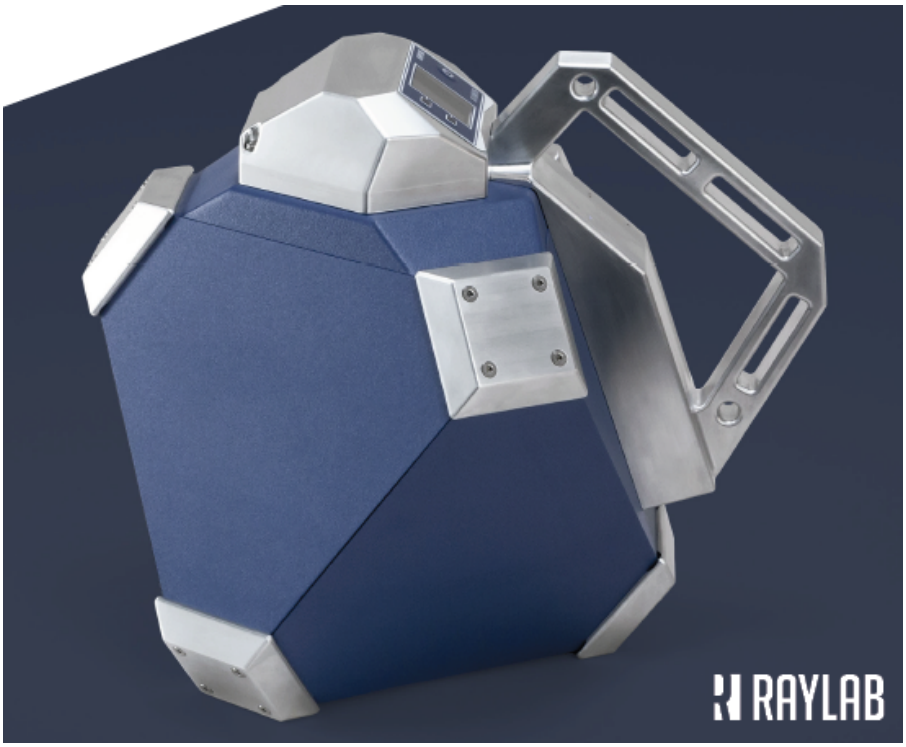

Figure 2.3. DIAMON

Chapter 3

ACSpect neutron spectrometer

In this section, the ACSpect neutron spectrometer is described in details.
The ACSpect is a high energy resolution neutron spectrometer based on a two-stages Monolithic Silicon Telescope (MST) coupled through a collimator to an organic scintillator, made of polyvinyl-toluene, that works as active converter too. It is an *active* converter because it converts neutrons into recoil protons meanwhile measuring the energy they deposit inside it. This innovative feature gives the spectrometer its name: *Active Converter Spectrometer*. The ACSpect can therefore be considered a *recoil proton telescope* spectrometer. It was first designed and developed by the Nuclear Measurements group of the Energy department of Politecnico di Milano [8] and later improved by them [6, 25]. In the framework of this thesis, a further improvement is implemented by changing its technological configuration and the whole elaboration process. The result is a much more compact instrument set-up, with better transportability and higher adaptability to different experimental environments being much less sensitive to external disturbances. It should be stressed that the energy resolution of this spectrometer at 200 keV has been achieved otherwise with time of flight systems that, other to be very complex, are so bulky to be impossible to transport.
Figure 3.1 shows the *ACSpect* system with all its components, whereas figure 3.2 is the *ACSpect* scheme.

3.1 Spectrometer design

In this section, the design of the ACSpect is presented. Focusing on its two main components: the active converter and the Monolithic Silicon Telescope (MST).

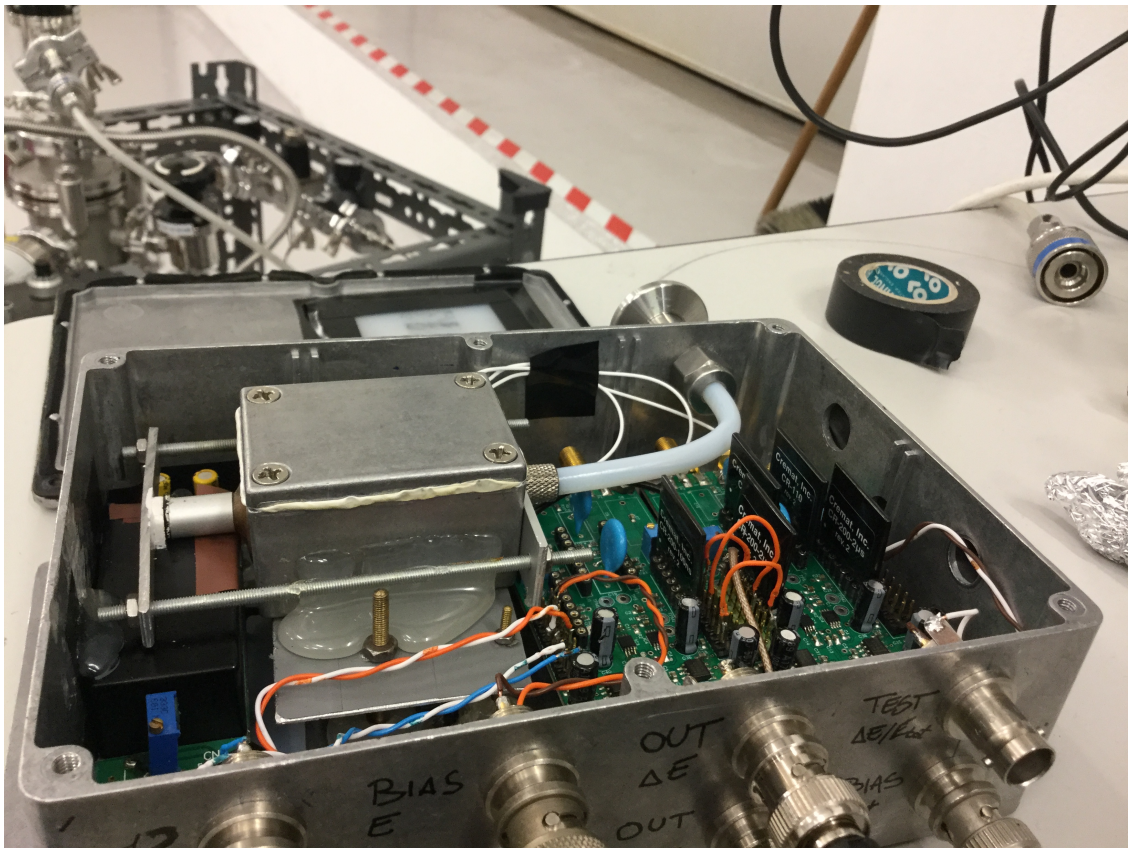

Figure 3.1. ACSpect. The external box is opened to show all its components.

3.1.1 Active converter

Placed at 1.476 cm from the ACSpect main box front, the active converter has the double function of converting impinging neutrons to recoil-protons and of measuring the energy deposited by the generated recoil-protons. Therefore it has to be a scintillator with hydrogen atoms abundance in order to promote (n,p) scattering reactions, between neutron and converter H atoms, producing recoil-protons. The active converter is indeed a 2 mm thick BC-404 scintillator fabricated by Saint-Gobain Crystals [33, 32], with an overall area of 7.3 mm x 9.5 mm. It is a polyvinyl-toluene based scintillator emitting blue light with a high light output and a very fast response. Table 3.1 shows the main BC-404 scintillator data. The radiation passing through the scintillator deposits energy exciting the scintillator atoms and molecules that relax emitting light. The light intensity depends on the energy released in the material. Since at energies lower than 1 MeV the quantity of optical photons generated per event is quite lower than for higher energies [33], the uncertainty of the scintillator information is negatively affected for proton energies below 1 MeV.

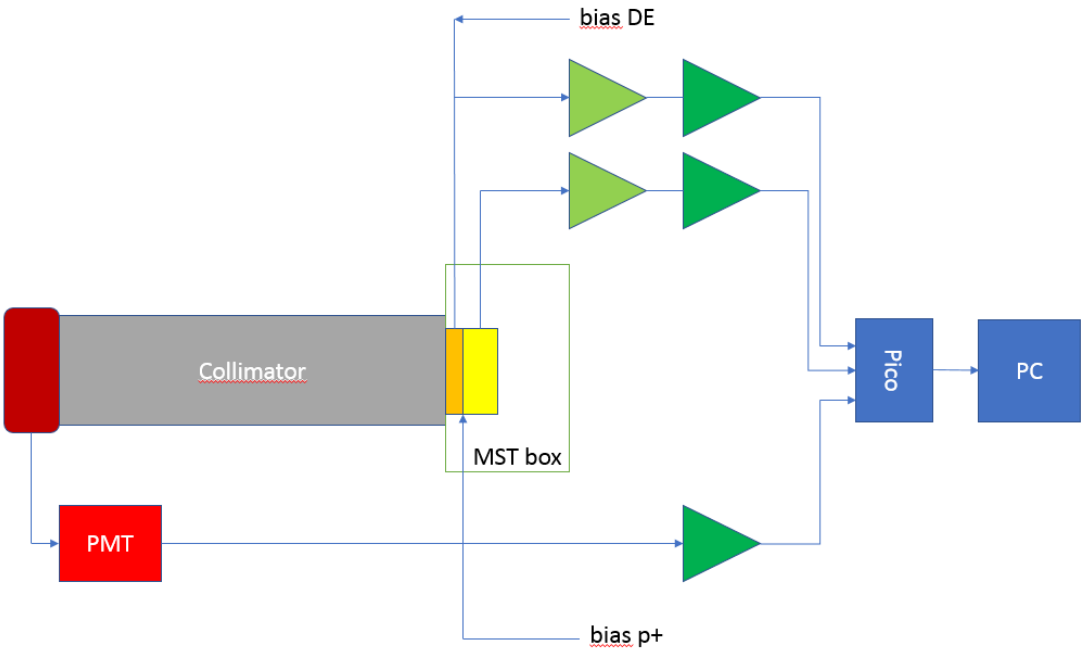

Figure 3.2. Scheme of the *ACSpect* spectrometer configuration with electronics and acquisition chains. The scheme is not in scale. The dark-red box represents the scintillator/converter, the red box labeled "PMT" represents the photo-multiplier tube, the orange and the yellow boxes represent respectively the DE and E stage of the MST, the light and dark green triangles represent pre-amplifier and amplifier respectively and the blue box labeled "Pico" represent the acquisition device.

Moreover, the scintillator energy-response is non-linear because the effect of high ionization lowers the light conversion yield. It alters, indeed, the behavior of the plastic scintillator molecules, that are responsible of the light generation. The non-linear dependence of the light emitted per unit length dL/dx on the energy released per unit path dE/dx by the interacting particle is well described by the Birks' law [13, 14]:

$$\frac{dL}{dx} \propto \frac{\frac{dE}{dx}}{1 + k_B \frac{dE}{dx}} \tag{3.1}$$

where k_B is the Birks' constant. It express the non-linearity as the equation is linear for $k_B = 0$ and it depends, indeed, on the material. For polyvinyl-toluene based scintillators, k_B is estimated to be 0.088 mm/keV [37]. Integrating equation (3.1) we have an equation for the light generated by a proton L . Considering E_{prel} to be the energy released by the proton in the scintillator and $\left(\frac{dE}{dx}(E_p)\right)^{poly}$ to be the proton stopping power in polyvinyl-toluene as a function of the proton energy,

Property	Value
Light output [% Anthracene]	68
Rise time [ns]	0.7
Decay time [ns]	1.8
Pulse width in FWHM [ns]	2.2
Wavelength of maximum emission [nm]	408
Light attenuation length [cm]	140
Bulk light attenuation length [cm]	160
Number of H atoms [cm^{-3}]	5.21×10^{22}
Number of C atoms [cm^{-3}]	4.47×10^{22}
Ratio H : C atoms	1.1
Density [$g\,cm^{-3}$]	1.032
Refractive index	1.58
Expansion coefficient [$°C^{-1}$] (for $T < 67\,°C$)	7.8×10^{-5}
Softening point [°C]	70
Vapor pressure	may be used in vacuum
Light output	$-60\,°C$ to $20\,°C$ independent from temperature; at $60\,°C$ it is 95 % of that at $20\,°C$

Table 3.1. BC-404 scintillator main data, [32].

the generated light is given by

$$L = \int_0^{E_{prel}} \frac{1}{1 + k_B \left(\frac{dE}{dx}(E_p)\right)^{poly}} \, dE_p \tag{3.2}$$

The procedure to correct the non-linearity of the scintillator is explained in section 3.3.
The scintillator is finally coupled with the H10720-110 photo-multiplier tube fabricated by Hamamatsu [2]. The device, shown in figure 3.3, is made up of the photo-multiplier tube R9880U [3] and its high voltage power supply circuit. The Photo-Multiplier (PM) is responsible of the conversion of scintillator light pulses into electronic signals. It is eventually coupled with the electronics to which it sends the signals of detected radiation and from which it is supplied. As it can be shown in table 3.2, the photo-multiplier has fast response to handle high count rates and high sensitivity in the visible range to make up for the low scintillator response.

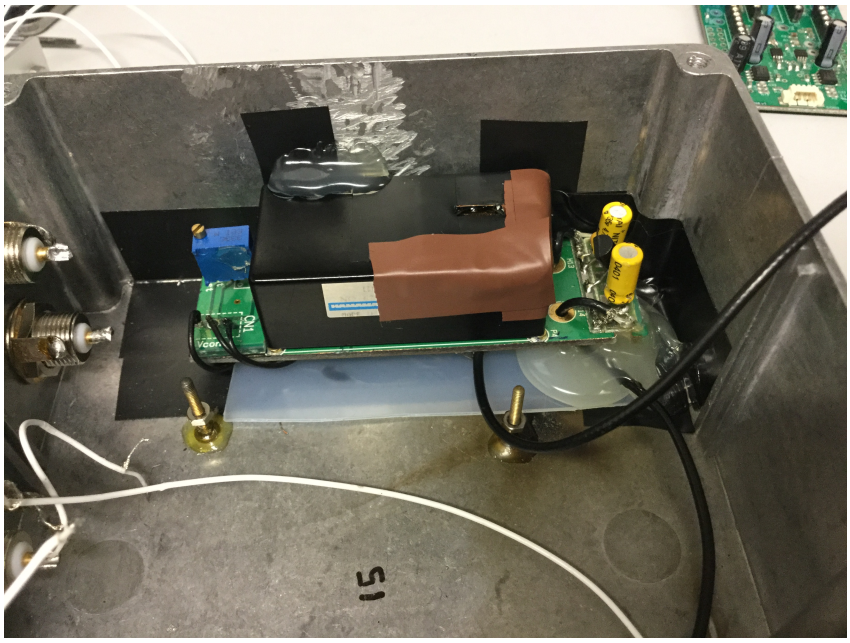

Figure 3.3. Photo-multiplier device, already glued to the ACSpect box bottom.

Collimator

The active converter is connected to the telescope through a geometric collimator (see figures 3.1 and 3.2). The collimator is an aluminum cylinder 21 mm long and 4 mm in diameter facing the scintillator back-surface through an o-ring and put under vacuum in order to avoid proton energy loss in air. The aim is to reduce the emission angle range of recoil-protons reaching the MST. Using this collimator, of the whole scintillator area, only the part facing the collimator tube is actually sensitive. Considering the tube dimensions, the scintillator sensitive area is 12.5664 mm^2 leading to a recoil-proton maximum detectable emission angle of $\theta = 7.35°$ [25].

3.1.2 Monolithic silicon telescope, MST

The MST is a semiconductor silicon wafer which is used to detect those recoil-protons selected by the collimator and to measure their remaining energy (since part of the energy with which they are emitted was deposited in the scintillator). It is placed right to the collimator face, so that the alignment between the scintillator and the MST is granted, and into an aluminum box which dimensions are 52 mm x 38 mm x 21 mm. The box was sealed because it has to be under vacuum as the collimator with which it is glued. In order to provide vacuum it is equipped with a vacuum connector. Figure 3.4 is a picture showing the active converter, the

Property	Value
Spectral response [nm]	230 -700
Input voltage [V]	4.5-+5.5
Max input current [mA]	2.7
Max output current [µA]	100
Control voltage [V]	0.5to+1.1
Effective area ϕ [mm]	8
Peak sensitivity wavelength [nm]	400
Rise time [ns]	0.57
Operating temperature [°C	5 to+50
Weight [g]	45
Width x Height x Depth [mm]	25 x18x50
Cathode	
Luminous sensitivity [µA/lm]	105
Blue sensitivity index	13.5
Radiant sensitivity [mA/W]	110
Anode	
Luminous sensitivity [A/lm]	210
Radiant sensitivity [A/W]	2.2×10^5
Dark current [nA]	1

Table 3.2. H10720-110 photo-multiplier tube main data, [2].

collimator and the MST box. The Monolithic Silicon Telescope is the prototype R327-12 # 5 M1. After a very thin dead layer of Titanium, about 0.24 µm thick, the device is characterized by two stages, called *DE* and a *E* stages, which thicknesses are respectively 1.9 µm and 500 µm and it has a square area of 1 mm^2. Figure 3.5 shows a scheme of how the MST is made up. The use of a semiconductor for radiation measurements is made effective by the properties created at a junction where *n-type* and *p-type* semiconductors are brought into good thermodynamic contact [22]. Biasing the *n-p* junction, the high electric field arisen in the region between the electrodes, called the *depletion region*, separates via drift the electron-hole pairs generated by ionizing radiation and their rapid movement produces a current pulse at the electrodes [16]. It is made up of two stages, commonly referred as *DE* and *E*, that are fabricated on a single Silicon substrate [4]. They share a *p+* electrode which separates them and it is realized through deep ion implantation. The whole Silicone substrate is in contact with two further electrode acting as non-injecting ohmic contacts [38]. These are the *n+n* junctions and they are placed one on the backside and the other on the front becoming therefore the entrance

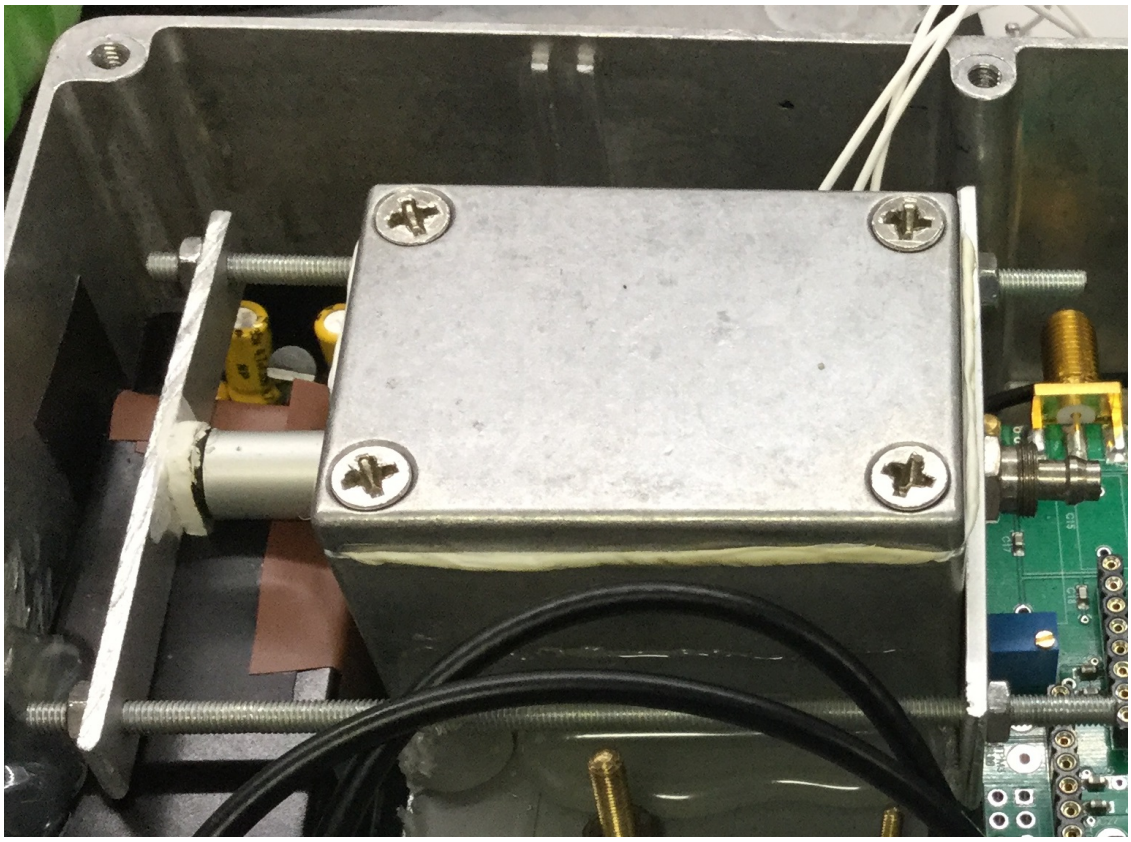

Figure 3.4. Scintillator-collimator-MST set up. From the left to the right, the white body is the scintillator, coupled at its bottom with the photo-multiplier, facing through an o-ring the collimator; at the other side of the collimator there is the MST box with the vacuum connector on its back.

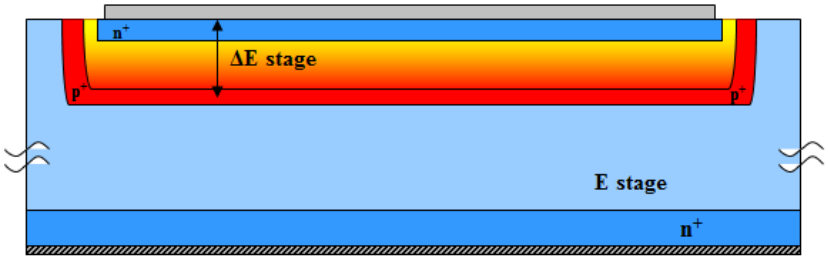

Figure 3.5. Scheme of the Monolithic Silicon Telescope, courtesy of prof. Andrea Pola. The *DE* and the *E* stages are clearly represented as well as the *p+* and the *n+* electrodes.

window of the MST (so it must be very thin). The two stages behave in this way like two biased *p-n* junction diodes collecting charges via drift driven separation of

electron-hole pairs in the polarized depletion region [31]. The three electrodes are connected with the electronics from which they are biased and to which they send the pulses generated by radiation. The *DE* stage is connected to the ground whilst the *common* $p+$ and the E_{tot} stage are biased with $-6\,\mathrm{V}$ and $150\,\mathrm{V}$, respectively. The *DE* stage is polarized with a much lower potential difference because it is much thinner. With this configuration, the $p+$ electrode collects the holes produced by radiation in the telescope whereas the $n+$ electrodes collect the electrons produced in the *DE* and the electrons produced in the *E*, respectively. As the $p+$ collects holes, the signals produced has negative amplitude and therefore they have to be inverted when acquired. As far as the *ACSpect* is concerned, it has been chosen to use the so called *DE*-E_{tot} MST configuration, collecting data from the *DE* and the *common* electrodes. The pulses are indeed representative of the energy deposited by the ionizing particles in the first stage alone, E_{DE} (pulses from the *DE*), and of the energy deposited in the whole telescope, E_{tot} (pulses from the *common*).

Scatter plot

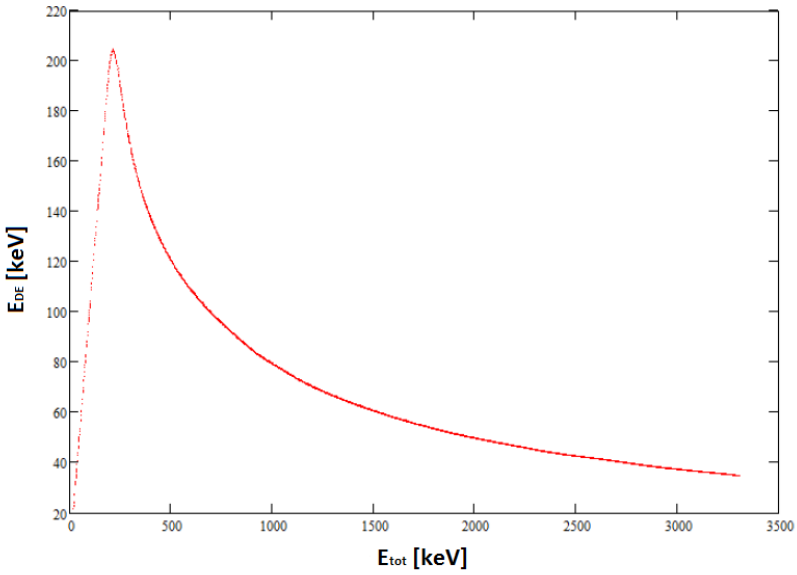

Figure 3.6. *DE*-E_{tot} scatter plot curve calculated with the numerical model developed in [25] for 3.31 MeV protons.

Since the *DE* stage is the first if the MST's with respect to the incoming particle direction, as shown is figure 3.2, a charged particle getting to the telescope has three possibilities:

- to release energy in the *DE* and stop within that stage;

- to release energy in the *DE* and get to the *E* stage where it stops releasing its remaining energy;

- to get to the *E* without any energy release in the *DE*.

Since the last case is very hardly happening however small is the *DE* thickness, we will not consider it. The occurrence of one of the other two cases instead of the other strongly depends on the energy the particle has when it comes to the MST. If its energy is high enough it succeeds in getting to the *E* stage, if it has not it stops within the *DE*. In both these situations signals are produced in both *DE* and E_{tot}; when the particle stops within the first stage, as the E_{tot} account for the energy released in both stages, the signals have the same amplitude (as far as the amplification chain is the same) whilst in the other case, the higher particle energy, the bigger is the E_{tot} signal with respect to the *DE* one. The curve describing the energy release distribution between the two stages is characteristic of the type of particle and of the telescope. It takes the name of *scatter plot* and it is represented in a $Energy_{DE}$ vs $Energy_{E_{tot}}$ graph. Lorenzoli in [25] implemented the physical model to calculate the characteristic curves for protons and alpha particles. A picture of the protons theoretical scatter plot is shown in figure 3.6. Figure 3.7 shows instead two examples of measured scatter plots: 3.7(a) is a $^{241}_{95}$Am 's α scatter plot from one of the measurements carried out for the instrument calibration at Polimi's *Nuclear Measurements Laboratories*; 3.7(b) is, instead, a recoil proton scatter plot from one of the measurements carried out at the INFN's LNL. The two possibilities the protons have getting to the telescope are well distinguished in the scatter plot. As one can see from figures 3.6 and 3.7, there is a proportional region related to all those particles stopping within the *DE*, that takes the name of *stopper* region, and there is the hyperbolic region related to all those particles getting to the *E* stage. The trend of this latter region is due to the way ions release energy in solid matter. Their stopping power curve is indeed the Bragg peak curve. Such a trend for the scatter plot is expected since protons release more energy nearby the point they stop so the more energy they have, the farther they stop from the *DE*, the less energy they release in the *DE*. As far as the stopper region is concerned, recoil protons are effectively discriminated from secondary electrons generated in the Silicon telescope by background photons [7]. However, when we are dealing with low energy of the order of 30/40 keV, attention must be paid anyway. These electrons have energies that could get up to several dozen keV and they produce the same signals produced by a proton with that energy.

3.2 Electronic chain and data acquisition

The major spectrometer improvement is made on its electronic chain that is completely changed with respect to the previous *ACSpect* version. Figure 3.8 shows

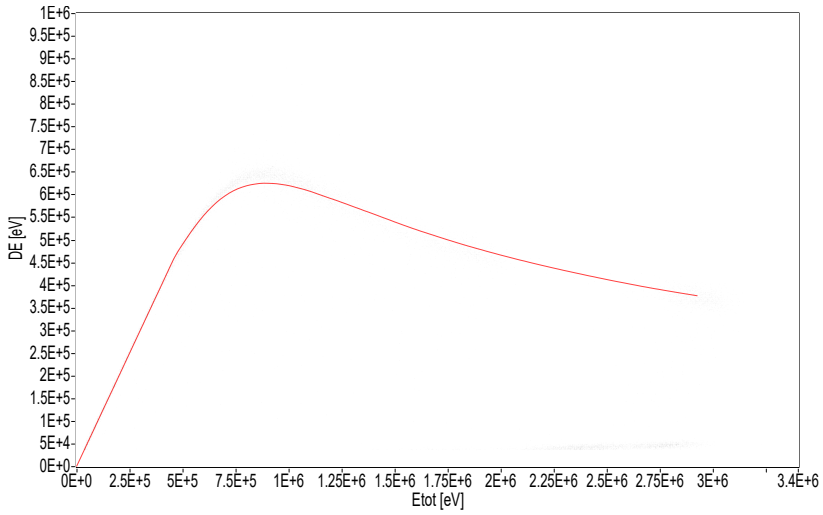

(a) α scatter plot by $^{241}_{95}$Am

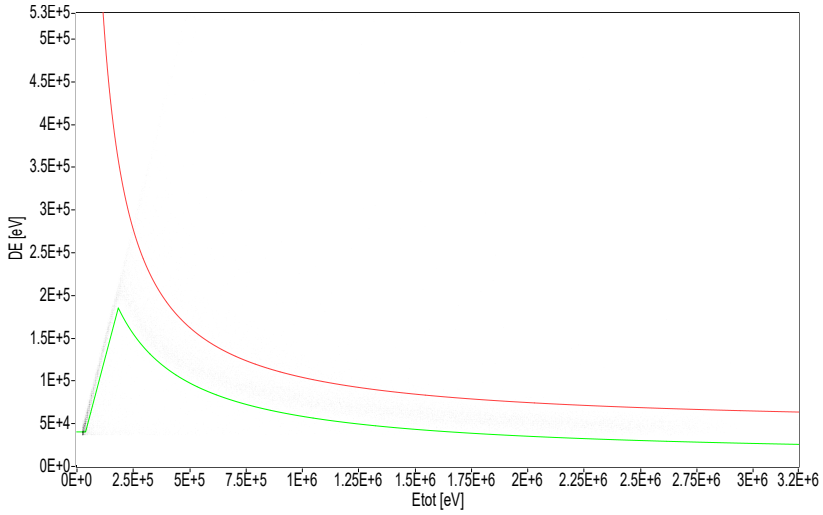

(b) recoil proton scatter plot

Figure 3.7. Scatter plots from two different measurements: (a) scatter plot of the events measured from an $^{241}_{95}$Am source at the Polimi's *Nuclear Measurements Laboratories*, the red line is the physical model curve. (b) scatter plot of the events measured from an accelerator based neutron beam at INFN's LNL, the red and the green curves are the scatter plot selection curves.

the ACSpect components before the improvement. Figure 3.9 shows instead the improved ACSpect.

All the electronic connections of the MST and of the PMT are coupled with the front-end electronics (still inside the instrument box). The new front-end electronics is made up of two equal electronic boards, shown in figure 3.10. They were

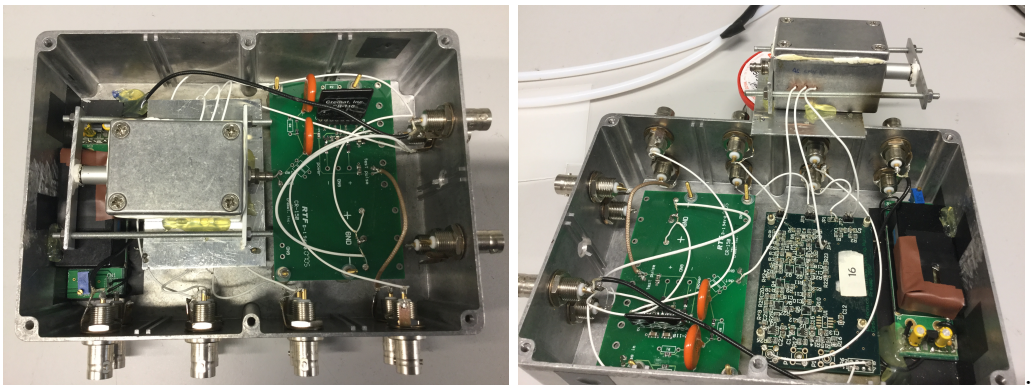

(a) Old ACSpect device, main box opened

(b) Old ACSpect device, main box opened with disassembled MST box

Figure 3.8. Old ACSpect configuration, before the improvement

designed by Nuclear Measurements group of the Energy Department of Politecnico di Milano. Each of them can handle two channels which test line and bias are coupled. They are used for managing all needed inputs and outputs and, in order to have the most compact configuration they are provided with all the amplifiers and pre-amplifiers needed. Furthermore, they both are placed in a separate region from the detectors. This new feature, since in the old configuration one of the two electronic board was placed right under the MST box, avoid any undesired electronic contact and induction between electronics and detectors because they are set apart.
Four channels (since each of the two boards has two channels) are available to handle three outputs and two bias input (table 3.3). It has been chosen to assign each

Outputs	Bias input
DE	*E*
common	*common*
PM	

Table 3.3. Electronic connections needed by MST and PM.

output to a different electronic channel. The three channels are therefore connected to the *DE*, to the *common* (E_{tot} channel) and to the *PM*. Then, since one of the two bias polarizing the MST has to be sent to the *common* that is already coupled to an electronic channel, the bias is given to that channel. As far as the other bias is concerned, it is assigned to the remaining fourth electronic channel and the channel connected to the *E* stage. One electronic board is used for the *DE* and for the *common* while the other for the *PM* and for the *E*. Table 3.4 schematizes

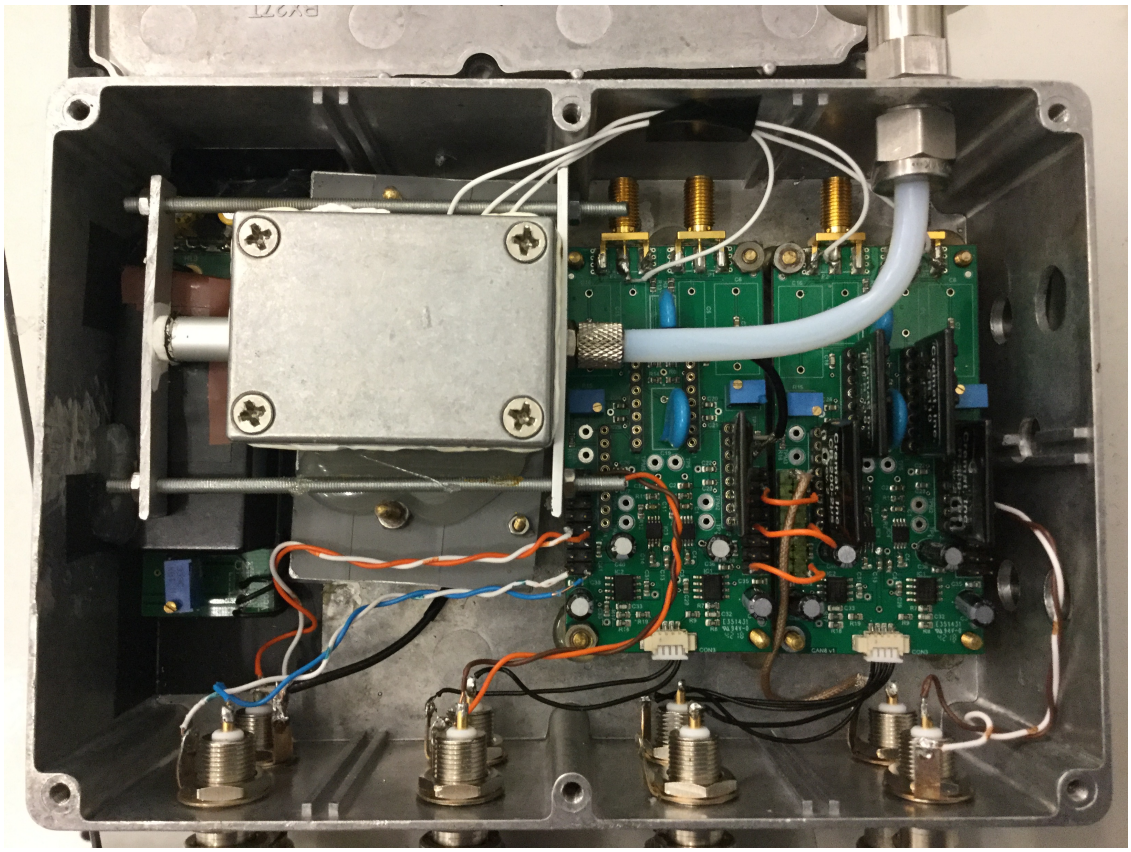

Figure 3.9. Upper-view of the final ACSpect set up. The separation between the detectors region and the electronics region is clearly visible as well as the three amplification chains and the connections between detectors, electronic boards and I/O connectors.

this configuration outlining the role of each electronic channel. In order to manage

Electronic board A		Electronic board B	
channel 1	channel 2	channel 1	channel 2
E bias		*common* bias	mass
	PM output chain	E_{tot} output chain	DE output chain

Table 3.4. Electronic channels configuration.

this configuration, since the bias is common for the two channels of each electronic board, the capacitance coupling the two channels is removed. By doing so, the bias is provided to one channel only while the other remain un-biased. In particular, the biased channels are the E and the *common*. The un-biased channels are connected

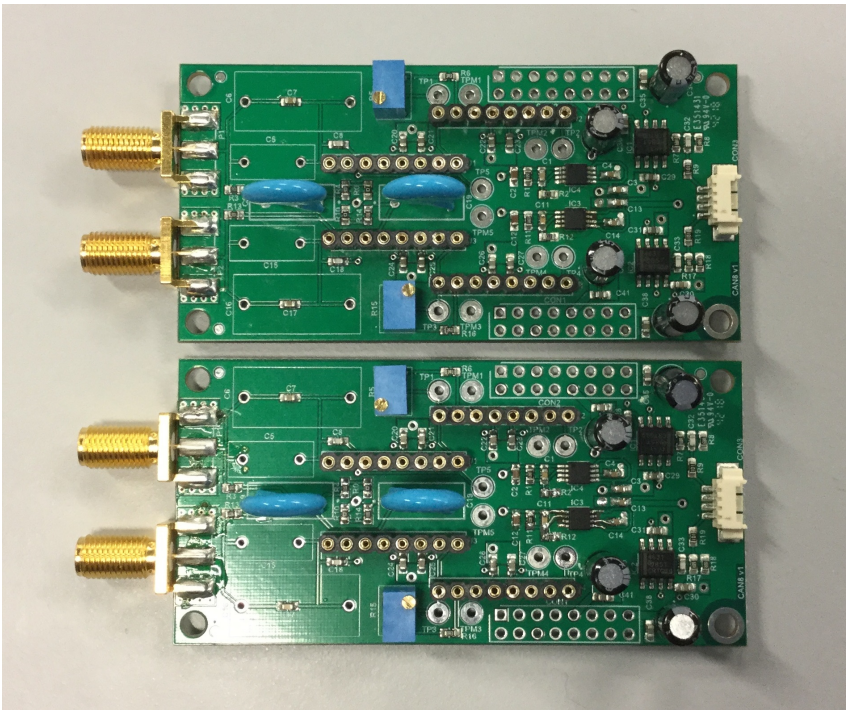

Figure 3.10. Electronic boards used to build the ACSpect.

to the mass-potential by means of a high resistance, to avoid electronic signal losses. The electronic boards used were designed to be equipped with Cremats amplifiers and pre-amplifiers. This feature is strongly improving the spectrometer because otherwise signals would be amplified by means of external amplification systems, as the old version was. Having the amplification within the front-end electronics inside the ACSpect reduces noise at minimum, eliminating all those external disturbances due to the external long-cabled amplification chain that behaves like an antenna. The DE and E_{tot} output chains are equal and are equipped with a Cremat "CR-110-R2" pre-amplifier and a Cremat "CR-200-2μs Gaussian shaping" amplifier each. They technical data are found in table 3.5. The electronic chain of the PM output is different instead, as it does not need pre-amplification. Therefore, to shorten the chain as much as possible, the PM output is directly welded to the amplification input. The amplifier used is a Cremat "CR-200-250ns Gaussian shaping", chosen for its short shaping time needed to accommodate the fast response and high count rate of the PM. Some of its specifications are found in table 3.5. Finally, from the amplifiers-exit to the board-output, each channel has later electronics providing a further gain of a factor 2 through a buffer. This further gain brings the PM signals to saturate also for low energies. The PM amplifier's output is therefore connected directly to its related spectrometer's output connector, by-passing the later electronics. Finally a $\pm 12\,\mathrm{V}$ power supply is provided to the

Property	Value
Cremat CR-110-R2 pre-amplifier	
Gain [V/pC]	1.4
Rise time * [ns]	7
Decay time constant [µs]	140
Maximum charge detectable per event [pC]	2.1
Power supply voltage [V]	
maximum	± 13
minimum	± 6
Output offset [V]	+0.2 to -0.2
Output impedance [Ω]	50
Cremat CR-200 Gaussian shaping amplifier	
Polarity	non-inverting
Output impedance [Ω]	< 5
Output offset [mV]	-40 to +40
Power supply voltage [V]	
maximum	± 13
minimum	± 5
CR-200-250ns	
Shaping time [ns]	250
Gain	10
Output pulse width (FWHM) [ns]	590
Input resistance [Ω]	240
Input capacitance [pF]	1000
Input noise voltage [µVRMS]	60
CR-200-2μs	
Shaping time [µs]	2
Gain	10
Output pulse width (FWHM) [µs]	4.7
Input resistance [kΩ]	2
Input capacitance [pF]	1000
Input noise voltage [µVRMS]	30

Table 3.5. Cremats CR-110-R2 and CR-200 specifications.
* Pulse rise time (defined as the time to attain 90% of the maximum value) has a linear relationship with input capacitance: $t_r = 0.4C_d + 7$, where t_r is the pulse rise time in ns, C_d is the added capacitance in pF.

two boards and to the photo-multiplier. Figure 3.9 shows the ACSpect components with all connections welded.

The whole assembly is placed inside a 122 mm x 172 mm x 54 mm aluminum box. All the electronic connections with the external are made using BNC connectors:

- the 12 V and the −12 V supplies;
- the E and the *common* bias;
- the DE, E_{tot} and PM channels output;
- the signal test input for the MST channels (one for both);

for a total of 8 connectors. The cables used for almost all the connections between the spectrometer components are coaxial cable.
The three output channels are sent from the spectrometer to the acquisition device and this latter is connected to a PC. The acquisition device used so far is the PicoScope-4424, for which it is implemented an ad-hoc acquisition program with Labview.

Data acquisition program

The data acquisition program, which main interface is shown in figure 3.11, is the means of communication between the PC and the acquisition device. It runs with all PicoScope-4000 series devices. The acquisition device needs to be set for

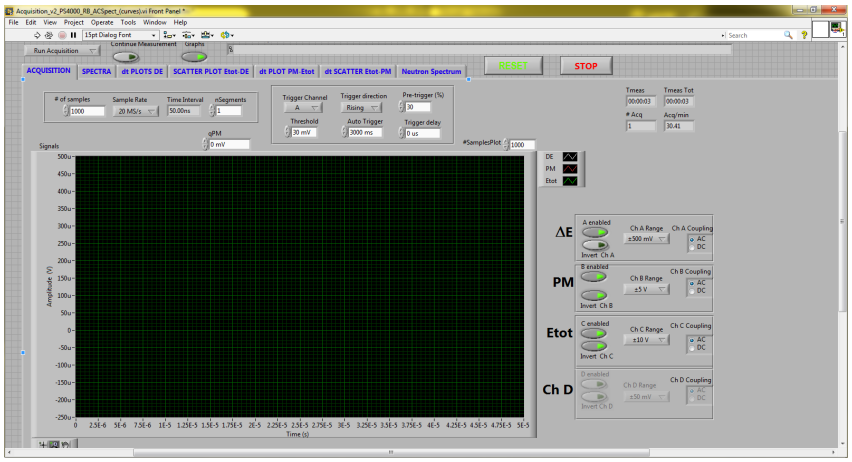

Figure 3.11. Screenshot of the "Acquisition" page of the acquisition program interface. When the program is working, the graph shows the signal acquired in a *pulse amplitude* [V] vs *acquisition instant* [s] plot. All buttons, drop down menu and blank windows are input parameters while the grey ones are indicators.

the acquisition. PicoScope provides some ad-hoc library function for Labview to communicate with the device. Each library function has a particular task. After

open the communication with the acquisition device, the acquisition settings are set up, imposing, between others, the acquisition *sample rate*, the channels to activate and their *range* (that is the voltage range on which the device samples the signal acquired), the channel on which setting the trigger and the trigger threshold. When the trigger is used, the device acquires and sends signals only when the amplitude of a signal of the selected channel overcome the trigger threshold. The signals acquired are within a certain time interval around the triggered instant. In the meanwhile the code creates the *.bin* files where it will write acquired signals. After the settings-section, it starts the actual acquisition cycle code. Each time the PicoScope triggers and acquires a signals train, it fills a memory segment with it. When the number of memory segment filled is equal to the number set, a cycle starts. Signals data are written in the *signals.bin* files; they are converted from "sampling-channels" to V and they are plotted. They are then processed by the Labview sub-function "peak" which once it gets the signals data, the sample rate, the channel range and the amplification shaping time, it seeks and finds all peaks and their location. Peaks are calibrated to their corresponding energy values by using the relation

$$E_{peak} = m_{channel} A_{peak} + q_{channel} \tag{3.3}$$

where m and q are the calibration factors, A is the peak amplitude and E is the peak energy. Data are then sent to the elaboration algorithm which is explained in section 3.3. It will not be the final elaboration but it gives a first on-line estimation of the neutron spectrum. The acquisition program prints out several plots useful for the on-line monitoring:

- spectrum of acquired events for each channel
- spectrum of proton events for each channel
- DE vs E_{tot} and PM vs E_{tot} scatter plots
- $t_{DE} - t_{PM}$ and $t_{DE} - t_{E_{tot}}$ plots
- final proton and neutron spectra

The possibility of having an on-line monitoring of the results is extraordinarily useful as the user can get aware of any trouble or wrong-functioning during the measurement so that the experiment can be stopped to try to fix the problem without losing the whole measurement duration time getting aware of the problem only once at home. Moreover, the user can monitor the results statistics and know when you get a suitable one.
The final part of the code has the function of saving data. It saves and closes the *signals.bin* files and also it saves in another proper *.bin* file the details used for the acquisition and the "pre-elaboration".

3.3 Data elaboration

In the framework of this thesis, a new elaboration algorithm, more appropriate for the recoil-protons selection and investigation, is implemented.
The ACSpect can be considered a recoil-proton telescope spectrometer. Indeed the neutron energy spectrum is derived from the recoil-proton spectrum. The relation between the neutron energy and the recoil-proton energy, as discussed in chapter 2.2, is given by the equation:

$$E_p = E_n \cos^2 \theta \tag{3.4}$$

where θ is the angle between the proton emission direction and the neutron direction before the collision, E_p is the energy of the recoil proton and E_n is the energy of the neutron. A recoil-proton must be detected by both the scintillator and the MST in order to be measured effectively by the spectrometer. Considering the ACSpect configuration, figure 3.2, it has to survive the collimator to be measured by both the detectors. Thanks to the collimator, as described in section 3.1, all measured protons have a direction within an angle $\theta = 7.35\,°\mathrm{C}$ with respect to the impinging neutrons. Equation (3.4) allows us to consider $E_n \approx E_p$ with an uncertainty of about 1.63% [25]. We have therefore information on neutrons energy straight forward out of the measured recoil protons energy, without the need on any unfolding technique that is often insidious and complicated. This is another main feature of the *ACSpect*. Since data elaboration is not slowed by the unfolding process, we can have on-line neutron spectrum results while performing measurements by using the elaboration algorithm in the acquisition program.
Following neutrons in their way through the spectrometer, still referring to figure 3.2 for a clearer understanding, the elaboration process is explained. Impinging neutrons n get into the active converter and have a certain probability to collide with its atoms. As it is an organic material, the most likely interaction the neutron can undergo is with Hydrogen atoms. Collisions between neutrons and H atoms can result in (n, p) scattering reactions, leading to the emission of recoil protons. Defining Σ_{np} as the (n, p) reaction cross section in polyvinyl-toluene and assuming the (n, p) scattering is the only interaction, by neglecting the nuclear reactions with ^{12}C nuclei (good approximation for neutron energies below 8 MeV), the physical law governing the neutrons flight across the converter is

$$n(x + dx) = n(x) - n(x)\Sigma_{np}dx$$

The number of neutrons surviving a certain thickness t of the converter is given by the following expression:

$$n_{surv}(t) = n_0 e^{-\Sigma_{np}t} \tag{3.5}$$

where n_0 is the number of neutrons entering the converter. The number of recoil protons p is, instead, the number of neutrons that experienced a (n, p) collision

within the distance flown dx, $|dn| = |n(x + dx) - n(x)|$.

$$p_{gen} = n_0 \Sigma_{np} dx \tag{3.6}$$

To reach the MST, the recoil-proton has, at first, to get out of the scintillator without being auto-absorbed. The recoil proton starts flying within the scintillator where it has been generated, releasing energy through unelastic collision. Protons have a certain *range* (the minimum thickness of material needed to stop them) depending mainly on their energy and on the material. It is clear that a proton, to get out of the scintillator, has to be generated within its range from the scintillator end. Then, the proton has to get to the telescope through the collimator. Its presence brings to the lost of all that protons getting out of the scintillator without a proper direction. To account for that, a detection efficiency $\varepsilon_{scint-MST}$ was calculated using a suitable model considering the (n,p) cross section and the recoil angle probability distribution.
Eventually, defining t_{scint} as the polyvinyl-toluene scintillator thickness, R_{p+} the proton range in polyvinyl-toluene and assuming Σ_{np} depending on neutrons energy but uniform within the scintillator, the impinging neutrons must survive a distance $t_{scint} - R_{p+}$, undergo a (n, p) collision within the remaining converter thickness (R_{p+}) and generate a recoil-proton with a direction that let it get to the telescope overcoming the collimator. With these considerations, using equations (3.5) and (3.6), we can easily come out with the expression that relates the number of detected protons with the number of neutrons got to the converter:

$$p_{detected} = n[e^{-\Sigma_{np}(t_{scint} - R_{p+})} \Sigma_{np} R_{p+} \varepsilon_{scint-MST}] \tag{3.7}$$

Once neutrons are converted and recoil protons detected by both the detectors, the three output signals that are generated must be discriminated against other signals such as electrons or noise in MST and such as γ radiation in the scintillator, and they must be coupled. To handle that, three different selections are done: the *scatter-plot* selection and two *time-coincidence* selections which couple events between channels too.

3.3.1 Scatter plot selection

Starting from the theoretical curve, the scatter plot selection picks out all those events scattered within a proper range around the theoretical curve, as shown in figure 3.12. As explained in section 3.1, distinguishing recoil-protons from secondary electrons generated in the silicon telescope by background photons can give some trouble at low energies. In the ACSpect case, electrons are further discriminated by same-energy protons because electron events have not any corresponding *PM* signal. However, it could happen that some *PM* γ event or disturbance occurs *randomically* with a good time coincidence with the electron. These "fake-proton"

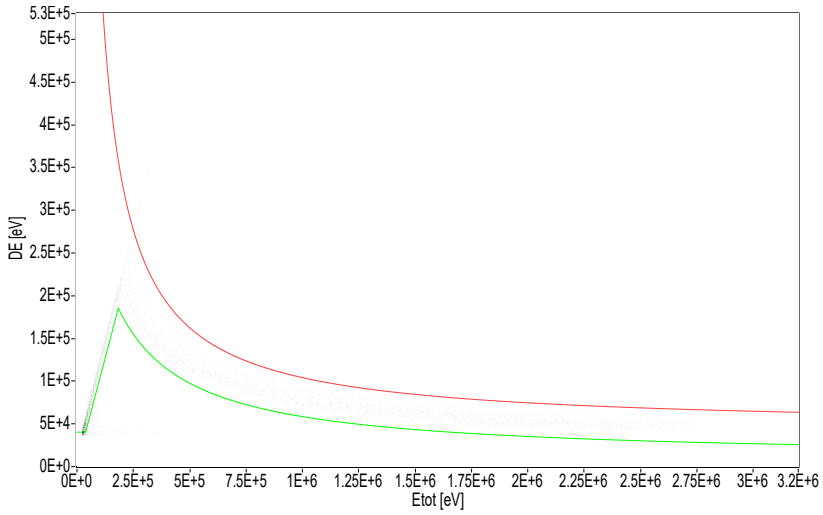

Figure 3.12. Scatter plot of the events measured from an accelerator based neutron fluence rate at INFN's LNL, the red and the green curves are the scatter plot selection curves.

events have obviously low energy. A proper energy "e-threshold" is therefore set to 40 keV on both DE and E_{tot} channels. The e-threshold value has been studied by observing its effect on the neutron spectrum. The critical energy region for the neutron spectrum is below 200/250 keV. The reason is that a $\sim$ 100 keV proton has a very short range in matter so it is very tricky to detect as it should be generated at the scintillator bottom edge and it could anyway be auto-absorbed in the roughness thickness. The little number of these events can therefore easily be overestimated by electrons events. The e-threshold value is chosen by looking for that value that being set would have lowered only the energy bins below 200 keV, without involving also higher energy bins.

3.3.2 Time coincidence between MST signals

To support the scatter plot selection, a time coincidence selection is performed on the two MST's channels. As we can notice from figure 3.13, almost all events selected by the scatter plot fit the time coincidence condition. The aim of this first time coincidence is to further clean from possible randomic disturbances or fake events. As figure 3.13 shows, the events distribution in the time-coincidence plot has a double trend. This is expected since the two trends correspond to the events of particles which have stopped within the DE stage and to the events of particle which got to the E stage. Figure 3.14 represents with different colors the two cases. Indeed, when the acquired signals data are read by the elaboration program, a trigger procedure similar to the acquisition triggering is performed on all the three

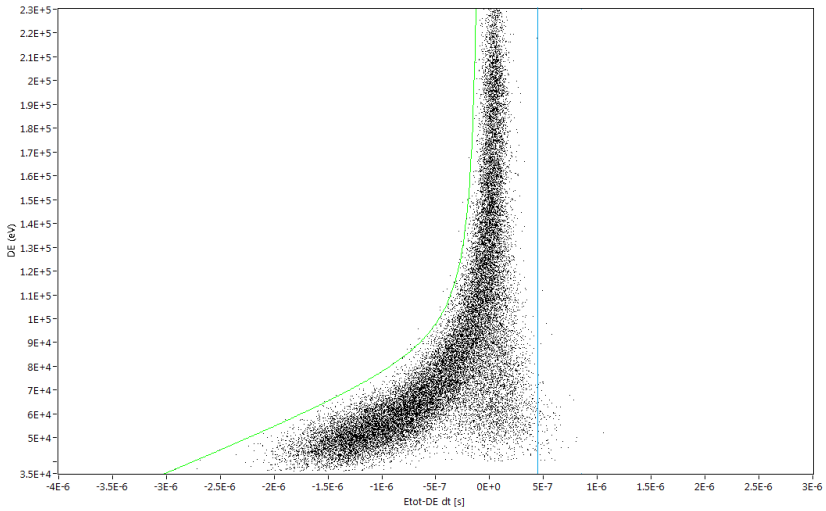

Figure 3.13. Time coincidence plot between the E_{tot} and the DE signals.

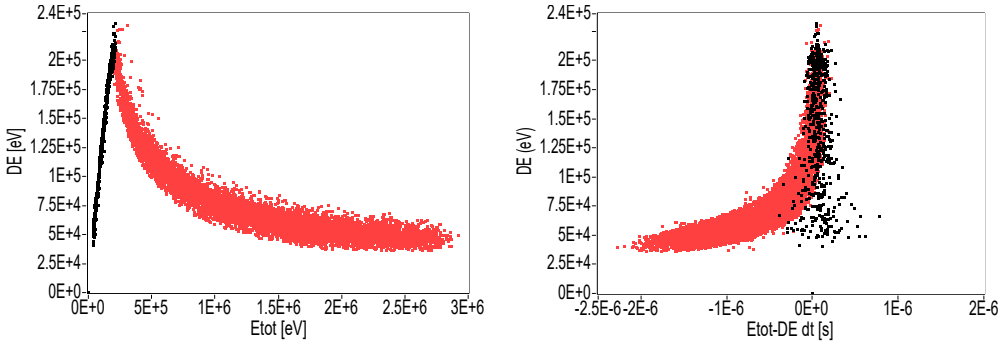

(a) Recoil protons scatter plot

(b) Time coincidence plot

Figure 3.14. Parallelism between the scatter plot and its related $E_{tot} - DE$ time coincidence plot. The relation between the two trends regions of the scatter plot and the two different shapes in the dt plot is highlighted by using two different colors.

channels signals to define the time location of the peaks. As soon as the signal overcome the threshold, the program identifies the pulse in time and looks for its shape. In the case the proton stops within the DE, the DE and the E_{tot} signals have quite the same shape and amplitude because the energy measured by the two channel is the same and their electronic chains are equal. The location of the two signals is therefore the same but for experimental spreading. A time windows of about 0.8 µs is considered for the selection. Signals at low DE are expected to be more spread around because the trigger (identifying the location) precision lowers as the signal slope decreases. Whilst in the case the proton reaches the E stage,

the E_{tot} signal is bigger so its shape is sharper because in almost the same pulse width it has to rise upper. It means that the trigger sees the signal in advance with respect to the DE one. The bigger is the E_{tot} signal, the more in advance is triggered and moreover, as the scatter plot shows, when it gets bigger the DE gets lower so the dt between the two channels grows conferring that particular shape to the time coincidence curve. Figure 3.15 shows the MST signals couple for the two cases.

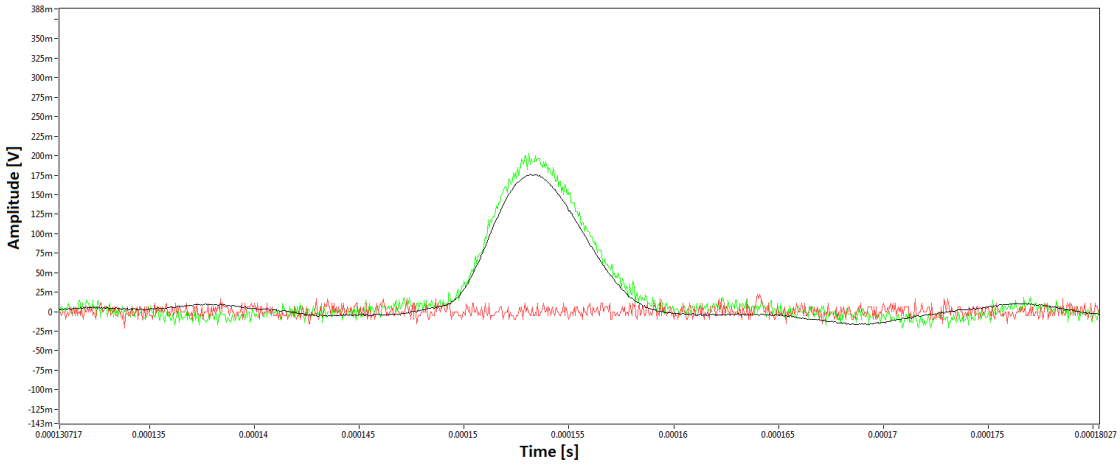

(a) Recoil proton stopped within the DE stage

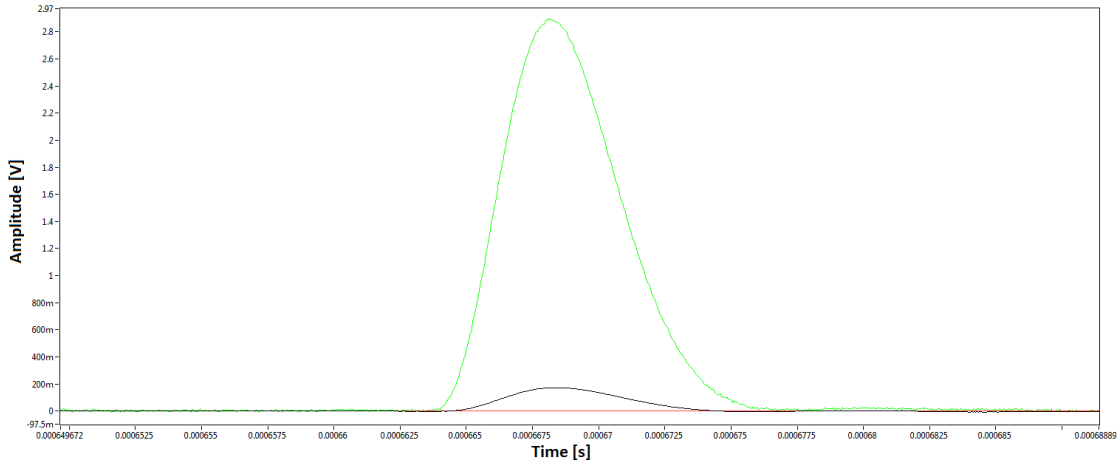

(b) Recoil proton stopped in the E stage

Figure 3.15. DE and E_{tot} signals for those two stopping cases. The black signal is the DE signal while the green one is the E_{tot}.

3.3.3 Time coincidence between *DE* and *PM* signals

The time coincidence between the *DE* and *PM* signals further discriminates real recoil-proton events and it has also the fundamental aim of linking each MST proton event to its corresponding *PM* signal. Figure 3.16 is the *PM-DE* time coincidence plot, from one of the measurements carried out at LNL. Similar reasons to the E_{tot}-

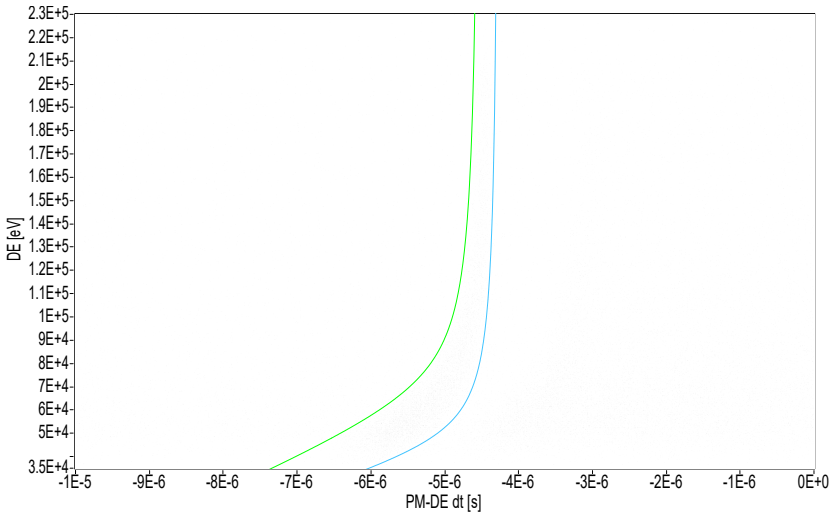

Figure 3.16. Time coincidence plot between the *PM* and the *DE* signals.

DE time coincidence ones, explain also the distribution shape of the *PM-DE* time coincidence. Considering a certain *PM* amplitude, for lower *DE* peaks the signal slope is lower and the trigger threshold is reached farther leading to a bigger delay between the two signals. Since the electronic chains are different, their amplifiers are different and the time-response of the detectors is different, the two signals have a roughly constant electronic delay difference of about 4.3 ns.
The reason why the coincidence is looked for the *DE* channel instead of the E_{tot} is the fact that the acquisition trigger is set on *DE*. For each *DE* signal, one for each acquired window as it is the trigger channel, the elaboration program looks for the *PM* event which matches the time coincidence condition, coupling therefore PM and MST signals.

3.3.4 Time coincidence between E_{tot} and *PM* signals

A third time-coincidence has been studied. The coincidence between a *PM* and a E_{tot} event is expected to be within a straight time interval but for very low energies where the E_{tot} signal heavily smooths its profile increasing the delay between its location and the *PM* one. Figure 3.17(a) shows the *PM*-E_{tot} time coincidence

plot of a measurement. Three different regions are highlighted with different colors. The green points are all those events within the straight time interval, the red points are the low $E_{E_{tot}}$ events while the black points seem to be out of coincidence events. However they do not look like randomically dispersed but their dispersion with respect to the coincidence time interval is more and more pronounced for higher E_{tot} energies. This behavior bring us to reason if putting a further selection but we did not at last. As far as the measurements on which we made this study are concerned, for higher $E_{E_{tot}}$ it becomes increasingly easier having lower E_{PM} since their sum is the total proton energy and for neutrons from 5 MeV protons on beryllium the energy end point is about 3.2 MeV. Figure 3.19 shows clearly what we are just saying, looking at the graph and considering red points indeed, we see that for higher $E_{E_{tot}}$, the maximum E_{PM} occurring is linearly decreasing. Since the photo-multiplier has a very fast response, the signal shaping is very fast and when it gets lower, its location is more difficult to be defined correctly as the pulse is made of few acquisition points. The time location uncertainty of low energy PM events leads to the dispersion with respect to the coincidence interval. The fact that the dispersion is on both sides of the coincidence dt gives credit to our theory. What's more, looking at 3.17 we see that "black events" places randomically in the middle of a good scatter plot region, without placing in isolated or border region, giving further credits to our believing that they are good events. This third time coincidence is therefore not used for any selection but it should be always check that events assume a correct distribution also on it.

Signals triplets corresponding to the recoil protons are identified this way. Figure 3.18 shows a signal triplet generated by a recoil proton.

3.3.5 Linearization of the scintillator energy-response

Once the protons triplets are identified, the recoil-proton energy is derived from a combination of the energy information brought by PM and E_{tot} channels. Indeed, neglecting possible energy losses through the collimator that is under vacuum, the whole proton energy is released within the scintillator and the telescope. The non-linearity in the scintillator energy response has now to be resolved. An analytical linearization procedure was developed by Lorenzoli in [25]. The procedure to correct the non-linearity of the scintillator is well-represented by figure 3.19. As it is shown, from the generated light curve obtained by equation (3.2) with polyvinyl-toluene k_B, a fictitious equivalent light L_{EQ} is calculated, corresponding to the light that would have been generated by the scintillator if the proton energy released in the telescope E_{TEL} would have been released in the scintillator. Summing L_{EQ} to the actual light generated by the scintillator L_{scint}, we have the total light L_p that would have been generated if the proton would have stopped within the scintillator releasing

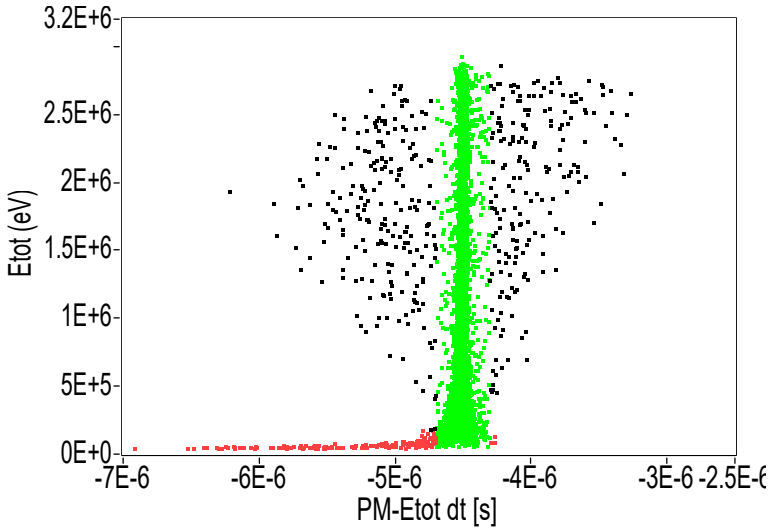

(a) dt between E_{tot} and PM plot

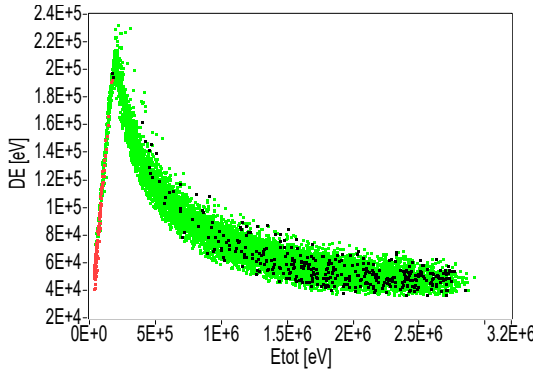

(b) DE vs E_{tot} scatter plot

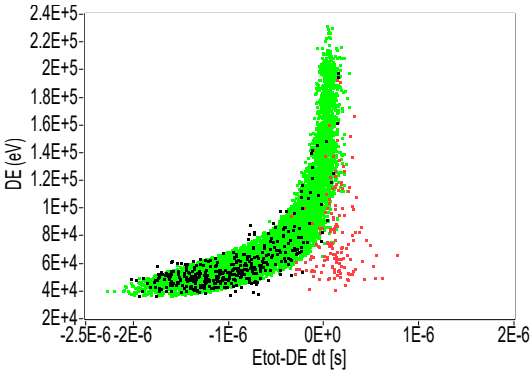

(c) dt between DE and E_{tot} plot

Figure 3.17. Interpretation of ACSpect measurements. The $t_{E_{tot}} - t_{PM}$ plot is divided into three regions identified by marking with different colors events occurred in different regions. Events on the other two plots are printed keeping their color-mark.

all of its energy in there. The total proton energy E_p is eventually numerically calculated from L_p by reversing equation (3.2). Figures 3.20 shows the effect of the linearization procedure in the E_scint vs E_{tot} graph. Having now data on recoil-proton energy, the proton spectrum is brought out and the neutron spectrum is calculated using equation (3.7) and conveniently normalized.

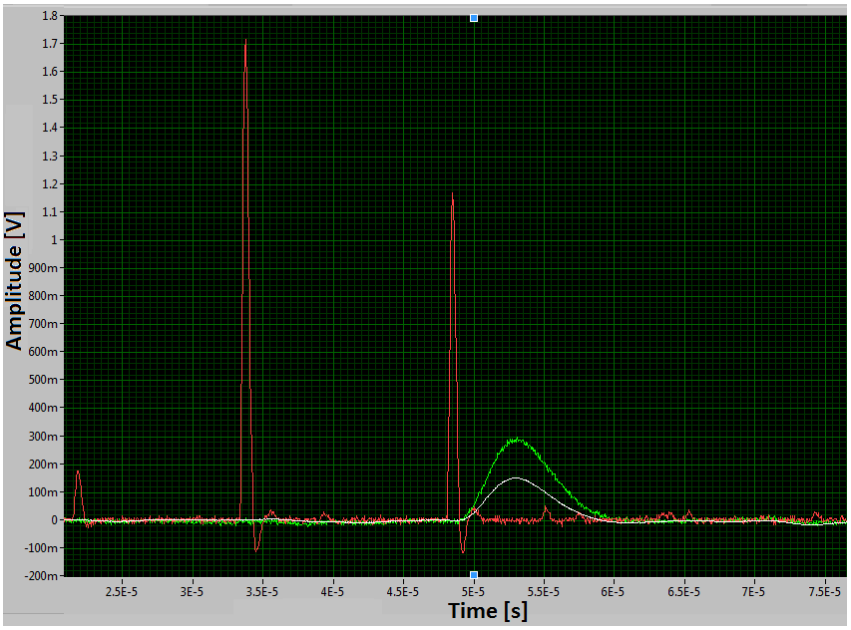

Figure 3.18. Typical signals triplet generated by a neutron. The red signal is the *PM*, the green one is the E_{tot} and the white one is the *DE* signal.

3.3.6 Data elaboration program

The elaboration program is written with Labview and it is implemented trying to make it the most useful and practical for the user. The aim is to have all the tools needed for the investigation of all the elaboration and selections parameters and last but not least to have a practical tool to evaluate and compare the results.
The program has several functions:

- *run elaboration*, starts the actual elaboration; runs the elaboration algorithm a first time and than keeps active the elaboration functions;
  - *re-elaborate*, runs again the elaboration algorithm for successive elaboration needed after changing some parameters;
  - *error analysis*, performs the error analysis on the elaborated results.
- *MST α calibration*, allows performing the calibration of the MST through the measurement of an α source.
- *sum signals*, let you open several measurements data and merge them together as they were performed all in once;
- *read details*, read and set acquisition and elaboration details from a previous saved elaboration or from a saved acquisition;

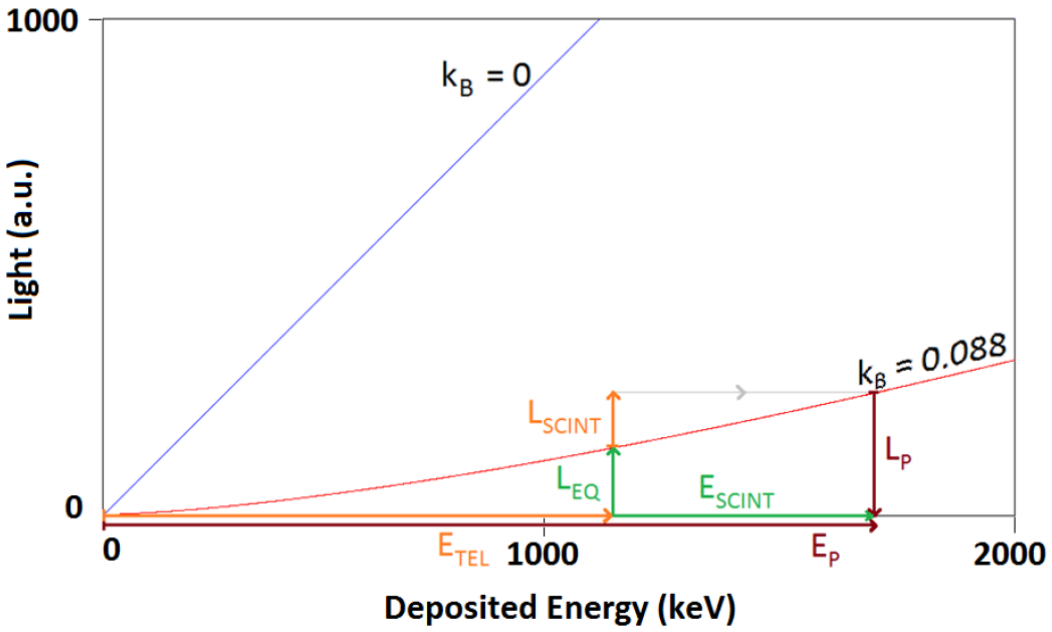

Figure 3.19. *PM* energy linearization procedure, [6].

- *read details + MST calibration*, read and set acquisition and elaboration details and reads also the calibration parameters saved from a MST α calibration;
- *read elaboration*, reads saved elaborations, making all graphs and showing the elaboration results.

Each of the buttons for starting the wanted function has two indicators on the left, one lights if the function is working while the second is green if the user can start the function or red if he cannot. Their aim is to avoid the program crashing happening if the user starts a function while the program is working on other stuff. The *run elaboration* function is the actual elaboration function. It reads the *signals.bin* files indicated by the user and processes the data. The user is supposed to give all proper settings for the signals reading and elaboration. While all elaboration settings are changeable during the elaboration, the signals reading settings are set once for all before running the elaboration. Signals are read, calibrated using the given *calibration parameters* in the equation 3.3, and stored in proper data vectors; acquisition events spectra are plotted for each active channel. A "while cycle" is used coupled to an "event case structure" in order to keep the elaboration on until the user stop it. The cycle starts indeed each time the user changes one of the values activating the "event case". The main algorithm is the whole elaboration one, activated at the first cycle and each time the function *Re-elaborate* is called by

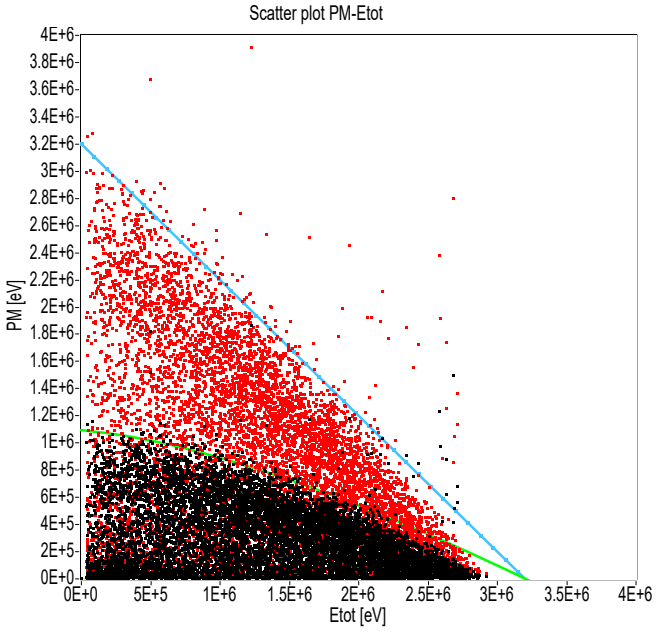

Figure 3.20. *PM* vs E_{tot} scatter plot showing the events distribution before the linearization (black points) and after the linearization procedure (red points).

the user. For each *DE* event, all E_{tot} events within a proper time interval, set by the user, around the *DE* are investigated by the *scatter plot* selection. Scatter plot selection curves are built using the "scatter plot parameters" given as input and only the couples of events occurring within the two curves are selected and kept. For the stopper region, the couples of events selected are those which energies differ less than 5 keV, to consider the experimental dispersion. All events with E_{DE} or $E_{tot} < e^{-}threshold$ are discarded. Couples candidates to be real recoil-proton events are sent to the first time coincidence selection, the $t_{DE} - t_{E_{tot}}$ one. Their location is investigated and if they fit the conditions they are kept. For each MST-couple, all *PM* events occurring within a user-set time interval from the *DE* event time location are investigated and only the one, if it exists, matching the $t_{DE} - t_{PM}$ coincidence condition is selected to form the proton event triplet. A third time coincidence selection could be used if selected by the user [1], the $t_{E_{tot}} - t_{PM}$ coincidence selection we used only for a further check of triplets goodness. A dedicated graphic for each selection is produced plotting all events getting to the considered study together with the curves identifying the selection condition. After the proton triplets are identified, their *PM* needs to be linearized in energy. The Birk's law 3.2

[1] Actually, for all three possible time coincidences the user can select, using the proper drop-down menu, if disabling the selection or enabling it by choosing which type of coincidence to use.

is used to build the Birk's curve and the linearization is performed using the algorithm described previously in this chapter, with a spline interpolation of the Birk's curve for the calculation. The PM vs E_{tot} scatter plot is printed showing both non-linearized events marked with white color and the linearized events marked with red. They are plotted together with up to three mono-energetic non-linearized and linearized curves of given energy. We have now a data vector made up of all proton events and carrying the information on their energy. It is used to build the proton spectrum, using the selected energy binning. The energy bins can be both imported from an Excel file, in order to use non-uniform bins, or uniformly spaced by setting a maximum energy and the number of bins. Finally, using the inverse of equation 3.7 the proton counts for each energy bins are turned to the corresponding neutron counts "at the scintillator". The average energy value of each energy bin is used to calculate the energy-dependent parameters in 3.7. The neutron spectrum obtained is then normalized as selected by the user with the proper drop-down menu and the neutron spectrum is plotted. The integral neutron fluence rate is also estimated by integrating numerically the neutron spectrum. Since the spectrum yield is expressed in $\mu C^{-1}MeV^{-1}sr^{-1}$, the integral fluence is calculated as

$$\phi = \sum_{bins} Y_{bin} dE_{bin} \tag{3.8}$$

where ϕ is the integral neutron fluence rate, Y_{bin} is the *normalized* yield of each bin and dE_{bin} its energy width. A spline fit of the proton spectrum is also performed if wanted and the spline-spectrum obtained converted to a spline-neutron spectrum. Once the first while-cycle elaborates data, the user can start analyze the measurements data and its elaboration. He can change all the *selection parameters* (the parameters building the selection curves), producing an instantaneous change of the curves in the plot being studied; in this way he can investigate and find out the most suitable selection parameters. The parameters change cause the event case to run a simpler code modifying only the related curve in its graph. To actually use the new parameters for the elaboration, the *re-elaborate* function has to be called. If the user changes the neutron spectrum normalization kind or the normalization factors, the program instantaneously modify the final results and spectra. Three additional neutron spectra can be added to the neutron spectrum being elaborated in order to have some comparisons. It can be plot one of the following neutron spectrum:

- *Simulated spectrum (from Excel)*; it is used to plot results from numerical simulations collected properly on an Excel file, a column with the average value of each energy bin on the first sheet and a column with the spectrum yields on the second sheet;
- *Measured spectrum (from Elaboration)*; it is used to plot results from other measurements (or from the same measurement but with a different elaboration) previously elaborated and saved with this elaboration program;

- *Massey* 5 MeV *p on Be*; it plots the neutron spectrum of a 5 MeV proton beam on a beryllium target measured by Massey using *Time of Flight* system [21];
- *Massey* 4 MeV *p on Be*; it plots the neutron spectrum of a 4 MeV proton beam on a beryllium target measured by Massey using *Time of Fight* system [21];
- *Guzek* 4 MeV *d on Be*; it plots the neutron spectrum of a 4 MeV Deuterium beam on a beryllium target measured by Guzek;
- *ISO AmBe source*; it plots the standard ISO for the neutron spectrum of an AmBe source.

Another study that can be performed by the program is the *PM* calibration study, of which it is written in section 3.5.2. During the elaboration run, the *error analysis* function can be called by the proper button. The error analysis is obviously essential to have meaningful results. The uncertainty on the neutron spectrum yield is the most tricky to be calculated. In order to avoid issues related to the non-linearity of the relation between recoil-protons and neutrons, the uncertainty is calculated starting from the proton counting. The uncertainty of each bin is the intrinsic standard deviation due to the Poissonian statistics governing the physical process. Indeed, Poisson probability distribution describes the probability that in a counting measurement, the number of counts N is exactly the number of events occurred. Making x different measurements, they distributes according to a Poissonian. Therefore, assuming that our single measurement is the mean of the distribution, the standard error is $\sqrt{N}$. A kind of sensitivity analysis is performed on both the m_{PM} and the proton counts yield allowing to propagate their uncertainties through the non-linearity. The algorithm considers a certain given number N_m of m_{PM} values between the value used for the elaboration and its uncertainty limits $m_{PM} \pm \varepsilon_{m_{PM}} m_{PM}$. For each of these values it makes the linearization and calculates the proton energy spectrum. For each of these spectra, a proton counts yield is generated according to the Poisson probability density function for each energy bin. The spectrum generation is perfromed N_P times each different m_{PM} value; so we handle $N_{spectra} = N_m N_P$ different proton spectra being randomically generated within the uncertainty ranges of the *PM* calibration value and of the measured spectrum. From all the $N_{spectra}$ proton spectra their corresponding neutron spectra are calculated. The mean value for each energy bin is estimated together with its standard deviation and these values are taken as final yield results and their uncertainties. The other uncertainties taken into account are on:

- ACSpect distance from the target (where neutrons are produced);
- integral accelerator charge used for the measurement or measurement time;
- sensitive detection area, $\varepsilon = 2\%$;

- distance between ACSpect box and the scintillator, $\sigma = 0.02\,\text{mm}$.

Taylor's error propagation, [35], is performed between the above mentioned errors considered in order to have the final results with its overall uncertainty. The final result with yield uncertainties is plotted in a dedicated graph. The mean relative error between all neutron spectrum bins is also provided. In the framework of the error analysis, up to three different energy bins can be studied together and compared to investigate the best energy binning.
When the user stop the elaboration through the dedicated "stop" button, it is asked if save the elaboration or not. If saved, all elaboration details and graphs are saved as well as the energy binning and the integral neutron fluence.
The initial part of the *MST α calibration* function algorithm is equal to the *run elaboration* one as measured data has to be read from their *.bin* files. Obviously, since the calibration is made by measures of α, which stopping power is very strong so they have a really short range in matter, the measurements are carried out using only the MST disabling the scintillator; so we have only two active channels. Once data are read the vector are sent to a while-cycle coupled to an event-case. This time the event-case is activated by changing the *Calibration parameters*. The program performs a dedicated $t_{DE} - t_{E_{tot}}$ selection if enabled by the user and it plots the measured events together with the known characteristic scatter plot curve for α in this Silicon telescope. Changing the calibration parameters, data are calibrated and plotted again. When a good matching between experimental data and the known-characteristic curve is achieved, the calibration can be saved.

3.4 Set-up and practical information

One of the main characteristic of the new ACSpect is its terrifically simple set-up compared with the other high resolution neutron spectrometers. This feature let it be unique for its adaptability to new and different experimental environments and for its portability. All the needed equipment can easily be transported with a standard luggage box.
The most troublesome equipment to carry is the vacuum-pump. However, laboratories and other facilities usually have vacuum-pumps of their own so it is not needed to carry it with you. The vacuum level needed by the spectrometer to work properly is easily achievable as a $\sim 0.1/1\,\text{mbar}$ pressure is already enough. Small portable vacuum-pump are therefore suitable.
Looking for the bias-supply system in order to minimize noise we found out that batteries are the most stable and less noisy tool. So two batteries to provide the $-6\,\text{V}$ and $150\,\text{V}$ biases and other two batteries, or a potential generator, providing the $\pm 12\,\text{V}$ power supply are needed together with the ACSpect and the vacuum-pump.
As far as the data collection is concerned, the PicoScope-4424 acquisition device

and a PC running the Labview acquisition program are needed. The output channels are linked to the PicoScope device assigning the *DE* to the PicoScope's *A* channel, the *PM* to the *B* and the E_{tot} to the *C*. Table 3.6 summarize the ACSpect needed equipment.

As a good advice, before starting a measurement all ACSpect box clefts should

Instrument	ACSpect neutron spectrometer
Vacuum	Pump suitable to get a $\sim 0.1/1$ mbar vacuum
Voltage supply	± 12 V generator or a 12 V and a -12 V battery 150 V battery -6 V battery
Acquisition	PicoScope multi-channel acquisition device (at least with 3 channels) PC with the ACSpect acquisition program

Table 3.6. ACSpect set-up equipment.

be covered with some black insulating tape in order to prevent external light disturbances on the PMT.

The improved ACSpect set-up is strongly simplified and bulky reduced, as shown by figure 3.21. Fixed amplification settings and incorporated amplification chains give it an outstanding adaptability to different and new experimental environment. Its simple set-up let it be very easy to transport and fast to setting up.

3.5 Spectrometer calibration

The three acquisition channels of the *ACSpect* must be calibrated in energy. Their calibration is fundamental as it is needed to relate electric signals pulse amplitude to the energy the recoil proton deposited to generate the signal. Equation 3.3 relates signal amplitude to deposited energy through the *calibration parameters*.

The ideal *ACSpect* calibration is performed by means of measuring a known monoenergetic neutron beam. At the moment such a calibration have not been performed yet.

Nevertheless, calibrating the MST and the PM separately is possible and it is done in the framework of this thesis.

3.5.1 MST calibration

After several electronic calibrations made using the test-line, an accurate calibration of the MST channels is performed by mean of an α source. The reason why

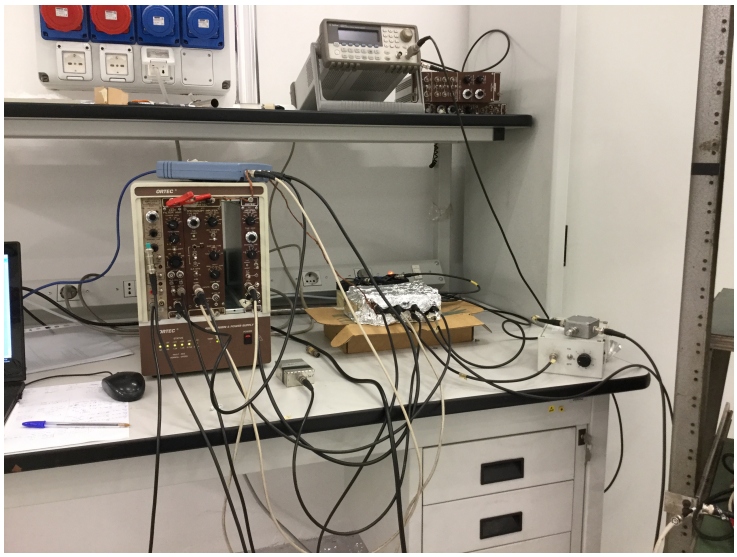

(a) Old ACSpect set-up

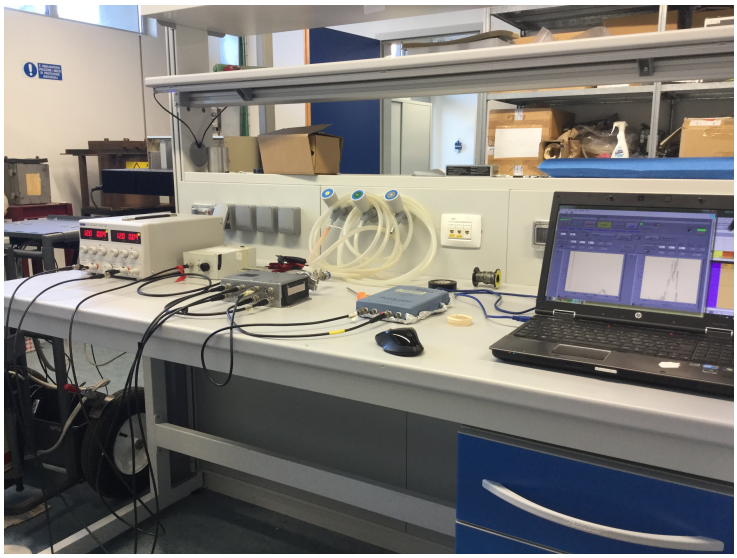

(b) New ACSpect set-up

Figure 3.21. Comparison between the old (a) and new improved (b) set-up. In both the pictures the whole ACSpect chain from the instrument to the PC is shown.

it is more correct is that it take into account all processes and losses taking place from the Silicon crystal to the acquisition and not only of the electronics ones as the test-signal calibration does. The scintillator was displaced to avoid α complete absorption within it. The $^{241}_{95}$Am source of the Nuclear Measurements group was

Coefficient	Value
m_{DE} [eV/ch]	15.8
q_{DE} [keV]	5
$m_{E_{tot}}$ [eV/ch]	150
$q_{E_{tot}}$ [keV]	−5

Table 3.7. MST's calibration coefficients.

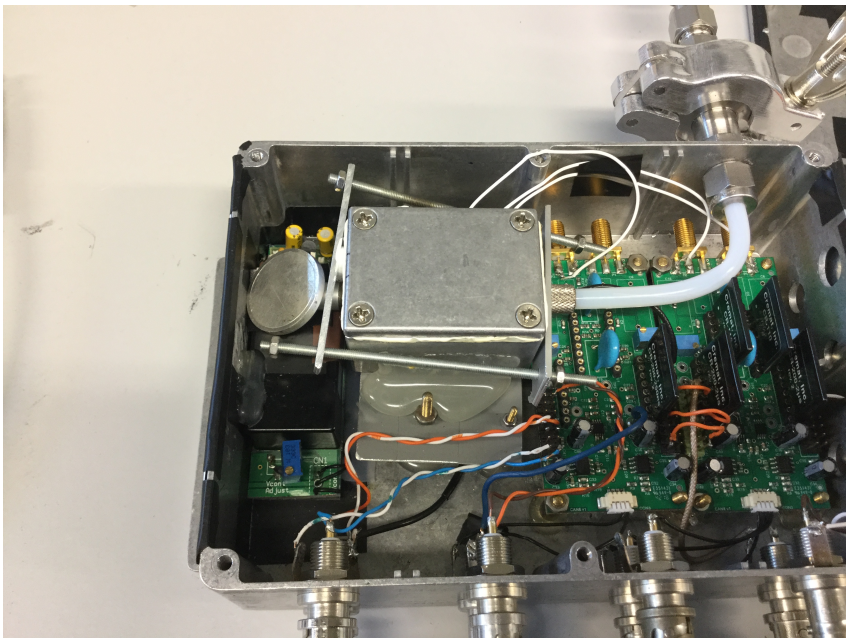

Figure 3.22. ACSpect box opened with the α source placed right in front of the collimator entrance.

used to carry on measurements at the Nuclear Measurements Laboratories of Politecnico di Milano. Figure 3.22 show the ^{241}Am measurements set-up. Since the scatter plot shape due to α particles is a well-known curve of which we have data, the calibration coefficients for the DE and the E_{tot} channels were found by matching the experimental curve with the theoretical one. The calibration coefficients values are shown in table 3.7 and figure 3.23 shows the matching result achieved with these coefficients.

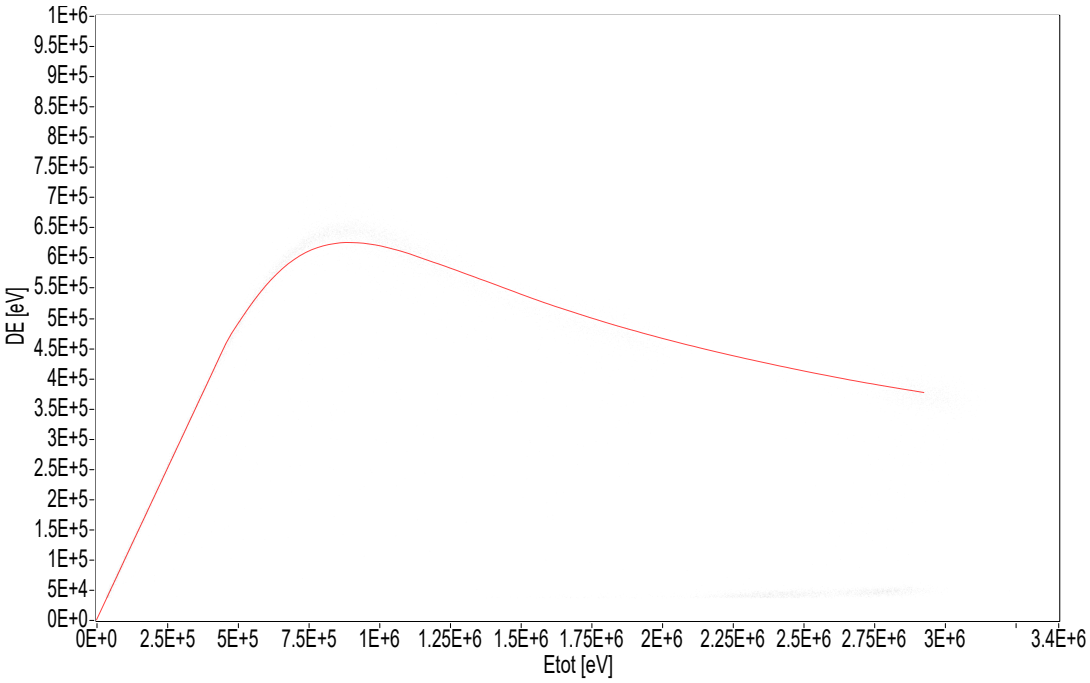

Figure 3.23. α scatter plot by $^{241}_{95}$Am source. Measurements were carried out at the Polimi's *Nuclear Measurements Laboratories*; the red line is the physical model curve.

3.5.2 PM calibration

The optimal calibration of the PM channel would be made by using a known γ source or by measure with the whole spectrometer a known mono-energetic neutron source but it has not been done yet. Therefore a calibration study is made by considering both the PM vs E_{tot} scatter plot and the proton events spectra comparison of the PM and of the E_{tot} channels. The calibration factor m_{PM} is found by checking the PM and E_{tot} energy spectra endpoints coincide [2] and checking the linearized events linear trend. The uncertainty on the m_{PM} is obviously high. We estimated it to be around $\sim 7.5\%$. When the m_{PM} is changed, the PM events vector is re-calibrated by considering the new to old m_{PM} ratio, $E_{PM} = E_{PMold}\frac{m_{PMnew}}{m_{PMold}}$. The linearization is performed on the new calibrated data and the proton energy and the proton and neutron spectra are calculated again.

[2] the PM and E_{tot} channels endpoints are expected to coincide since there is a maximum neutron energy and these two channels energies are complementary so it is expected that both their spectra decrease down to zero getting to the maximum E_n. The endpoints coincidence for calibrated PM is shown in figure 3.24.

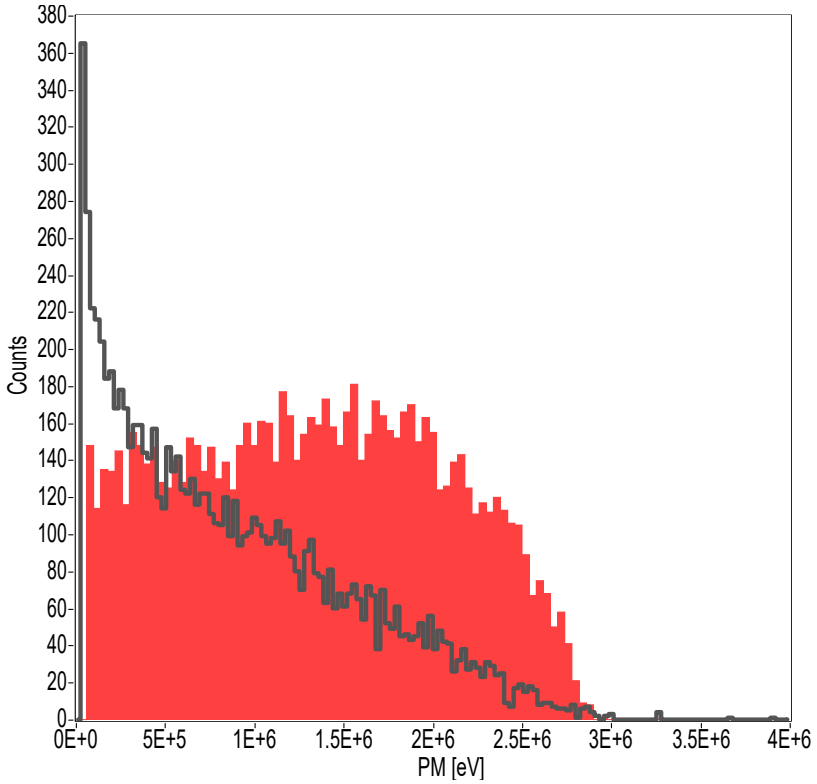

Figure 3.24. The grey spectrum is the spectrum of the energy released by recoil-protons in the scintillator (PM channel); the red spectrum is the spectrum of the energy released by recoil-protons in the E_{tot}.

Chapter 4

Measurements Campaign

Figure 4.1. Van de Graaff CN accelerator building at INFN's LNL.

The experimental work was carried on at the Van de Graaff CN accelerator of the *Laboratori Nazionali di Legnaro* (LNL) of the Istituto Nazionale di Fisica Nucleare (INFN). The measurements campaign involved both the nuclear measurement group of Politecnico di Milano and the BNCT group of Pavia and took us a week, from the 14^{th} of January to the 18^{th} of January 2019. The aim of the experiment was to measure the neutron spectrum emerging from a Be target irradiated with the 5 MeV proton beam of the CN accelerator. Neutron spectra were acquired with increasing thickness of a new moderator material (AlF_3 with Li, 3%

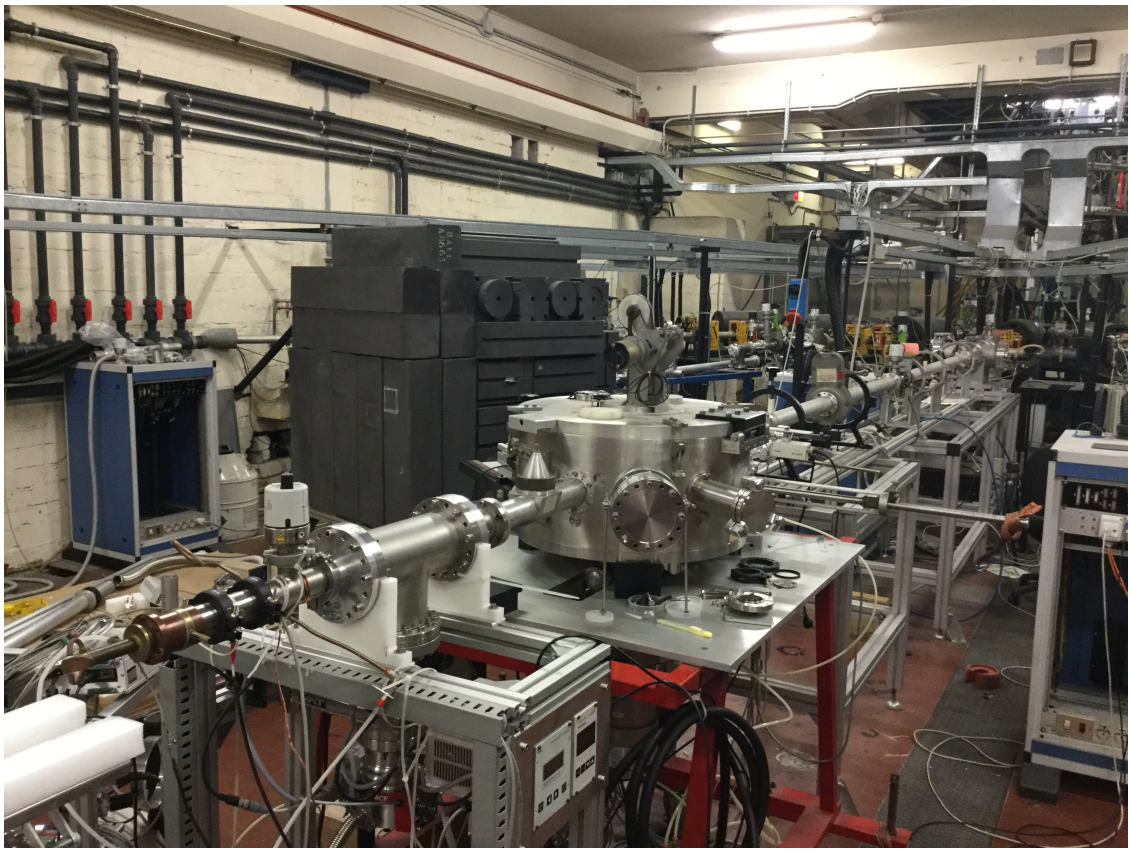

Figure 4.2. CN accelerator experimental room. The focus is on the beam-line we used.

in weight). The attenuation and the moderation of the neutron spectra were also simulated by means of Monte Carlo simulation. The comparison of the simulated and the measured spectra has the purpose of validating the Monte Carlo model. The week before the campaign we had a meeting during which we made a measurements plan. Considering the preliminary Monte Carlo simulations we run with different thickness of the moderator, since we had seven AlF_3 tiles about 1 cm in thickness (details in table 4.1 and figure 4.3), we decided to perform three different measurements, according to the beam-time and beam characteristic available. The first would have been without the moderator, in order to have a measure of the open-flux neutron spectrum to compare with previous experiments [7, 6]; the second would have been with 2 cm of AlF_3 and the third with 4 cm of the BSA. Further we decided to spend the first day by measuring the neutron fluence rate without, with 2 cm, 4 cm and 7 cm tiles using the low resolution spectrometer *DIAMON*, which measurements takes very short time (about 15/20 minutes). By doing so, we would acquire precise integral fluence information and whole-energy range neutron spectra at the price of low resolution. The AlF_3 tiles were sinterized by

the laboratories of Università di Pavia.
The neutron fluence rate is generated by Be(p,χn) reactions of the 5 MeV accelerator-

cross-section shape	circular			square			
thickness [cm]	1.01	1.15	1.18	1.13	0.67	0.86	0.63
diameter or side [cm]	4.95	5	5	5	4.9	4.9	4.9

Table 4.1. AlF_3 tiles details.

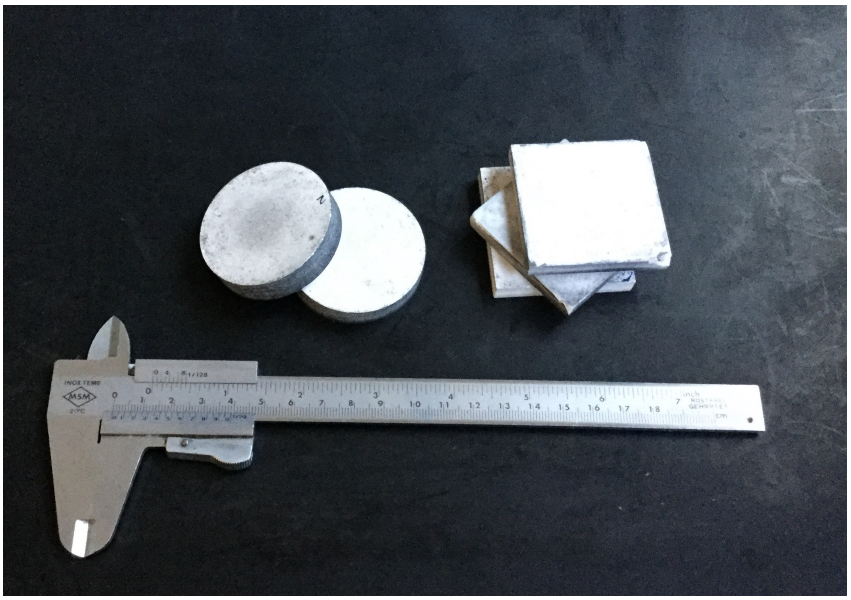

Figure 4.3. AlF_3 tiles used for our experiments.

driven proton beam on a beryllium target, showed in figure 4.11. Neutrons are produced through the contribution of different reactions [7]: ^{9}Be(p,n)^{9}B, ^{9}Be(p,np)2α, ^{9}Be(p,np)^{8}Be and ^{9}Be(p,nα)^{5}Li. From the kinetics of these reactions it comes out that the maximum neutron energy is about 3.2 MeV.
Since the ACSpect efficiency is very low ($\sim 10^{-6}$), we asked for a proton current of 500 nA. Unluckily the CN accelerator was not working properly. The Hydrogen source from which the protons are usually extracted [1] was out of order. Protons were therefore extracted from the Helium source H-waste. Moreover, the beam was focused through two focus of which only one of them was working. Despite

[1] Van de Graaff accelerator extracts the particles to be accelerated from a proper source turned into its plasma state.

all these problems the CN could provide 30 nA of 5 MeV protons, so we could to perform our measurements. Obviously our measurements plan had to be reviewed since the proton current was more than one order of magnitude lower than expected. We decided to carry on measurements with *DIAMON* as planned since, being fast proceeding, it would not have been affected in significant way by the lower proton current. As far as the ACSpect is concerned instead, its very low detection efficiency would have felt heavily the much lower current, strongly slowing measurements time down. We decided to proceed anyway by doing a first measurement without the moderator and then a second putting two AlF_3 tiles for a total of 2.16 cm of moderator thickness. In order to have adequate statistics for both, the measurements went on overnight too. By remaining in the facility also during the night, the accelerator had not been shut down. This contributed to succeed in keeping the proton current stable at about 40 nA as a shut down could have been critical. The CN operator could keep a stable proton current that sometimes reached 50 nA.
As soon as we completed the work with the *DIAMON* we set up and started with the ACSpect. After the first night of measurements, thanks to the possibility of live-monitoring the detection with the acquisition program, we became aware that several *PM* signals were saturating at 8 V, the electronic board saturation limit. Further we saw that the *PM* was not well sampled. This latter problem could have been fixed by increasing the acquisition sample rate or by increasing the amplifier shaping time. Since we were already using the maximum sample rate affordable with the Picoscope used, we changed the Cremat amplifier from a 100 ns shaping time one to the 250 ns one, then definitively kept on. Further to fix the saturation issue, since lowering the channel trimmer did not solve the problem, we decided to make a change in the instrument electronics by-passing the buffer between the amplifier exit and the electronic board output that is responsible of a further x2 gain factor over the amplifier gain. By doing so the *PM* signals decrease down the limit and the saturation problem was fixed. Once we overcame these initially issues, measurements kept on trouble-less allowing to increase the moderator thickness, adding an additional slab of 1 cm (more thickness than the 2 cm measured would have attenuated the flux too much).

4.1 Set-up and measurements

In this section, the experimental set-up used at the LNL's CN accelerator is described together with the several measurements performed.
The spectrometer used is placed in the experimental room. When the accelerator is operating and the beam-line is activated the access to the experimental room is inhibited. The room is closed with a thick concrete door which is interlocked against the accelerator operation. All expected monitoring and controls have to be operated remotely.

The facility is equipped with an integral charge counter. It measures the integral proton charge striking the beryllium target and it accounts for all current variations. The charge information is primary to normalize correctly the results. The counter displays an integer number corresponding to 10^{-8} C.
The neutron fluence rate source, that is the beryllium target assembled on the proton beam-line output, is 124.5 cm above the ground. The target is cooled by compressed air.

4.1.1 DIAMON

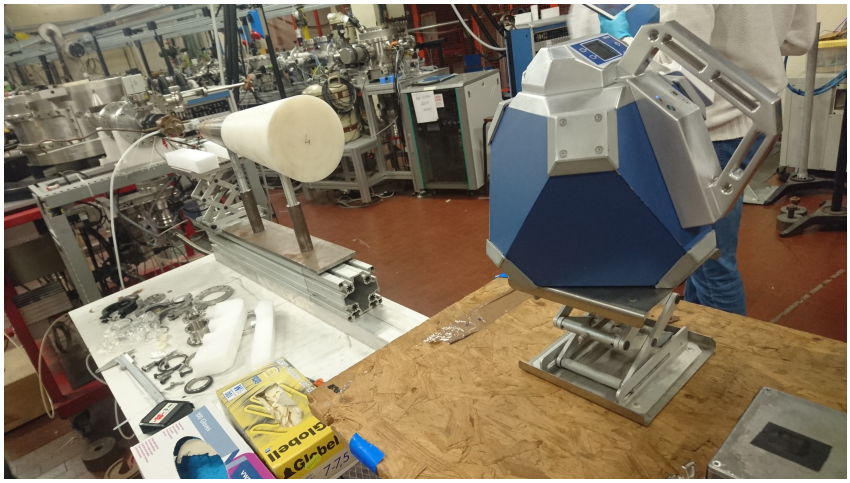

Figure 4.4. *DIAMON* spectrometer placed for measurements at LNL's Cn accelerator experimental room.

The *DIAMON* was placed at 130 cm from the beryllium target and centered at the 0° direction with respect to the beam-line, as shown in figure 4.6. Measurements were carried out without and with three different AlF_3 thicknesses. Table 4.2 lists the configurations of the experiment. The moderator was placed 2 cm downstream of the beryllium target, as shown in figure 4.5. The instrument was remotely controlled through a Wi-Fi connection.
Since the spectrometer was quite far from the neutron source, the scattered and background components become relevant and have to be accounted for. Therefore, for each different thickness, we measured both the overall spectrum and the scattered component by placing a shadow cone between the moderator and the instrument. The cone was placed centered, in-line with the beam-line direction and 20 cm downstream of the Be target. The cone is 50 cm long, the first 20 cm are made of iron while the last 30 cm are made of polyethylene. Two or three sets of measurements were taken for each distance with and without the shadow cone.
The accelerator provided for all measurements 5 MeV protons with a stable average

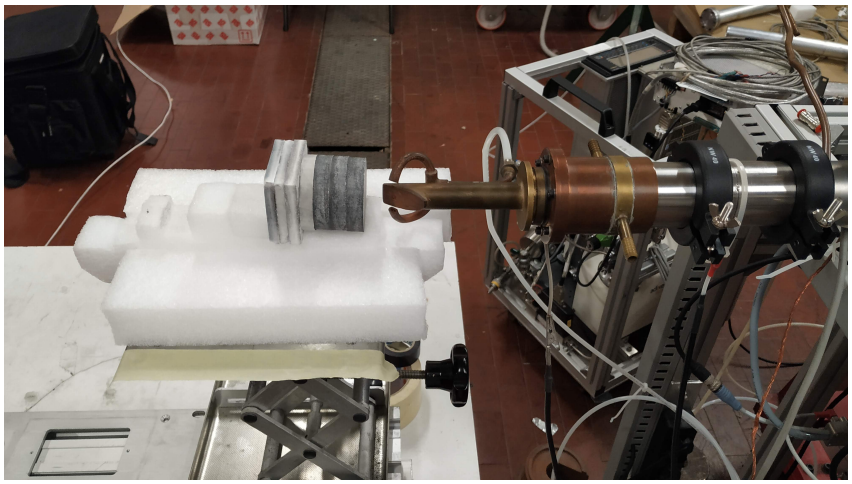

Figure 4.5. Example of the *DIAMON* set-up, focus on the moderator tiles. Six AlF_3 tiles are set-up for a total of 6.63 cm thickness in the beam direction.

current of 35 nA.

AlF_3 thickness [cm]	0	2.16	4.47	6.63
integral charge [μC], overall spectrum 1^{st} set	15.24	15.15	20.36	19.39
integral charge [μC], overall spectrum 2^{nd} set	13.94	15.13	23.62	22.08
integral charge [μC], overall spectrum 3^{rd} set	10.92		10.12	8.55
integral charge [μC], scattered component 1^{st} set	21.33	20.52	27.23	21.16
integral charge [μC], scattered component 2^{nd} set	15.09	16.73	17.37	17.28
integral charge [μC], scattered component 3^{rd} set	16.56			12.97

Table 4.2. *DIAMON* measurements information. The "integral charge" is the integral proton charge got to the Be target in the measurement time.

4.1.2 ACSpect

The *ACSpect* was placed as close as possible to the beryllium target in order to have the highest counting rate. The spectrometer was placed at 2.16 cm downstream of the beryllium target, thus allowing to position the 2.16 cm thick moderator in between during the second irradiation. In order to center and align the *ACSpect* with the beam-line as shown in figure 4.8(a), the position of the scintillator sensitive area was indicated on the instrument external front face.

The experimental set-up is shown in figure 4.9. All supporting devices were placed on a table beside the spectrometer. A stabilized voltage power supply has been used

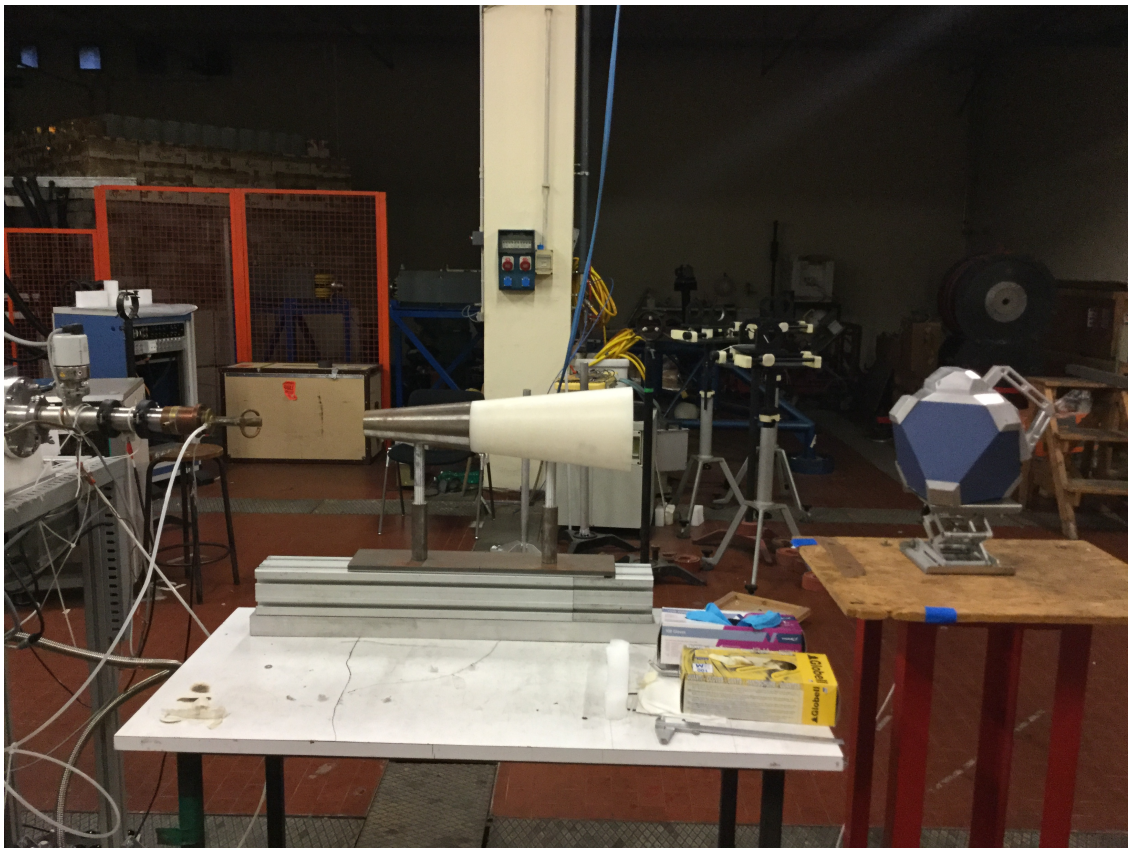

Figure 4.6. *DIAMON* set-up for scattering component measurements. From the left to the right there is the end of the proton beam-line with the Be target assembled, the shadow cone and the *DIAMON* spectrometer on the right.

to provide the ±12 V supply; two different series of batteries have been used to provide the two biases voltage; the PicoScope-4424 has been used as acquisition device, connected to a PC running the acquisition program; a vacuum-pump has been used to put the MST and the collimator under vacuum. All the set-up tools, but the vacuum-pump, were brought by car from Politecnico di Milano nuclear laboratories to the CN facility in a single rigid-box together with the ACSpect. Since the PC connected to the acquisition device was inside the experimental room, we made a remote connection via LAN. Table 4.3 lists the set-up used for this experiment.

All measurements were carried out on the neutron fluence rate generated by 5 MeV protons on the Be target. The average stable proton current was about 40 nA. Measurements were performed for four days and four nights continuously and they were saved every two hours in order to avoid losing measured data for any problem on the PC, acquisition program, ACSpect, accelerator or charge counting and any other issue. Table 4.4 lists the three different experimental configurations,

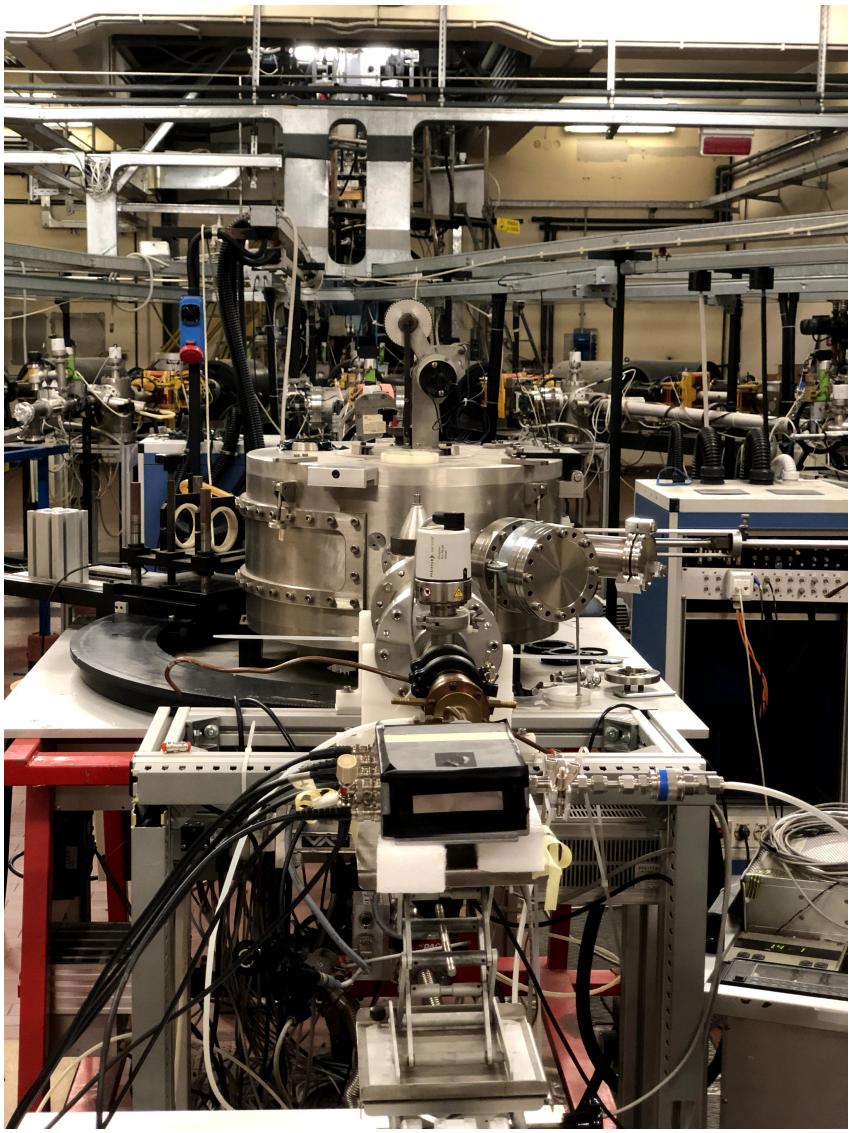

Figure 4.7. *ACSpect* spectrometer placed for measurements at LNL's Cn accelerator experimental room.

shown in figure 4.10.

It should be stressed that the experimental results are very remarkable by considering the very low current of protons which could have been extracted from the accelerator.

By the way, a second measurement campaign would have been impossible before the end of the year, because the accelerator required heavy maintenance.

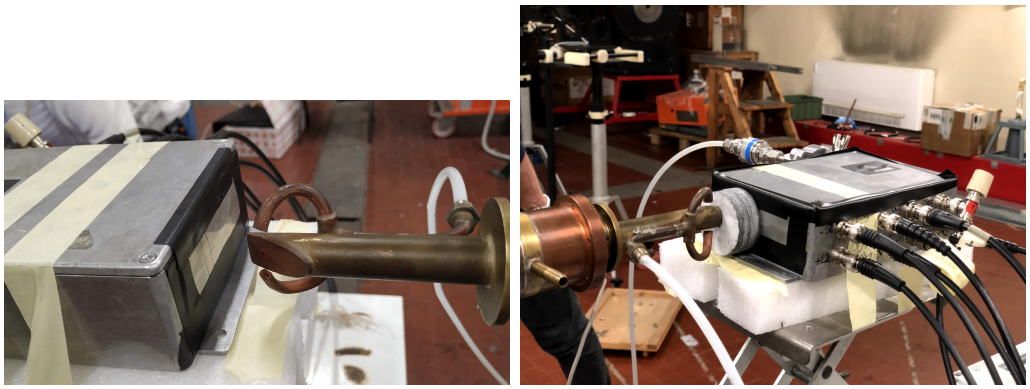

(a) (b)

Figure 4.8. *ACSpect* placed for measurements: (a) without any moderator; (b) with two AlF_3 tiles (2.16 cm).

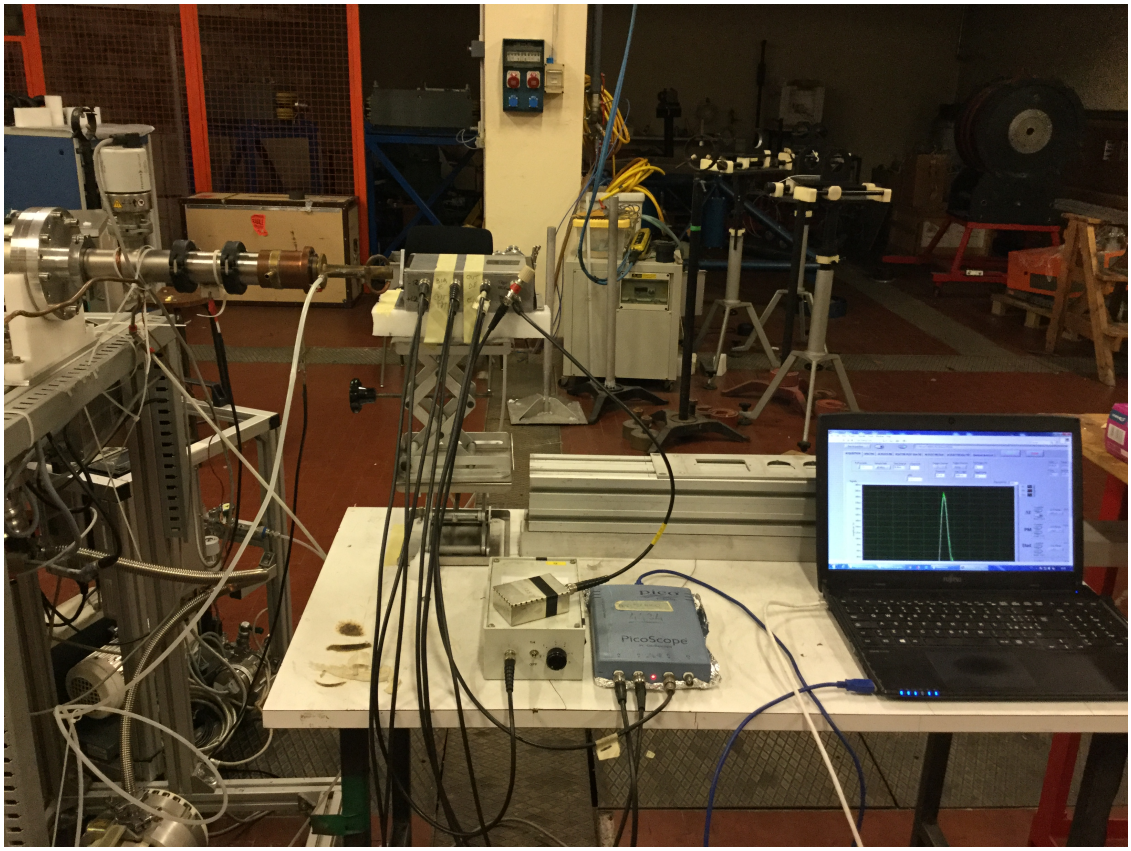

Figure 4.9. *ACSpect* set-up in the experimental room of the LNL's CN accelerator.

Set-up quantity	Value
Power supply [V]	± 12
$p+$ bias [V]	-5.6
E bias [V]	142
Vacuum pressure [mbar]	1.60×10^{-1}

Table 4.3. ACSpect set-up quantities used during this measurements campaign.

AlF_3 thickness [cm]	0	1.15	2.16	0
Be target - AlF_3 distance [cm]	-	0	0	-
Be target - *ACSpect* distance [cm]	2.16	2.16	2.16	2.16
trigger channel	DE	DE	DE	E_{tot}
trigger threshold [mV]	30	30	30	-50
channel DE range [V]	± 0.5	± 0.5	± 0.5	± 0.5
channel PM range [V]	± 10	± 10	± 10	± 10
channel E_{tot} range [V]	± 5	± 5	± 5	± 5
integral charge [μC]	2154.34	3537.64	4550.38	314.78

Table 4.4. *ACSpect* measurements information. The "integral charge" is the integral proton charge got to the Be target in the measurement time. The negative value for the E_{tot} trigger is due to the fact that their pulse are negative, since the $p+$ electrode collects holes instead of electrons as done by the DE, and they are inverted during the processing after the acquisition.

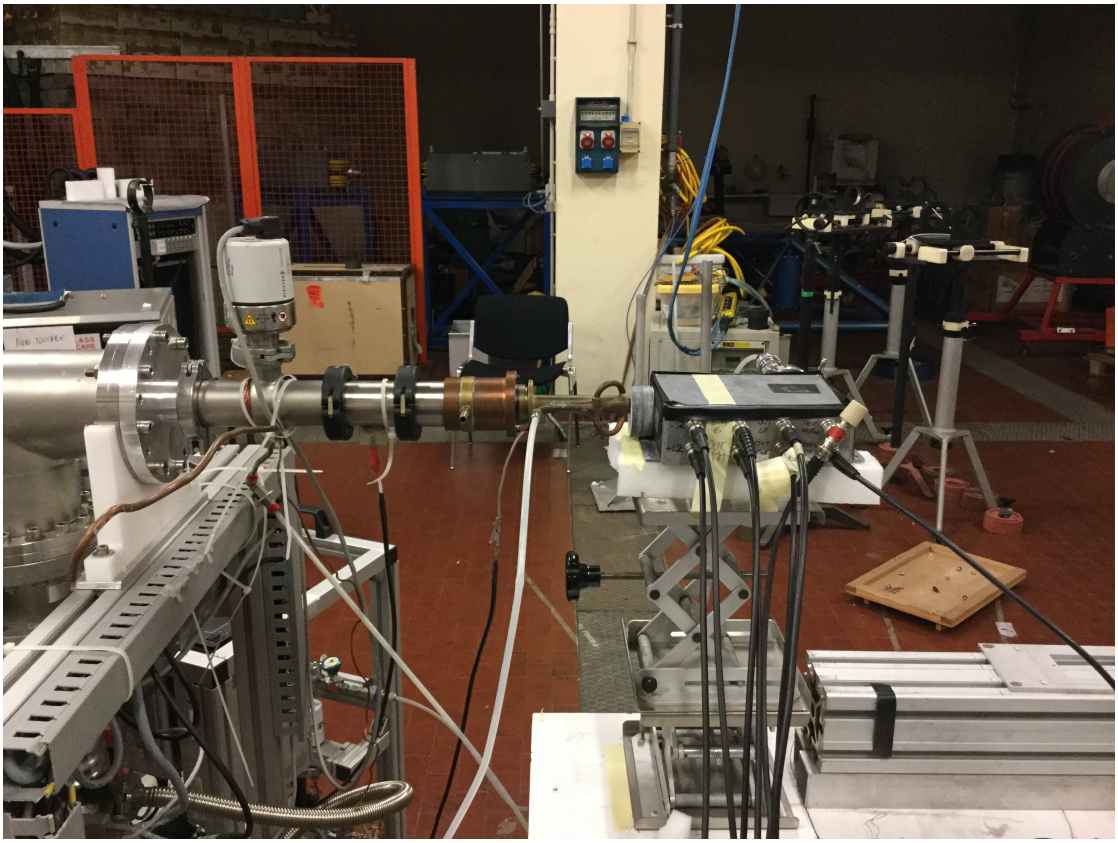

(a) 2.16 cm of AlF_3

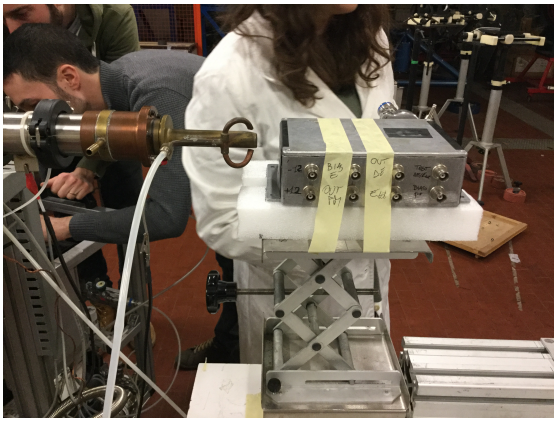

(b) without moderator

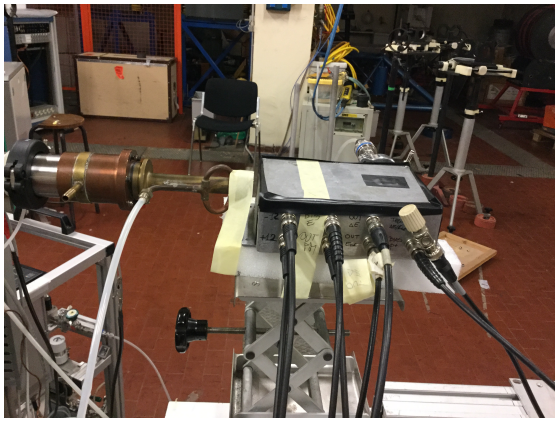

(c) 1.15 cm of AlF_3

Figure 4.10. *ACSpect* set up in the three different measurements configurations.

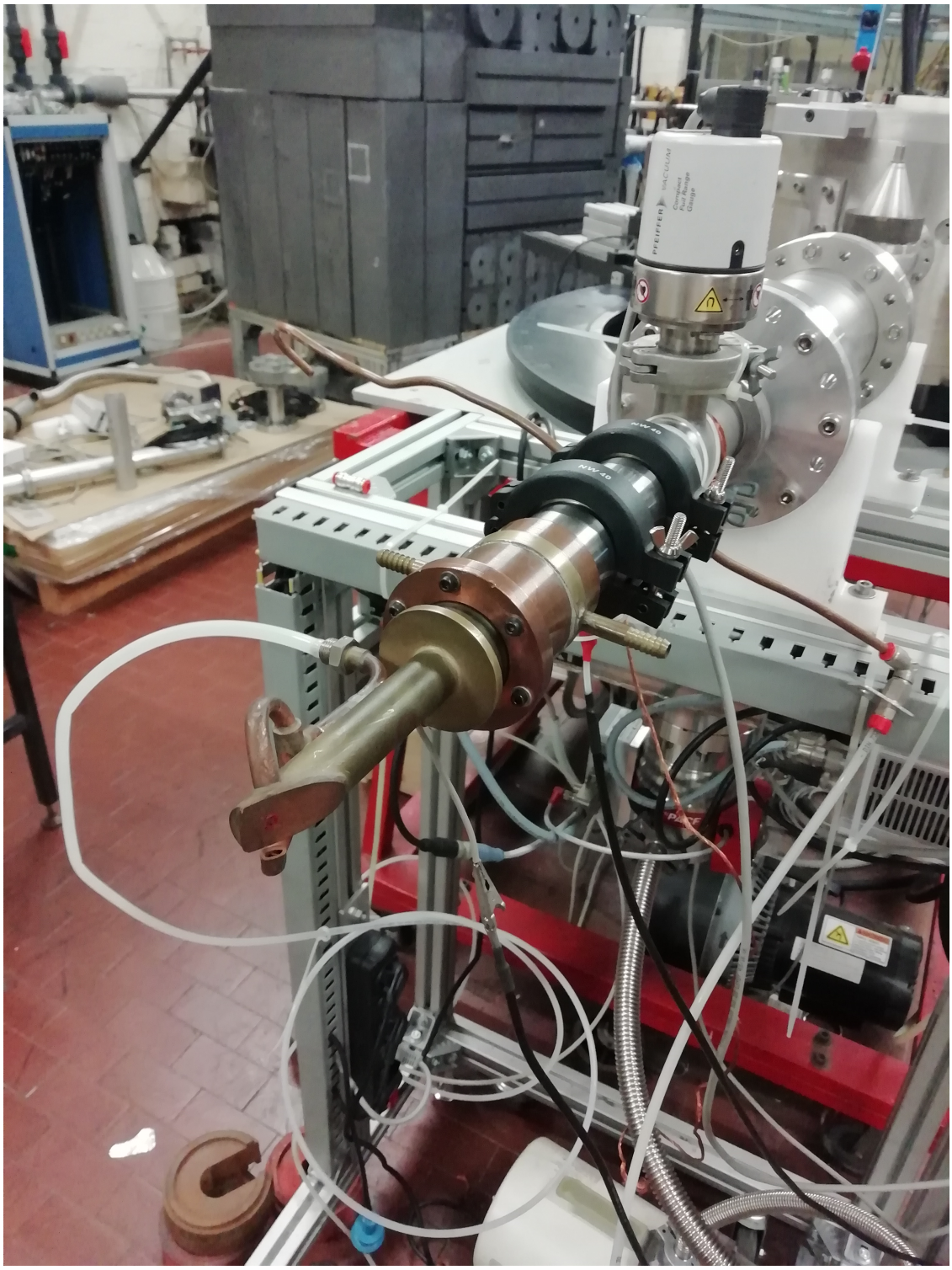

Figure 4.11. Be target assembled on the beam-line output.

(a) (b)

(c) (d)

(e) (f)

Figure 4.12. *ACSpect* setting up.

Chapter 5

Monte Carlo Simulations

In this chapter, the Monte Carlo simulation work is described. The simulations were performed to support the experimental results in the characterization of the AlF_3 as neutron moderator for BNCT applications. Moreover, the validation of simuations by experimental measurements allows the use of a robust model for further calculations. In fact, it is the first time that a neutron moderator made up of densified aluminum fluoride with lithium has been obtained and tested under a neutron beam. An overview on the numerical model used and an overlook on the variance reduction technique used for longer simulations are given and their post-processing is presented.
All the simulations were performed with the *MCNP6* code, using a licensed computer owned by the physics department of the Università di Pavia with which I am collaborating. $MCNP^{TM}$ is a general purpose, continuous-energy, generalized geometry, time dependent Monte Carlo radiation transport code designed to track a lot of particle types over broad energy ranges [27]. The code is trademark of Los Alamos National Security, LLC. It was developed by two Los Alamos National Laboratory's (LANL) teams: the LANL's X Computational Physics Division, Monte Carlo Codes Group and the Nuclear Engineering and Nonproliferation Division, Systems Design and Analysis Group. MCNP6 is considered the gold standard among the Monte Carlo codes concerning coupled neutron-photon-electron transport. The code can also simulate the transport of other charged particles and it is used in many applications. Some of these applications are listed in the following:

- medical physics, especially proton and neutron therapies
- nuclear reactor design
- nuclear criticality safety
- design of accelerator spallation targets, particularly for neutron scattering facilities

- accelerator based imaging technology such as neutron and proton radiography
- high-energy dosimetry and neutron detection
- charged particle propulsion concepts for spaceflight

and many others [27].
Three types of simulations were set up: the preliminary ones to help us defining the measurements plan by predicting the neutron fluence rate attenuation with the moderator thickness, the second one simulating the exact experimental configurations to check the validity of the simulation results, and the "thicker-moderator" ones to investigate the effects of thicker AlF_3 layers on the neutron spectrum. All the simulations have been optimized in order to be as reliable as possible from the point of view of statistical convergence and to be as efficient as possible.

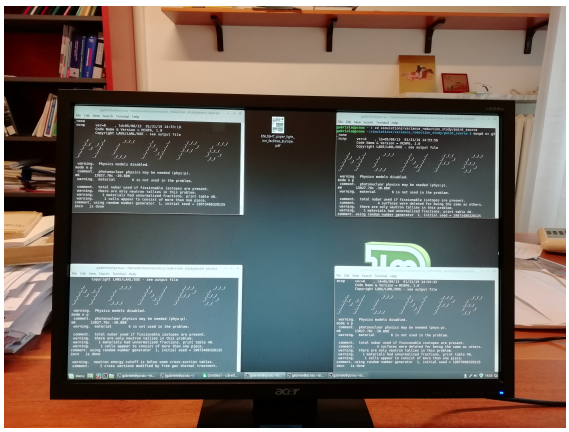

Figure 5.1. Simulations running.

5.1 Numerical model

MCNP6 requires the user to provide an accurate input file that defines the problem giving instruction to the code for calculations. The following items should be defined in the input file:

- the problem geometry
- the materials
- the radiation source
- the tally

Further, the user must indicate the transport model to be used, the simulation-run stopping conditions and the variance reduction, if necessary.
The *tally* is how MCNP calls the volume or surface element in which he calculates and scores the results. In this thesis, the variable parts of the simulations have been the geometry (changing with different detector set-ups and different moderator thickness), the energy binning of the tally (depending on different detectors) and the stopping conditions (to achieve convergence).
The *transport model* uses by default the MCNP6 libraries to get the radiation transport information. Neutrons and photons were transported in these simulatoins. MCNP transports by default also the anti-particle of the particles it is set to transport. Analog capture was set for neutrons, thus stopping neutron transport for each absorption[1]. Moreover, to process all nuclear interactions, the use tables for each nuclide is set where available otherwise using physics models. Recoil ion transport form neutron elastic scattering was disabled. The simulated *materials* were: air and lithiated AlF_3. Tables 5.1 and 5.2 list the materials properties.

Three different energy bins were used for each simulation type. The prelimi-

Air	
Element	Atomic fraction [%]
$_{6}$C	0.0125
$^{14}_{7}$N	68.69
$^{16}_{8}$O	30.1248
$_{18}$Ar	1.1717
density [g/cm^3]	0.001 124

Table 5.1. Air compositions and density.

nary simulations have a fine uniform energy binning from 4 MeV to 10 keV, with $dE_{bin} = 30$ keV; the LNL measurements comparison simulations have the same energy bins used for the measured spectrum; the thicker-moderator simulations have instead a energy binning useful to investigate the spectra at lower energies using a bins-per-decade energy binning.
Finally, the stopping condition is set in terms of "nps", the number of particle-histories. The calculation terminates when the requested nps have been transported. The number of histories is set in order to achieve reasonably accurate statistics. As suggested in [26], an uncertainty below 5% can be considered reliable, up to 10% acceptable and above 10% not meaningful. Therefore the number

[1] in contrast, non-analog transport (being a variance reduction technique) decreases the weight of each particle undergoing capture without stopping its transport.

Lithiated AlF_3	
Element	Weight fraction [%]
$^{27}_{13}$Al	30.88
$^{19}_{9}$F	66.6
$^{6}_{3}$Li	0.189
$^{7}_{3}$Li	2.331
density [g/cm^3]	3

Table 5.2. Compositions and density of the AlF_3 tiles used for our measurements.

of histories was set in order to give uncertainties below 5% in each energy bin. MCNP6 prints out an output file in which, together with the results, there are several information on the calculation and some statistical check the user has to care to be sure the calculations did not get into bad troubles and the statistics is correct. All results that will be presented have passed all statistical and common-sense checks.

5.1.1 Neutron source

The neutron source used reproduces the neutron yield from a 5 MeV proton beam on a beryllium target. As demonstrated by Ian Postuma [30], most of the codes did not give reliable results for neutron spectrum when simulating 5 MeV protons striking a beryllium target. Nuclear data in the libraries and the models implemented for the physical processes used by MCNP6 for charged particles are therefore not that reliable as far as our physical problem is concerned. Therefore experimental data were considered for the simulated neutron source. This approach is also more efficient in terms of computational time. Valsecchi in [39] improved a first model of neutron source to test various materials for neutron moderation. The experimental data used for the source are the measurements carried out by Agosteo et al. in [7]. These measurements were performed with the first ACSpect version [8] on 5 MeV proton beam on beryllium target at the CN accelerator of INFN's LNL. The neutron energy spectrum was measured at several angles with respect to the beam direction: 0°, 20°, 40°, 60°, 80°, 90°, 100°, 120°. Figure 5.2 shows some of these spectra. The neutron source in the input code is approximated as a point-like source since the proton beam section-diameter on the beryllium target is small. The source was designed by sampling the flight direction and the energy distribution using the experimental spectra. The emission angle samples are the eight different angles measured in the experiment and their probability is given by considering the integral of the spectra at that angle. For each of them, energy sampling is performed in the same way: the mean values of the energy bins are the

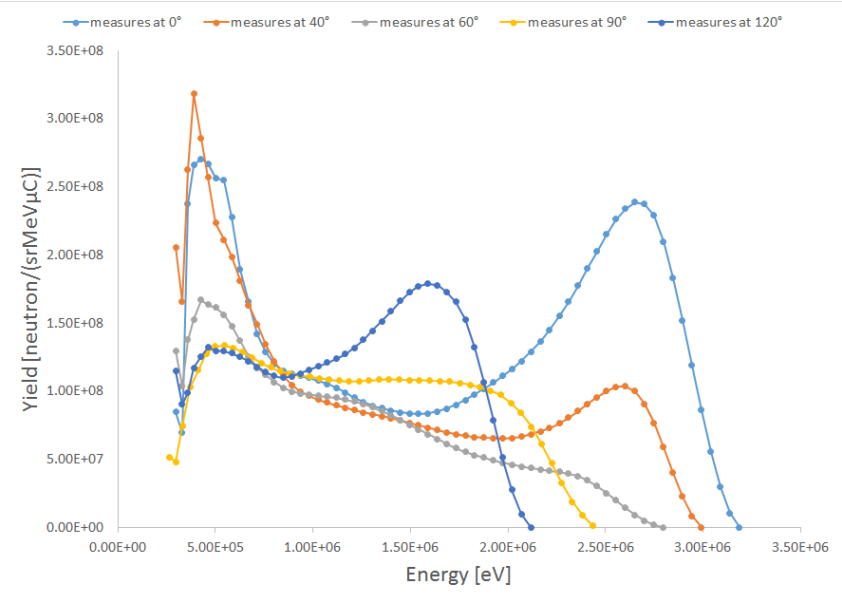

Figure 5.2. Neutron spectra from 5 MeV proton beam on beryllium target at 0°, 40°, 60°, 90°, 120° with respect to the proton beam direction [7]. Courtesy of professor Stefano Agosteo.

energy samples and their simulated emission probability is calculated form the experimental yield. The experimental data were linearly interpolated by the code for generqating neutrons at all angles and energies. The probability distributions are determined on the source intensity, calculated by integrating the neutron spectra over the considered solid angle and energy range. The source intensity turns out to be $2.58 \times 10^9\,\mu C^{-1}$.
It should be mentioned that considering the beam fluctuation, the source cross-section can be approximated to a disk 1 cm in diameter. Since the sensitive area of the ACSpect is also very small ($12.566\,mm^2$) and the spectrometer is placed very close to the target, the goodness of a point-like source approximation is questionable. A disk-like source 1 cm in diameter was therefore implemented to check if the simulation results change significantly. Checking for several moderator thickness, the spectra did not show variations within the uncertainty values and therefore the point source approximation was used for simplicity.
The neutron source used for the simulations is reported in appendix B.2.

5.1.2 Geometry and tally

The problem geometry was implemented by assuming that the contribution of scattered neutrons is negligible. Neutrons could indeed be scattered by any object in

the experiment room and by the room walls and floor. As far as our measurements are concerned, the distance between the spectrometer and the target is so short, the sensible area is so small and the detection efficiency so low that the scattered component should give a negligible contribution to the detector counts. Neutrons can be also scattered by air but the scattering probability is very low so it can be neglected as well. For measurement positions farther from the source (and closer to the room walls), the contribution of scattered neutrons cannot be neglected anymore. The scattered component should be simulated by considering the experimental room geometry. Its contribution to the experimental measured data can be evaluated, instead, trough the shadow cone technique. By considering the assumption of a negligible scattered neutron component, a very narrow geometry suiting the AlF_3 tiles shape and then converging to the tally dimensions is implemented. The scoring region reproduces the shape and dimensions of the AC-Spect sensitive volume, i.e., a cylinder 2 mm in radius and thickness (figure 5.3). The moderator geometry reproduces strictly the tiles used in the experiment, i.e.,

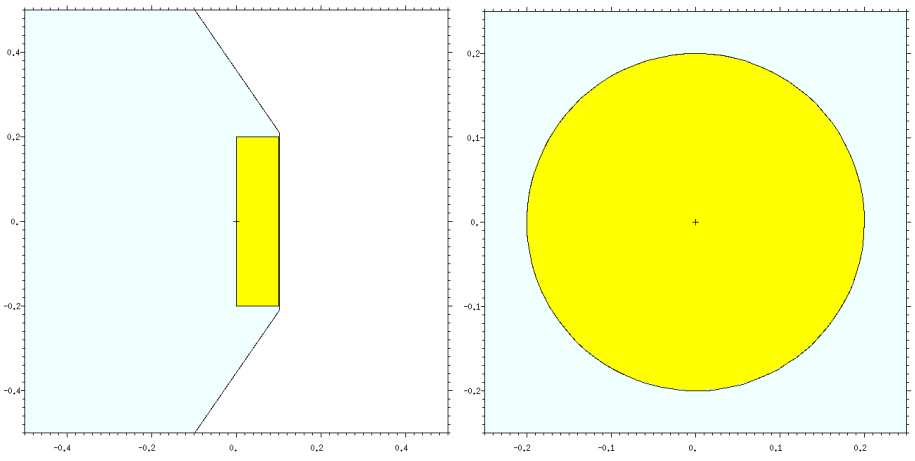

(a) *yz*-section, *z* is the horizontal direction

(b) *xy*-section

Figure 5.3. Geomtry of the tally (colored in yellow). Scales units are in cm.

a cylinder 5 cm in diameter with a thickness corresponding to the one used in the irradiations. Figure 5.4 shows the simulated geometry. In particular, the source was placed adjacently to the moderator. A truncated-conical region filled with air includes the tally volume. MCNP6 has several type of tally calculating different physical quantities. They are indicated in table 5.3. The result of all the tallies is given per unit of source particle. It means that it represents the probability that a particle reaches the tally volume/surface within the considered energy bin, in terms of the physical quantity scored by the tally. Therefore it has not a physical meaning on its behalf but it has to be multiplied by the source intensity to become

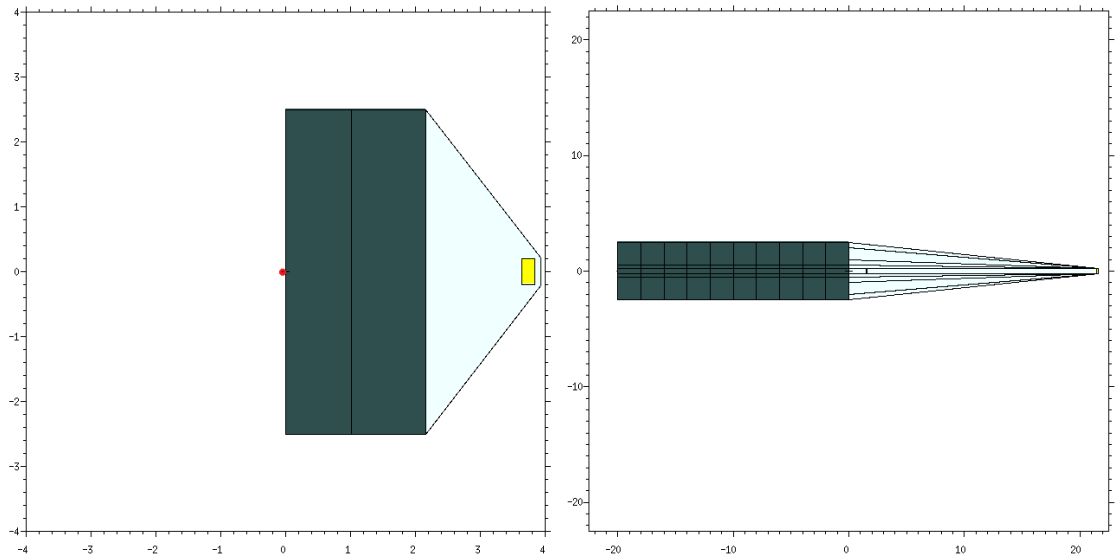

(a) Simulated set-up with the two AlF_3 tiles for the total thickness of 2.16 cm.

(b) 20 cm of AlF_3. The geometry is divided in cells for the variance reduction.

Figure 5.4. Examples of geometry configurations. The AlF_3 is colored in gray, air is colored in light blue and tallies are yellow. The red dot at the beginning of the moderator is the point-like source position. z-axis is the horizontal one. Scales units are in cm.

meaningful. Since the quantity of interest is the neutron fluence, and the spectrometer determines the neutron spectrum by measuring the recoil protons generated by neutrons within the scintillator volume, the tally *f4* is the most suitable. Anyway, some simulations also using tally *f1* and tally *f2* was made as well. The results did not show significant variations for the three tallies which were accounted for. Since the direction of neutrons directly impinging on the detector is very close to the normal to the surface of its very small sensitive area, the current density does not differ from the fluence across that surface. This is also due to the negligible contribution of scattered neutrons which was mentioned above. However, the tally that is conceptually more correct to compare simulations and experimental results is *f4* calculated in the detector sensitive volume.
Geometry splitting and Russian Roulette were considered for reducing the variance. More details will be given in the next section. The geometry and tally input codes of two different geometric configurations are reported in appendix B.1. An important geometric quantity related to the tally is its distance from the source. For the experimental set-up simulations the tally was placed exactly at the distance between the target and the spectrometers; so for the *DIAMON* experimental set-up it was placed at 130 cm from the source while for the *ACSpect* experimental set-up it was placed as it would have been the scintillator so at 3.636 cm (2.16 + 1.476).

Tally name	Calculated quantity	Units
f1	Current integrated over a surface	particles
f2	Flux averaged over a surface	particles/cm^2
f4	Flux averaged over a cell	particles/cm^2
f5a	Flux at a point or ring detector	particles/cm^2
fip5	Array of point detectors for pinhole flux image	particles/cm^2
fir5	Array of point detectors for planar radiography flux image	particles/cm^2
fic5	Array of point detectors for cylindrical radiography flux image	particles/cm^2
f6	Energy deposition averaged over a cell	MeV/g
+f6	Collision heating	MeV/g
f7	Fission energy deposition averaged over a cell	MeV/g
f8	Energy distribution of pulses created in a detector by radiation	pulses
+f8	Charge deposition	charge

Table 5.3. Types of tally in MCNP6.

For bigger thickness instead, two equal tallies at different distances were used. One was placed 1.476 cm downstream of the moderator end, such as the ACSpect would touch the moderator surface; the other, instead, was fixed for all the simulations and it was placed at 41.476 cm.
Table 5.4 summarizes the simulations performed. The "preliminary" simulations were preparatory for the ones used for the comparison with the experimental measurements, without the precision in the set-up geometry. Since we used their results only to assist the measurements plan decision they are not indicated in table 5.4.

5.2 Variance reduction techniques

When thickening the moderator layer, the calculations become increasingly time-expensive. Moreover, since the probability for a neutron to get to the tally decreases as the moderator thickness increases, we would need too many particle histories to have good statistics. Some variance reduction technique is therefore required, in order to obtain statistically significant results in reasonable calculation times. Indeed it has been demonstrated by Booth [15] that variance reduction techniques can increase the efficiency of a Monte Carlo simulation.
It should be mentioned that variance reduction does not introduce any bias but it

	AlF_3thickness[cm]	Tally distance
experimental set-ups	0	3.636 130
	1.15	3.636
	2.16	3.636 130
	4.47	130
	6.63	130
thicker AlF_3 layers	2	3.476 41.476
	4	5.476 41.476
	8	9.476 41.476
	12	13.476 41.476
	16	17.476 41.476
	20	21.476 41.476
	25	26.476 41.476
	30	31.476 41.476
	35	36.476 41.476
	40	41.476

Table 5.4. Information on the Monte Carlo simulations performed.

deals with the statistical weight. The physics of the problem is therefore respected. MCNP6 has several tools to perform variance reduction. All of them work on sampling rather particles considered important for the aim of the calculation than particles "unimportant". The problem is tricky as the aim is to decrease the relative standard deviation of the mean, σ_{mr}, in shorter times. Let's consider fixed computer time and the definition of σ_{mr}:

$$\sigma_{mr} = \frac{\sigma}{\mu\sqrt{N}} \tag{5.1}$$

σ is the history standard deviation, N is the number of particles simulated and μ the mean. If we want to decrease σ_{mr} we can decrease σ or increase N. For fixed computer time, increasing N would mean decreasing the time per history to obtain information and so σ_{mr} is likely to be increased; vice versa, decreasing σ_{mr}, requiring more time per history to have better information, would increase N.
One of the oldest, most effective and most widely used variance reduction technique is the *geometry splitting and Russian roulette*. It works on the spatial domain which has to be subdivided into regions called "cells" in MCNP. To each of these cells a certain *importance* I_n has to be assigned, considering the role, the "importance", the cell has for the particle to get to the tally. The geometry division as well as the importance assignment, have to be done in the best way for the specific problem considered. By assigning different importances, MCNP automatically perform

Russian roulette and splitting. When a particle crosses from cell m to cell n, it computes $\nu = I_n/I_m$, where I_n is the importance of the n^{th} cell, and follows these rules: if

- $\nu = 1$, MCNP continues transport the particle
- $\nu < 1$, MCNP plays Russian roulette: the particle survives with probability ν and its weight is multiplied by ν^{-1} otherwise the particle is killed with probability $1-\nu$. In general, Russian roulette decreases the time per histories, so more histories can be run but it increases the history variance
- $\nu > 1$, MCNP split the particle into ν sub-particles. If ν is not an integer, it must be sampled. MCNP use the "expected value scheme" to sample it. If ν is not an integer the particle can be spit into i or $i+1$ integer particles where $i < \nu < i+1$. The expected value scheme works as shown in table 5.5

Probability	**Split weight**
$p(i) = i + 1 - \nu$	$w_s = w/\mu$
$p(i+1) = \nu - i$	$w_s = w/\nu$

Table 5.5. Expected value splitting scheme. w is the particle weight before the splitting while w_s is its weight after.

This scheme does not conserve weight crossing the splitting surface at each occurrence but it does conserve the "expected" weight. Indeed:

"Expected" weight:
$p(i)n\frac{w}{\nu} + p(i+1)(i+1)\frac{w}{\nu} = w$
crossing weight at each occurrence:
$i\frac{w}{\nu} = \frac{i}{\nu}w < w$
$(i+1)\frac{w}{\nu} = \frac{i+1}{\nu}w > w$

A big advantage comes out using the expected value splitting: the weight of all particles crossing the splitting surface is w/ν, where w is the weight of the particle before the splitting. This leads to another advantage that is: assuming that all particles start in the source cell with importance I_S and weight w_S, in cell j all particles will have weight $w_S\frac{I_S}{I_j}$ whatever random walk they have taken to cell j.
Also other variant reduction techniques were taken into consideration, such as Energy splitting and Russian roulette, DXTRAN, weight windows and weight windows mesh but the geometry splitting and Russian roulette comes out to be the best for our problem. All the other techniques considered were implemented in some test-run but all failed in improving the simulations efficiency. It should be mentioned

that the weight windows technique is effective for the thicker AlF_3 layers, but without any appreciable advantage with respect to the geometry splitting and Russian Roulette. As far as the weight windows are concerned, they merge together the geometry and the energy splitting and Russian roulette principles in a way that the weight of particles is always controlled, thus avoiding over-splitting, that is time consuming, and too heavy particles that may cause large tally fluctuations; see appendix C. Weight windows are usually very effective in problems where the particles weight undergoes big variations. Since in our problem the geometry is very narrow and neutrons hardly fly back and forth varying their weight heavily, the time took to compute them does not win strongly over the statistical uncertainty improvement. As mentioned above, weight windows proved to be more effctive as the AlF3 layer thickness increases. In this case indeed, neutrons undergo a larger number of collisions thus increasing their weight variation. In the next section, the best geometry splitting and Russian roulette configuration is investigated. In the next section, the best geometry splitting and Russian roulette configuration is investigated, considering weight windows as well.
Although the splitting and Russian roulette is easy to use and very effective, it can be abused. An optimal geometry division in cells and importances assignment is of primary importance for the success of the technique. It has been observed that a flat track distribution throughout the several cells is near the optimal configuration. A good argument for this statement can be made by considering an extremely thick slab. For too little splitting (too small importance ratios), the track population will decrease about exponentially and no particles would be able to penetrate the slab whilst for too much splitting (too large importance ratios) the track population will increase about exponentially and a particle history will never end. An important ratio leading to a flat distribution is therefore the best choice. To fulfill this principle, several geometric subdivisions and, for each of them, several importance ratios were tested both with all 40 cm of moderator and without. The optimal geometry subdivisions are showed in figures 5.4(b) and 5.5. These are different for the case with the AlF_3 and the case without. For this reason, the importance pattern has been optimized for the cases with a moderator thickness smaller than the 40 cm, to accommodate the "long-air-layer".

5.2.1 FOM analysis

In order to find the optimal geometry subdivision and importances assignment for variance reduction, several attempts were analyzed and compared. The parameter used in the comparison to choose the most efficient configuration is the *figure of merit* (FOM) defined as

$$FOM = \frac{1}{\sigma_{mr}^2 T} \tag{5.2}$$

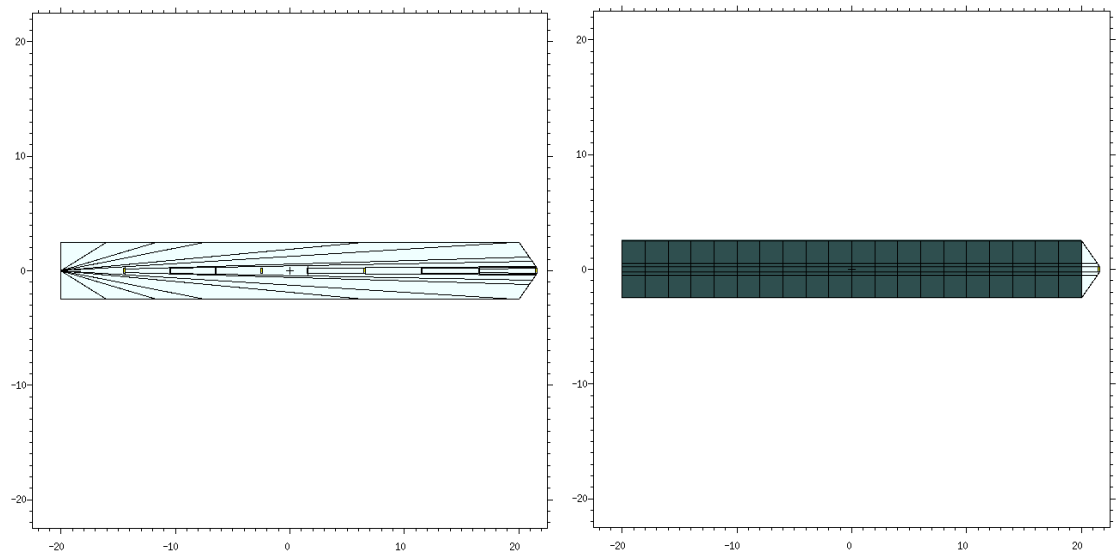

(a) Geometry configuration without moderator (b) 40 cm of AlF_3

Figure 5.5. Examples of geometry configurations with the optimal division in cells for the geometry splitting and Russian roulette variance reduction technique. The AlF_3 is colored in gray, air is colored in light blue and tallies are yellow. z-axis is the horizontal one. Scales units are in cm.

where T is the computational time and σ_{mr} is the relative standard deviation of the mean [15]. It is a good parameter to evaluate the efficiency of a simulation as it takes into account both the computational time and the standard deviation of the mean. The higher the FOM is, the more efficient the calculation is. Furthermore the FOM is expected to be roughly constant for a well-sampled problem. Indeed, from equation 5.1 we know that σ_{mr}^2 is proportional to N^{-1} while T is on average proportional to N; where N is the number of histories run. This latter property let the FOM be used also as a statistical check.
Figure 5.6 shows the considered geometry subdivisions tried and, referring to that figure, table 5.6 reports the FOM coming out from the use of those geometry divisions each one with several importance ratio configurations. The simulation performed for the FOM analysis, since FOM are constant throughout the calculations, run for a much smaller number of histories than the simulations run to get the final results. However, the number of histories was enough to ensure convergence of results avoiding large tally fluctuations occurring at low nps.

For the best FOM-giving configurations an attempt was made using the weight windows, setting the parameters as suggested in [15] and obviously keeping the importance scheme of the configuration. Finally the super-imposed mesh weight windows were used too. It was implemented by doing some iterations using the weight windows generation set to generate mesh weight windows. Figure 5.7 shows

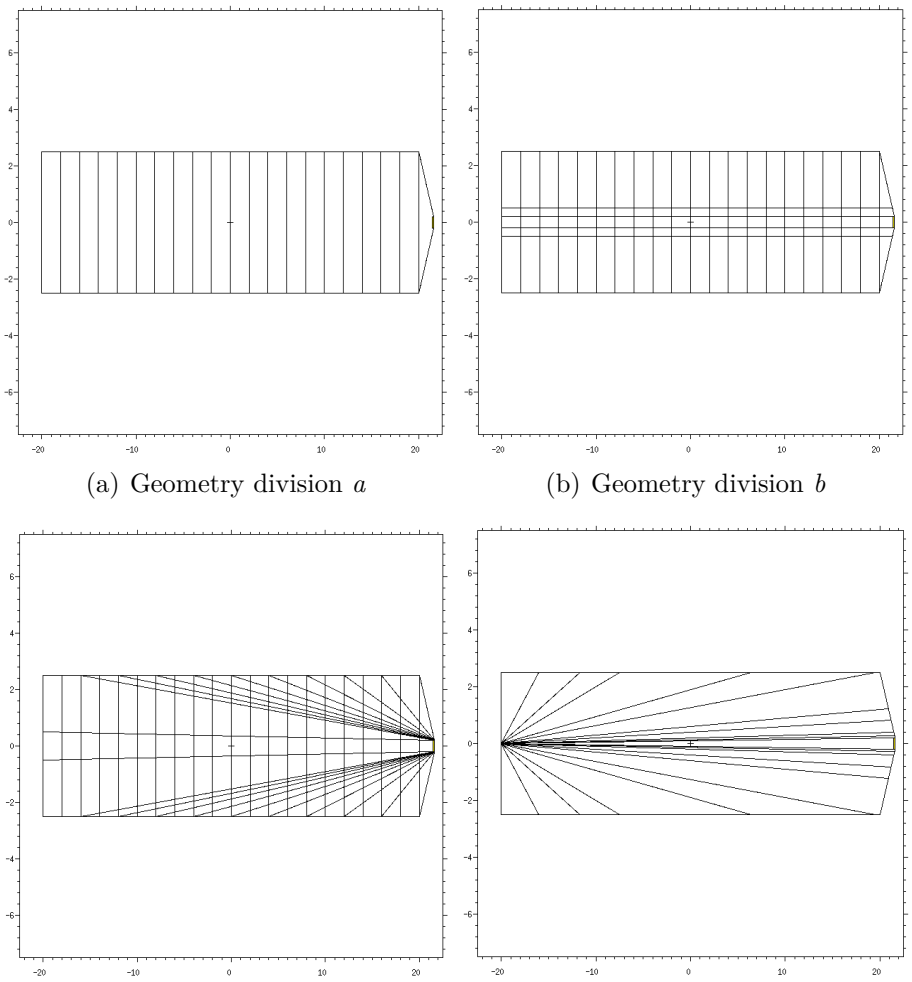

(a) Geometry division *a*

(b) Geometry division *b*

(c) Geometry division *c*

(d) Geometry division *d*

Figure 5.6. Some examples of geometry division in cells for geometry splitting and Russian roulette technique. The division shown in (b) is the best for simulations with moderator whilst the one shown in (d) is the best for simulations without moderator. *z-axis is the horizontal axis* while the vertical one is the r-axis as the geometry is axial-symmetric on z.

the geometry division used for the super-imposed mesh weight windows.

As it is clear from table 5.6, the best configurations for the two cases (without moderator and with 40 cm of moderator) are those shown in figure 5.5 of the previous section. Further it comes up that the use of super-imposed mesh weight windows, despite of being quite effective in general, gives worse FOM than the best configurations of geometry splitting and Russian roulette.

As already said, other geometry splitting and Russian roulette configurations and also other variance reduction techniques were investigated but they are not reported

Geomtery division	Importance scheme	Multiplication factors z axis	r axis	Figure of merit only air	40 cm of AlF_3
None	-	-	-	96	0
a	1	1.5	-	5.8	4.1
	2	2	-	ot	13
	3	2.5	-	ot	1.2
b	1	1.5	1.5	13	3.5
	2	3	3	ot	ot
	3	1.5	3	29	1.8
	4	2	2	ot	20
	5	1.15	3	47	0.029
	6	1.5*	3	41	0.26
c	1	1.5	1.5	16	0.74
	2	1.5	3	31	0.7
	3	1.5	5	37	1.3
	4	2	2	0.66	6.1
	5	2	3	1.1	5.9
	6	2	5	1.4	0.16
	7	2.5	3	ot	2.3
	8	2.5	5	ot	0.67
d	1	-	3	120	9.9
	2	-	2	120	0.72
Weight Windows					
b	4	ww+energy groups		-	20
b	4	ww+1 energy group		-	7.5
d	1	ww+energy groups		71	-
d	1	ww+1 energy group		92	-
Super-Imposed Mesh Weight Windows					
None		simww + energy groups		34	0.064
None		simww + 1 energy group		77	0.13
Best		simww + energy groups		43	8.8
Best		simww + 1 energy group		101	6.6

Table 5.6. Some FOM analysis results. Geometry division identifier refers to figure 5.6. The blue colored solution is the best for simulations with moderator whilst the green-colored solution is the best for simulations without moderator. (*) means that the first five importance ratio were 5, from the sixth on the ratio is the one indicated. "ot", overtime, indicates that the calculation was taking too much time (days with respect to some minutes).

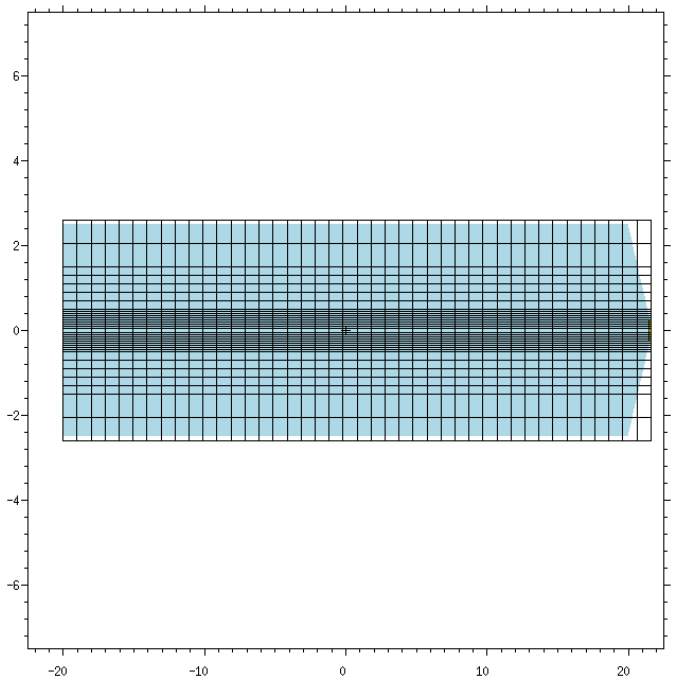

Figure 5.7. Super-imposed mesh weight windows on the simulations base-geometry.

as their FOM were much lower than the values in table 5.6. Their values were even lower than the analog calculation (calculation without any variance reduction technique).

5.3 Post-processing

The MCNP outputs have to be post-processed in order to give them a physical meaning, to opportunely normalize them, to properly calculate their uncertainties and to plot and compare them.
In the framework of this thesis a MATLAB code is implemented. It is capable of post-processing in the same run whatever number of different results, running with whatever tally configuration (different tally types, different distances from the source, different tally dimensions, different energy binning, ...). After the post-processing ends, the code let the user choose how many comparison desired between the computed results. For each comparison a list of the processed results is shown and the user can select which ones to compare. Finally the code can save on Excel files the post-processed results. The Excel file is set to be read by the Labview elaboration program for being compared with the experimental spectra. The complete code is reported in appendix A.
Since the spectrum yield results are given per unit computed-particle, they have to

be multiplied for the source intensity to be physically meaningful. As mentioned above, the source intensity is $2.58 \times 10^9\,\mu C^{-1}$. Then, data have to be normalized in energy by dividing each yield for the energy interval of its bin. Results are now expressed in $\mu C^{-1} MeV^{-1} cm^{-2}$. By multiplying for the tally area and dividing by the solid angle to consider also the distance between the tally and the source, we get eventually the most proper unit for studying them and doing comparisons between results with different moderator thickness and between simulations and experiments: $\mu C^{-1} MeV^{-1} sr^{-1}$.
The last part of the post-processing is dedicated to the uncertainty analysis. From the Central Limit Theorem we know that simulations results have the probability of 68% of actually being within the interval $\mu \pm \sigma_s$, the 95% of being within $\mu \pm 2\sigma_s$ and the 99% of being within $\mu \pm 3\sigma_s$, where μ is the yield value and σ_s its statistical standard deviation, the one provided by MCNP. It was chosen to consider $2\sigma_s$ as intrinsic calculation uncertainty and to perform a Taylor propagation analysis [35] considering all other error sources in the normalization such as the solid angle estimation. It is important to state that it was not taken into account any error due to MCNP6 cross-section tables or brought by the neutron source used. The errors of the simulations carried out are therefore imputable to the calculation statistics and to the normalization quantities.

Chapter 6

Results and Discussion

This chapter discusses results of the experimental campaign and the comparison with those of Monte Carlo simulations. Material and methods adopted are described in detail in previous chapters.

6.1 Experimental results

An extensive experimental campaign was carried out at Legnaro National Labs of INFN by irradiating a thick beryllium target with 5 MeV protons accelerated via a CN Van De Graaff accelerator. Neutron fluence energy spectra and the related integrals were derived at different moderator thicknesses in order to characterization the actual moderating property of the AlF_3.

6.1.1 Neutron energy spectra

The measurement were performed through the innovative and improved spectrometer *ACSpect*. This compact and easy-of-use system demonstrated to be able of reconstructing neutron spectra similar to those obtained with complex and bulky *time of flight* systems [21]. The system was irradiated at three configurations, i.e. without moderator and with moderator layers 1.15 cm and 2.16 cm in thickness. Spectra were collected adopting the following variable binning structure:

- $dE_{bin} = 70$ keV from zero to 280 keV
- $dE_{bin} = 60$ keV from 280 keV to 400 keV
- $dE_{bin} = 40$ keV from 400 keV to 3.2 MeV

Experimental results are shown in figures 6.1, 6.2 and 6.3, where neutron spectra collected at 0, 1.15 and 2.16 cm of moderator thicknesses are reported. Uncertainties were calculated as explained in section 3.3. In particular, an error value of

0.1 µC was assumed for the integrated beam charge, while an uncertainty of 1 mm was considered for the distance between the spectrometer and the beryllium target.

The spectra measured by ACSpect show a minimum detectable neutron energy

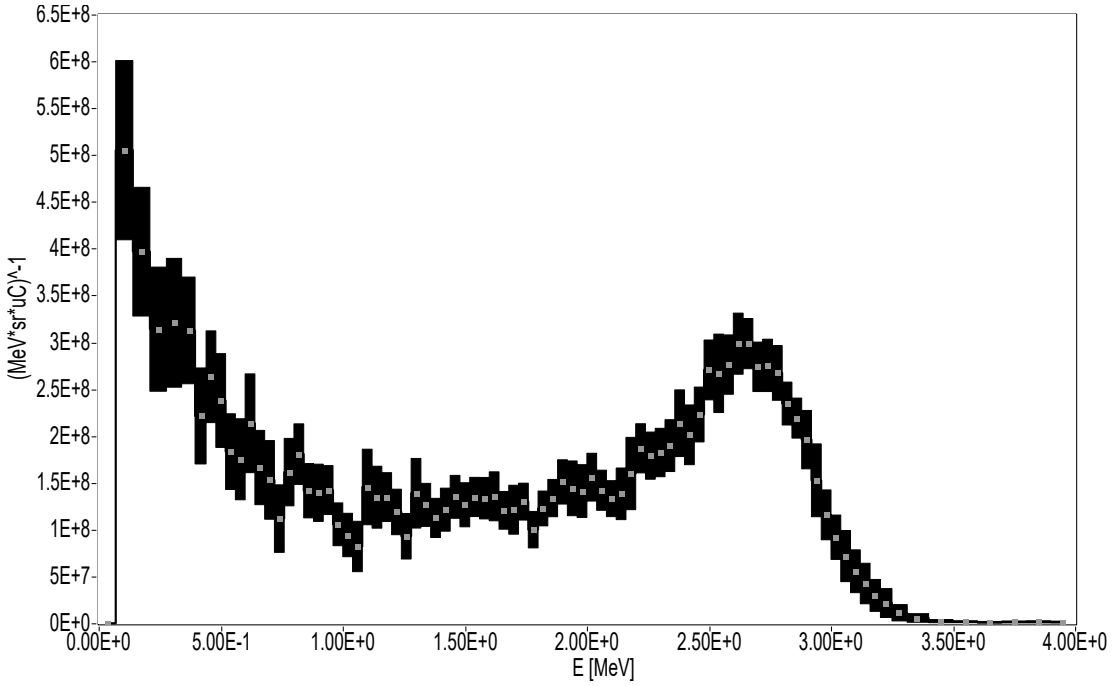

Figure 6.1. Neutron spectrum without moderator. The yield is normalized to the unit $MeV^{-1}\mu C^{-1}sr^{-1}$. The mean uncertainty averaged over all the energy bins is about 20%.

of about 100 keV. Anyway, as already discussed in chapter 3, for energy below 200/250 keV data have to be taken with care since at these low energies:

- the system capability of discriminating between recoil protons and secondary electrons due to gammas could be not effective,
- any non-idealities of the different stages of the spectrometer, in particular the scintillator interface, could affect the assessment of the proton energy,
- the actual irradiation geometry and air and room scattering components could modify the spectrum profile measured.

It should be finally underlined that below 250 keV there are no literature data to compare with.

The first comparison concerns the neutron spectrum measured with *ACSpect* without moderator and the only two other results reported in literature for the same irradiation field, i.e. neutrons generated by 5 MeV protons impinging on a thick

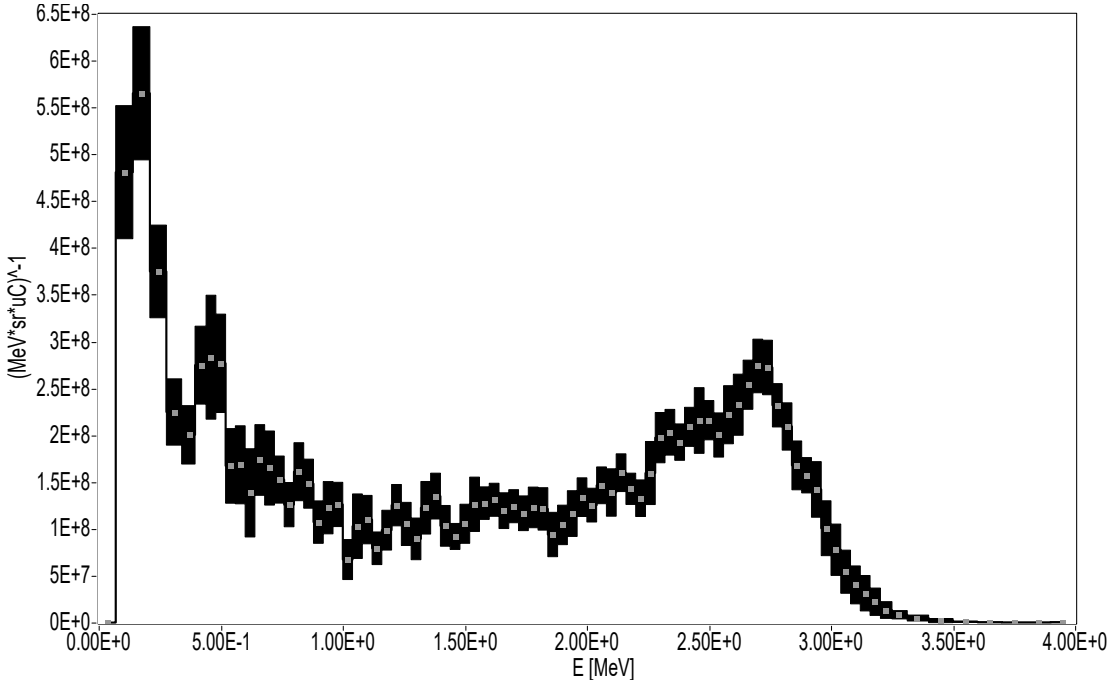

Figure 6.2. Neutron spectrum moderated with 1.15 cm of AlF_3. The yield is normalized to the unit $MeV^{-1}\mu C^{-1}sr^{-1}$. The mean uncertainty averaged over all the energy bins is about 20%.

beryllium target. Literature data refer to spectrometry performed by Howard et al. [21] by means of a *time of flight* system and by Agosteo et al. [7] by means of the first version of the *ACSpect*. Figure 6.4 shows the comparison.

It should be underlined that, due to beam source instability and the related current limitations during the experimental campaign, it were not possible to have counting statistics lower than about 10% for the *ACSpect*. Despite that, as shown by figure 6.4, spectra agree fairly well. In particular the spectrum measured by *ACSpect* resulted to be higher than the ones from literature of about 20% probably due to a systematic error in the source-detector distance.

As described in previous chapters, Monte Carlo simulations based on MCNP6 code were performed to have a numerical basis for the understanding of the neutron spectrum modulation in the AlF_3 moderator at study. Simulations assumed as the neutron source the spectrum measured by Agosteo et al. [7] and focus on the evolution of this starting energy distribution within the moderator. Therefore, numerical results do not consider and do not reproduce any other field components present in the experimental energy distributions. The actual spectrum results on even lower energy region than the critical one but those account for the effects of the moderator on the source-limited-energy-range only. In order to compare numerical and experimental results, both experimental and calculated spectra were

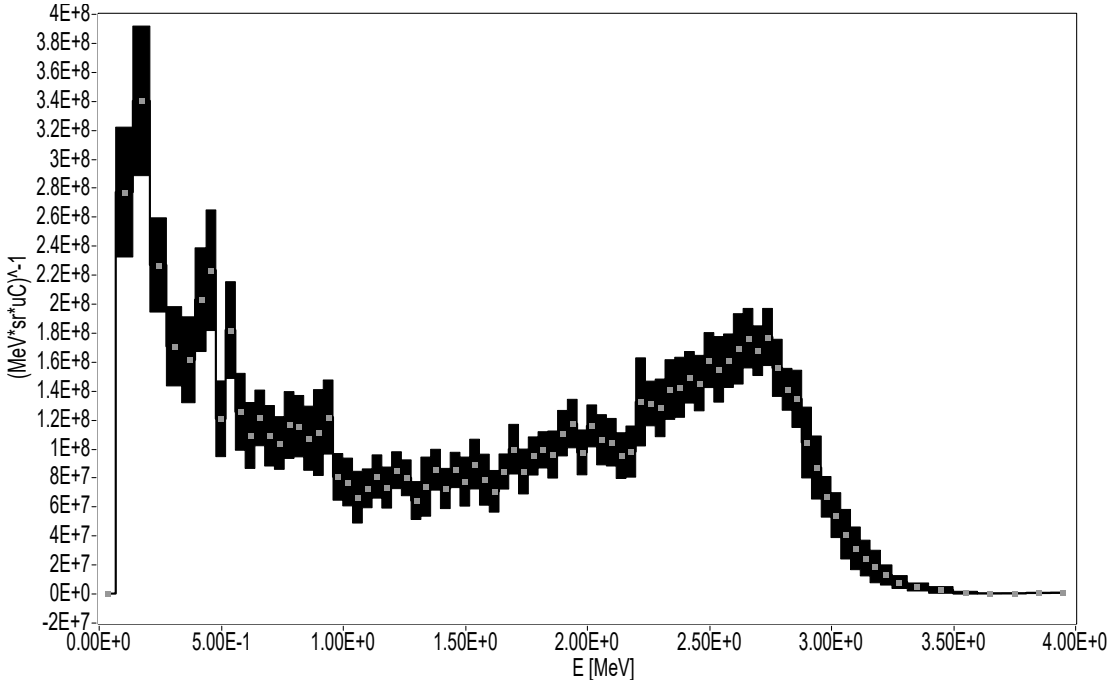

Figure 6.3. Neutron spectrum moderated with 2.16 cm of AlF_3. The yield is normalized to the unit $MeV^{-1}\mu C^{-1}sr^{-1}$. The mean uncertainty averaged over all the energy bins is about 19%.

cut at a threshold energy of about 298 keV. As a test of the correct implementation of the neutron source, simulations were firstly compared with experimental results obtained through the *ACSpect* in the configuration set-up without any moderator layer. Figure 6.5 shows the good agreement between the numerical and the experimental results. Given that, a direct comparison between experimental neutron spectra and numerical distributions derived with an AlF_3 layer 1.15 cm and 2.16 cm (6.8) in thickness were carried out. Results are shown in figures 6.6 and 6.7.

The overall comparison between numerical and experimental spectra shows a good agreement between results, with an increasing matching at 1.15 cm and 2.16 cm of AlF_3. This demonstrates the good agreement between the moderator numerical model and the actual moderator composition and density. Figure 6.9 shows a comparison between the three experimental spectra we measured.

6.1.2 Neutron integral fluence

From spectra shown in figures 6.5, 6.6 and 6.7 the total fluence can be calculated by integrating distributions over the energy range 245 keV-3.2 MeV. In order to improve the amount of information useful to perform the best assessment of the

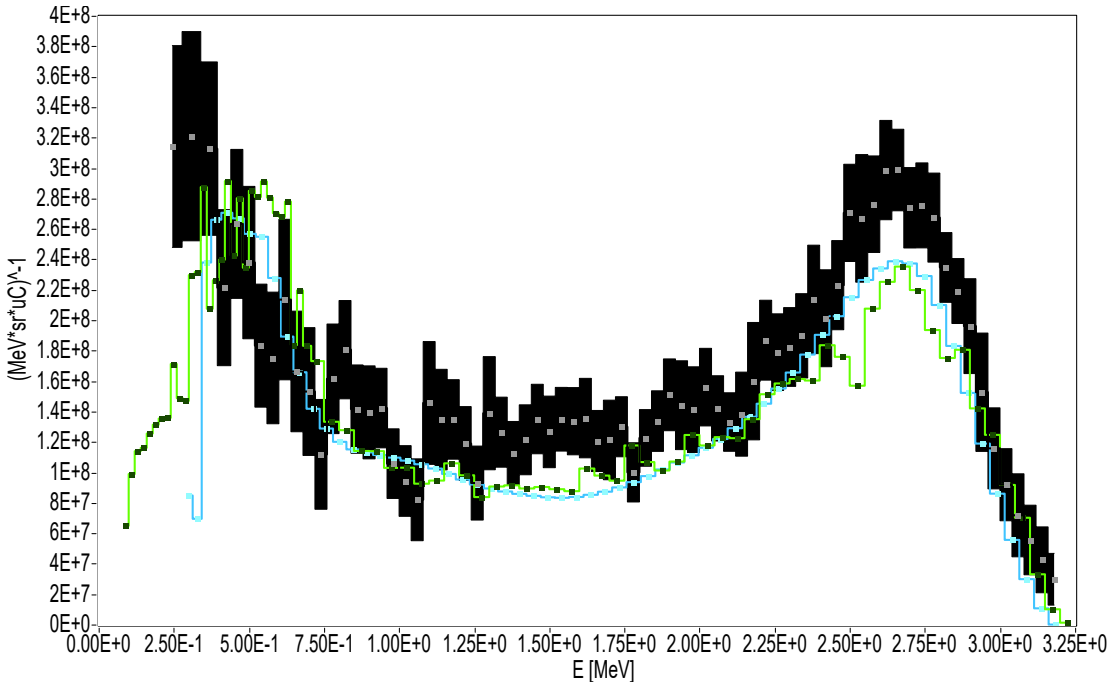

Figure 6.4. Comparison between the neutron spectrum (without moderator) measured with the *ACSpect*, black spectrum, measured by Howard et al. [21], green spectrum, and measured by Agosteo et al. [7], light-blue spectrum. The yield is normalized to the unit $\mathrm{MeV}^{-1}\mu\mathrm{C}^{-1}\mathrm{sr}^{-1}$.

moderation properties of the AlF_3, a second set of measurements were performed with the fast and reliable low resolution neutron spectrometer *DIAMON*, recently developed by Raylab, a spin-off company of Politecnico di Milano. Therefore, this calibrated device can provide a reliable integral information to be used as a reference term for the characterization.
Figure 6.10 shows spectra derived by the *DIAMON* spectrometer without moderator and with 2.16, 4.47, and 6.63 cm in thickness of AlF_3, respectively. Spectra refer to the direct component of the neutron fields derived by adopting the ISO shadow cone method for the removal of the scattered components. Table 6.1 reports the integral fluences derived through the two different detection systems, *DIAMON* and *ACSpect*, together with those obtained numerically by performing simulations at the positions where the systems were actually located, i.e. at 130 cm for *DIAMON* and at 3.6 cm for *ACSpect*. As it can be observed, all results are in good agreement and integral values resulted to be within the uncertainties at each position and with every AlF_3 moderator thickness.
Figure 6.11 graphs integral fluences as a function of the AlF_3 moderator thickness. Values can be fitted with an exponential function to assess the macroscopic reaction

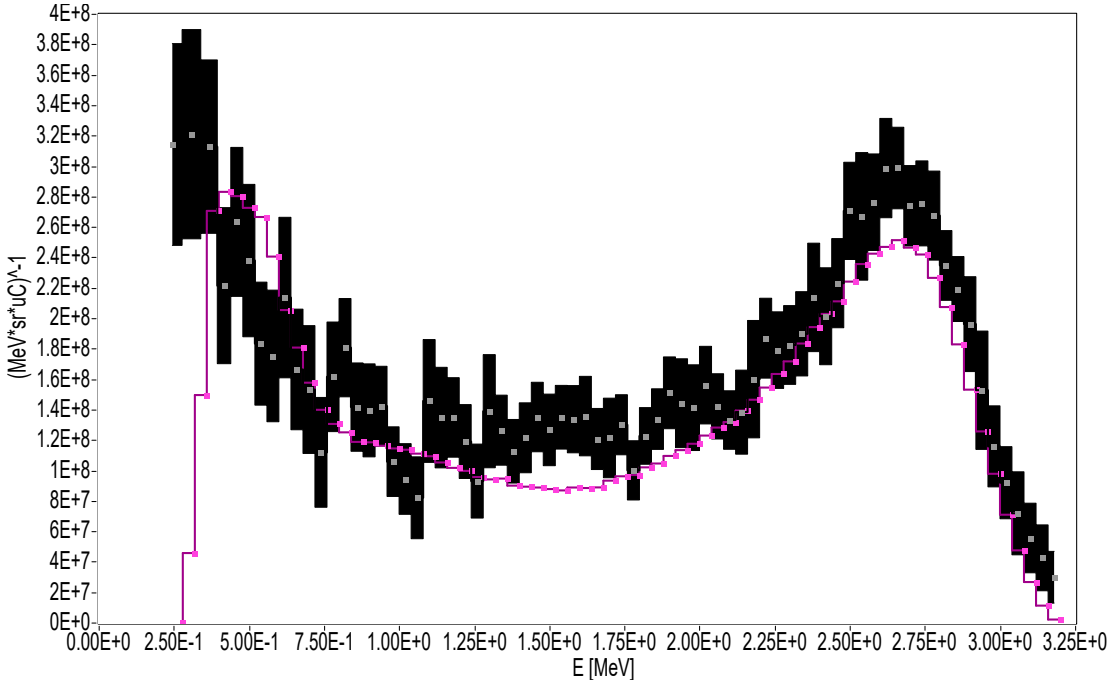

Figure 6.5. Comparison between experimental, black spectrum, and Monte Carlo simulation results, purple spectrum, obtained without any moderator. Neutron yields are normalized to the unit $\mathrm{MeV}^{-1}\mu\mathrm{C}^{-1}\mathrm{sr}^{-1}$.

Integral fluence $[10^8\ \mu\mathrm{C}^{-1}\mathrm{sr}^{-1}]$				
AlF_3	DIAMON		ACSpect	
thickness [cm]	Experiments	Simulations	Experiments	Simulations
0	3.93 ± 0.16	4.19 ± 0.23	5.11 ± 0.94	4.19 ± 0.23
1.15			4.37 ± 0.76	3.83 ± 0.21
2.16	2.73 ± 0.11	3.18 ± 0.11	3.39 ± 0.58	3.35 ± 0.18
4.47	1.66 ± 0.07	1.87 ± 0.07		
6.63	1.15 ± 0.05	1.10 ± 0.04		

Table 6.1. Neutron integral fluence measured at INFN's LNL and calculated by means of Monte Carlo simulations, using different moderator thickness. DIAMON simulations are performed at 130 cm, while ACSpect simulations at 3.636 cm.

cross section corresponding to the overall attenuation of the neutron population[1].

[1]The estimated cross-section Σ is therefore related to the overall neutron fluence attenuation by the relation: $\frac{\phi_x}{\phi_0} = e^{-\Sigma x}$, where x is the path-length flown in the moderator ϕ_x is the neutron

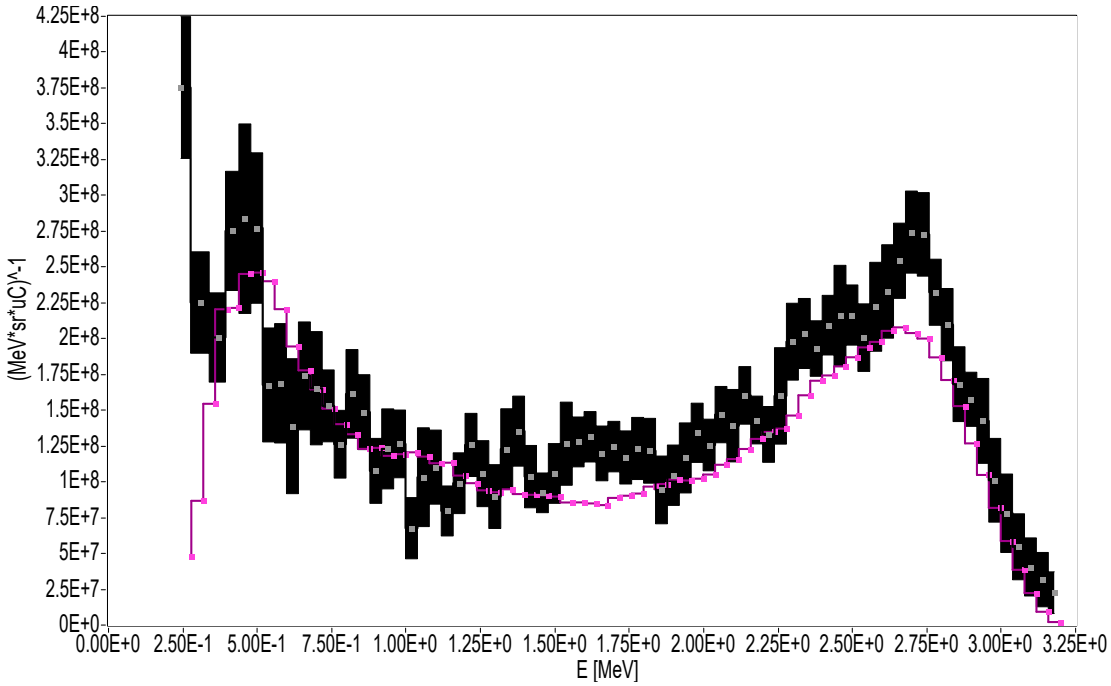

Figure 6.6. Comparison between experimental, black spectrum, and Monte Carlo simulation results, purple spectrum, obtained with a 1.15 cm of AlF_3. Neutron yields are normalized to the unit $MeV^{-1}\mu C^{-1}sr^{-1}$.

This information is important to determine the effectiveness of the AlF_3 moderator at study. Results are reported in table 6.2, which highlights a good agreement between experimental and simulation results.

	Macroscopic cross-section [cm^{-1}]
DIAMON	0.186
ACSpect	0.178
Simulations	0.19

Table 6.2. Neutron macroscopic cross-section of AlF_3 in the energy range from about 250 keV to 3.2 MeV.

flux after a certain thickness x of the moderator and ϕ_0 is the neutron flux without moderator.

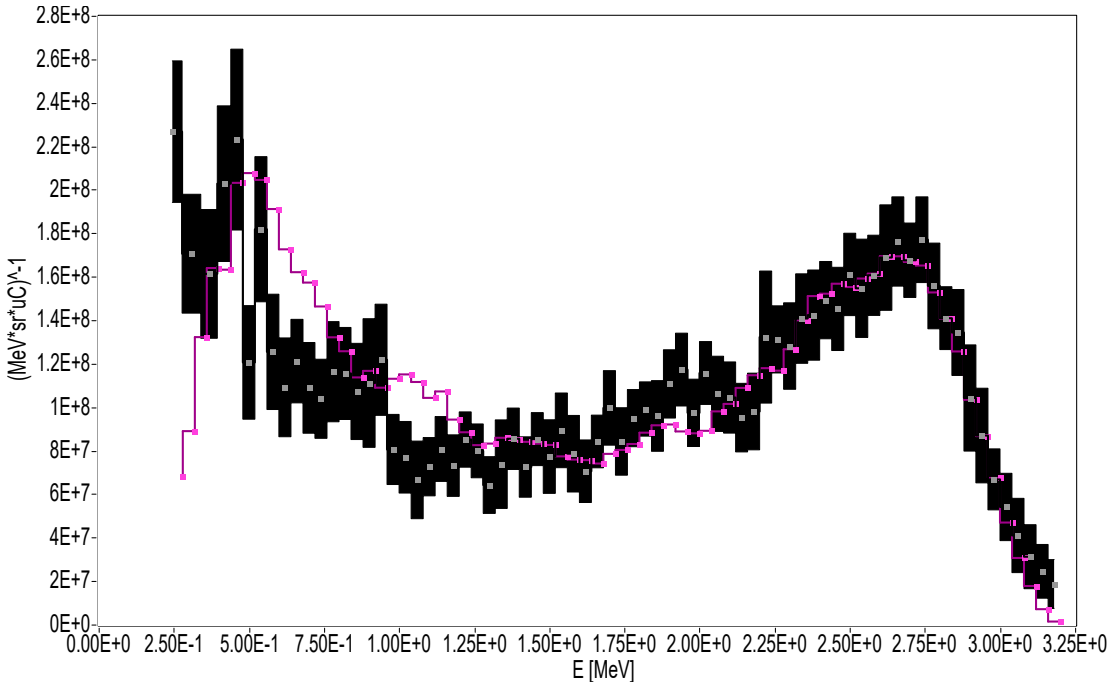

Figure 6.7. Comparison between experimental, black spectrum, and Monte Carlo simulation results, purple spectrum, derived with 2.16 cm of AlF_3. Neutron yields are normalized to the unit $MeV^{-1}\mu C^{-1}sr^{-1}$.

6.2 Thicker layer of AlF_3, simulations results

Since the Monte Carlo simulations gave good results, the neutron spectra of the simulations performed using increasing thicknesses of AlF_3 are hereby shown. Figure 6.13 shows the spectra in a linear scale in order to appreciate their profile change. Since the attenuation brings strongly down neutron yields, only three increasing thicknesses per graph are plotted. In each further graph the thinner layer of moderator is the thicker one of the previous graph in order to have a reference for the yield. To better appreciate the yield attenuation instead, the same spectra are plotted using a logarithmic scale and are shown in figure 6.14. We can see that the spectra is shifted toward the epithermal region as it is expected and wanted. Finally we remind that the spectra presented in this section are calculated using a source which energy does not get down 298 kev. The energy region below 298 keV is therefore accounting for the effects of the moderator on the source-limited-energy-range only.

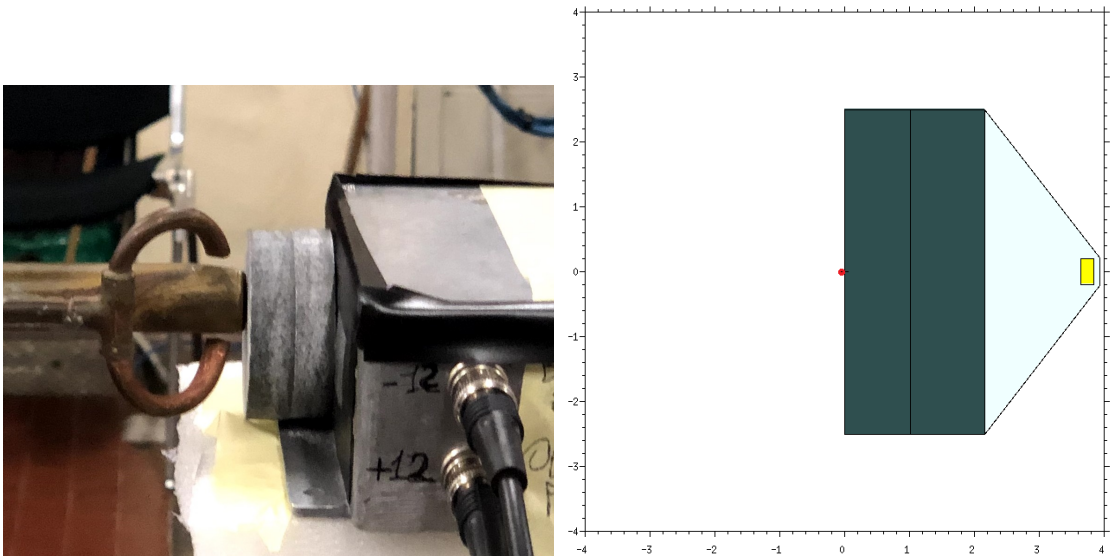

(a) (b)

Figure 6.8. Parallelism between the experimental set-up (a) and the simulation geometry (b)

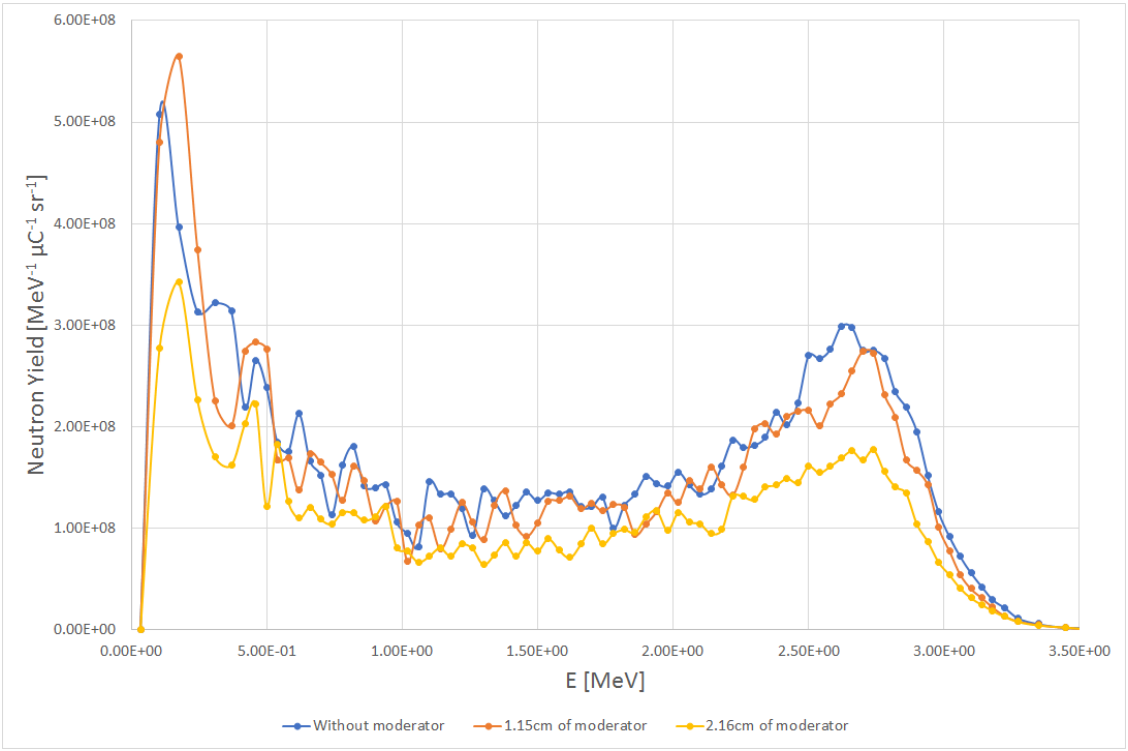

Figure 6.9. Neutron spectra measured with the *ACSpect* at the CN accelerator of INFN's LNL

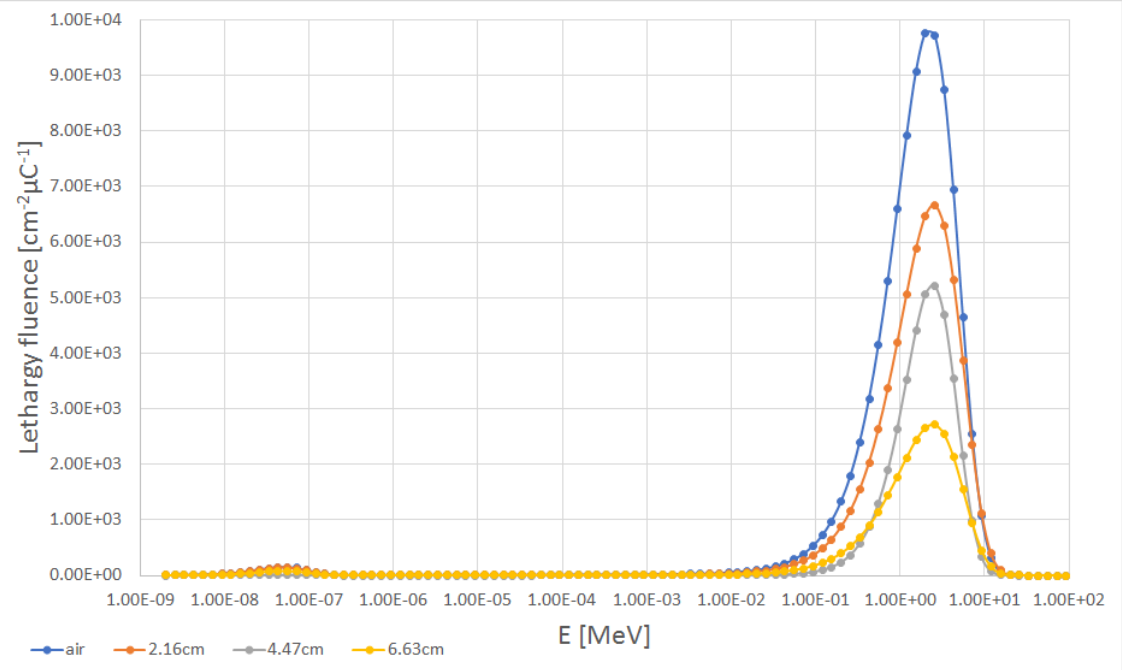

Figure 6.10. Neutron spectra measured by *DIAMON* without AlF_3, blue spectrum; with 2.16 cm, orange spectrum; with 4.47 cm, grey spectrum; with 6.63 cm, yellow spectrum. All measurements are performed at 130 cm from the beryllium target. Neutron yields is in lethargy fluence [$\mu C^{-1} cm^{-2}$].

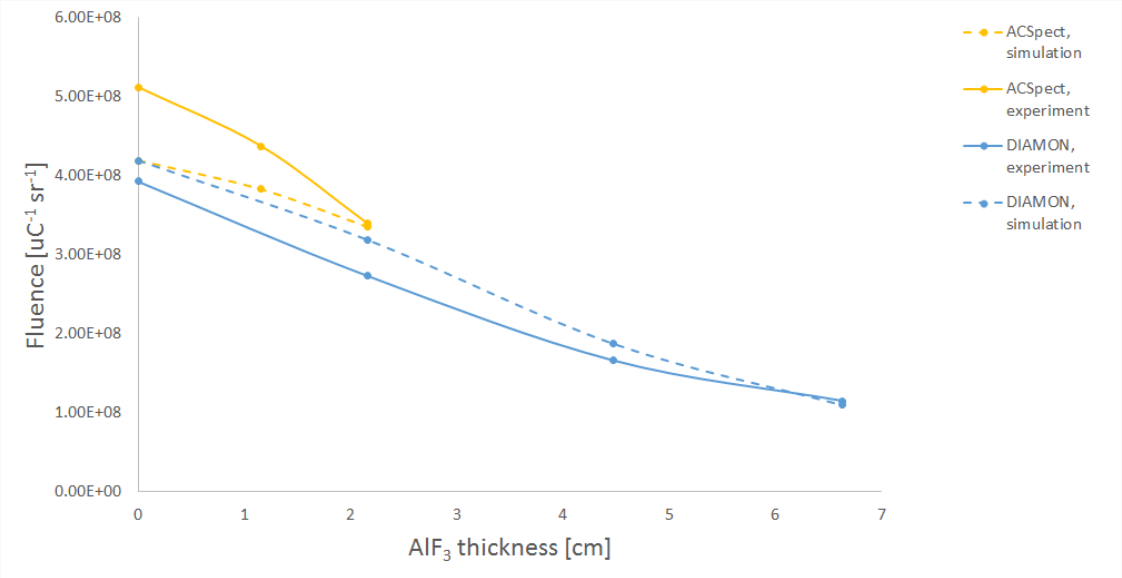

Figure 6.11. Neutron integral fluence measured at INFN's LNL with DIAMON and ACSpect spectrometers and calculated by means of Monte Carlo simulations for both the experimental set-ups, plotted versus the thickness of moderator used.

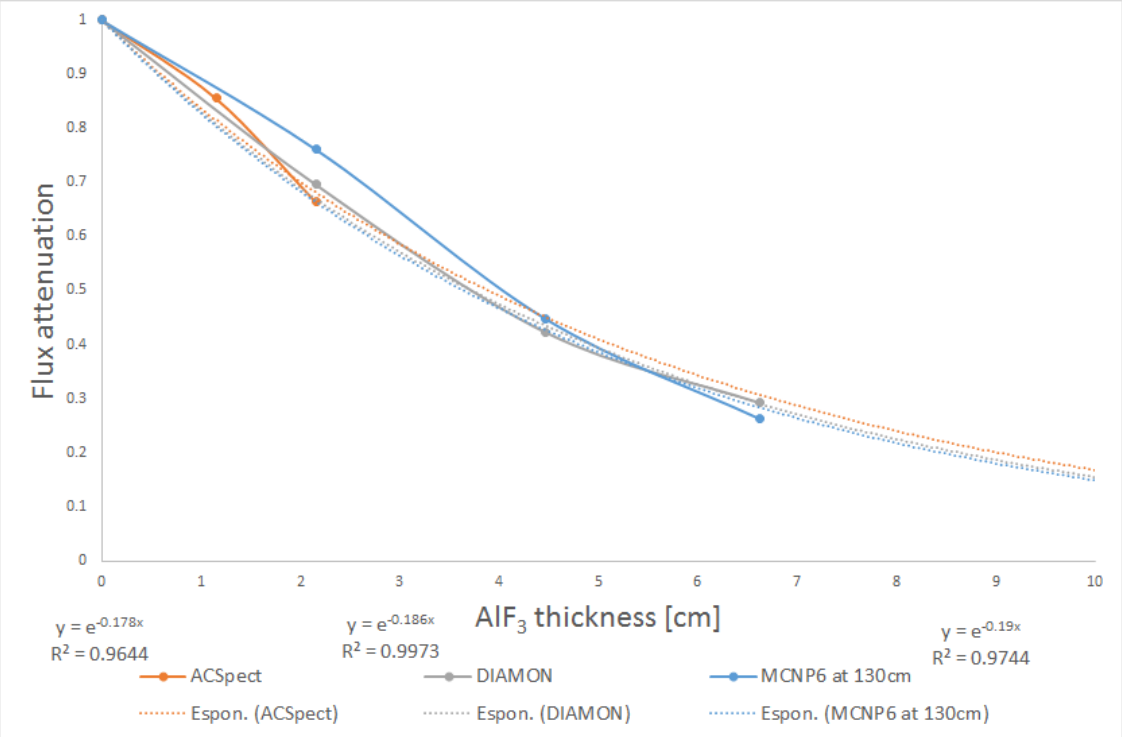

Figure 6.12. Fluence attenuation plotted versus the thickness of AlF_3 used. The three plots are the experimental results of the *ACSpect*, orange curve, the experimental results of the *DIAMON*, grey curve, and the Monte Carlo simulations results, blue curve. Dashed curves are the respectively exponential fits and the related equations are written on the legend together with the square of the fit-residuals.

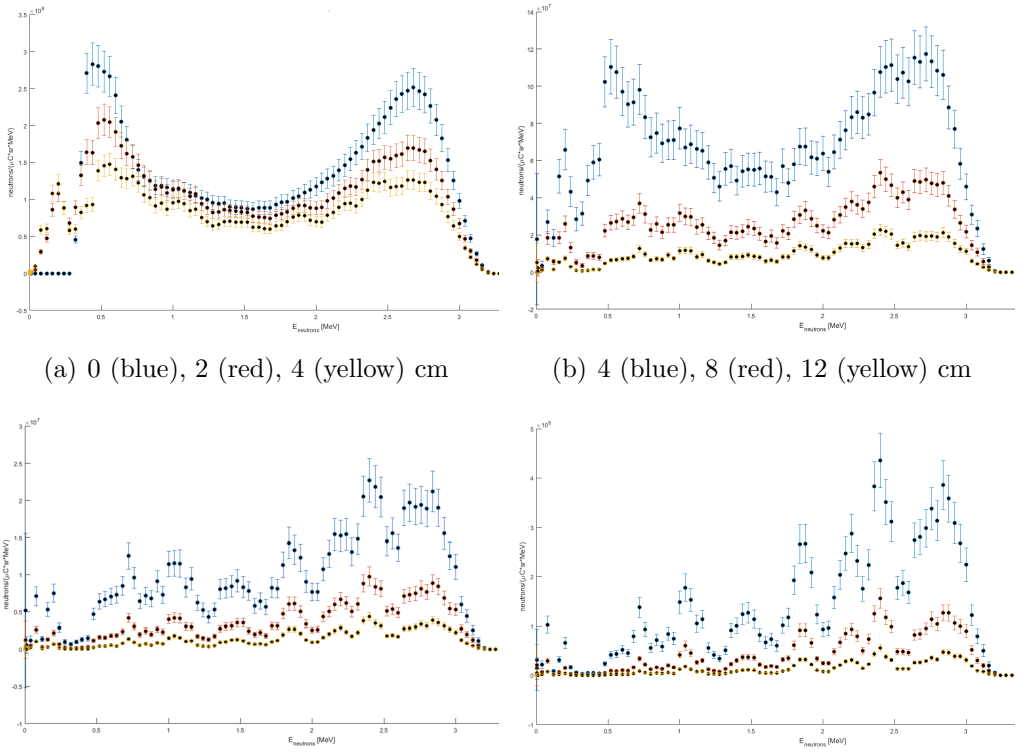

(a) 0 (blue), 2 (red), 4 (yellow) cm

(b) 4 (blue), 8 (red), 12 (yellow) cm

(c) 12 (blue), 16 (red), 20 (yellow) cm

(d) 20 (blue), 25 (red), 30 (yellow) cm

Figure 6.13. Neutron spectra calculated by means of Monte Carlo simulations, using several AlF_3 thicknesses up to 30 cm.

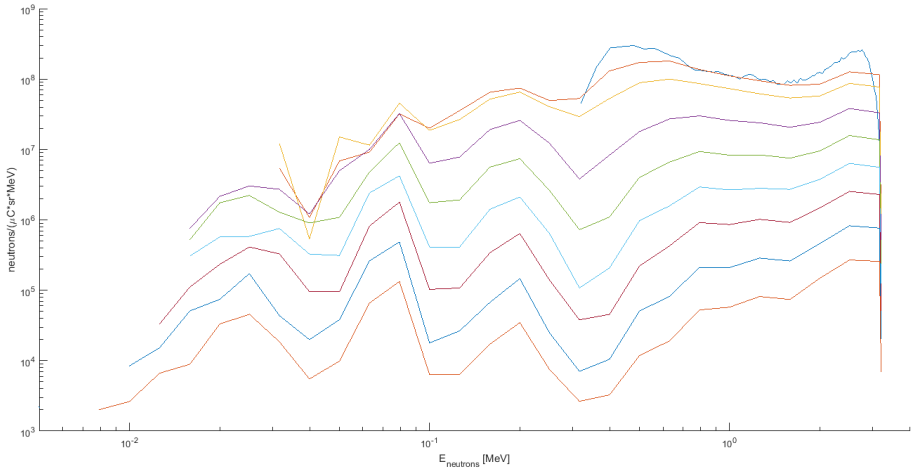

Figure 6.14. Neutron spectra calculated by means of Monte Carlo simulations. Several thicknesses of AlF_3 are used as indicated in the plot legend. The scoring tally is kept fixed at 40 cm from the source. The axis are represented in logarithmic scale.

Chapter 7

Conclusions

Experiments and Monte Carlo simulations were carried out to characterize the moderation properties of densified aluminum tri-fluoride AlF_3 mixed with lithium (LiF) on a neutron beam for accelerator-based Boron Neutron Capture Therapy (BNCT). The neutron beam for accelerator-based BNCT is provided through either ^{7}Li(p,n), ^{9}Be(p,n) or ^{9}Be(p,n) nuclear reactions induced by high energies proton or deuterium beams on a beryllium or lithium target. The clinical beam desired for BNCT has energy in the epithermal range. Since neutrons produced by those reactions have high energies, they need to be thermalized in order to be used for BNCT treatments. A proper Beam Shaping Assembly is therefore needed. The design of the BNCT beam obtained with the RFQ accelerator built by INFN, comprises a BSA which bulk is made of AlF_3. AlF_3 was indeed found to be the best among the other material tested to obtain an epithermal beam for deep seated tumors. The densified material was produced in Pavia through an innovative sintering process, however, no in-beam measurements were ever carried out before this work.
Monte Carlo simulations were performed using the *MCNP6* Monte Carlo radiation transport code, which is considered the gold standard among the Monte Carlo codes concerning coupled neutron-photon-electron transport.
Experiments were carried out at the CN accelerator facility at the LNL of INFN. The neutron beam was obtained by a 5 MeV proton beam on a beryllium target through the nuclear reaction ^{9}Be(p,n)^{9}B. The beam has the same spectral characteristic as the one generated at the RFQ accelerator facility, but with much lower flux. Measurements were performed using two neutron spectrometers:

1. the *DIAMON*, designed by Raylab to perform fast and reliable low resolution neutron spectrometry from thermal to high energies [1];

2. the *ACSpect*, an innovative active neutron spectrometer capable of measuring high resolution spectrometry from about 250 keV to about 4 MeV.

The ACSpect is based on a triple stage detection structure in which a plastic scintillator acts as an active neutron converter. Recoil-protons, generated in the scintillator via elastic scattering, are detected by a silicon telescope located at a proper distance far from the scintillator. This compact and easy-to-use system demonstrated to be able of reconstructing neutron spectra similar to those obtained with complex and bulky *time of flight* systems [21]. A notable characteristic is that it relies on a very simple response function (it does not need any unfolding technique) to determine the neutron spectrum. The ACSpect was first implemented by the Nuclear Measurements group of the Energy department of Politecnico di Milano [8] and later improved [6]. In this thesis, a further improvement was implemented by changing its technological configuration and the whole elaboration process: the spectrometer is now more compact, thus very easily transportable, and much less sensible to external noise.
Neutron spectra were measured by means of the ACSpect without any moderator, with 1.15 cm and with 2.16 cm-thick AlF_3 bricks and compared to the Monte Carlo model for its validation. From the spectra, the integral neutron fluence is calculated and compared with the more reliable integral fluence measured by means of the DIAMON. This detector was used to measure the neutron fluence without any moderator and with 2.16 cm, 4.47 cm and 6.63 cm-thick AlF_3 bricks. Considering the integral neutron fluence obtained with different moderator thickness, the AlF_3 macroscopic cross section corresponding to the overall attenuation of the neutron population is derived.
The measurements are the first experimental neutron spectra obtained with densified AlF_3 with LiF as moderator and do give a first validation of the Monte Carlo calculations involving aluminium tri-fluoride, considering that the experimental results are in good agreement with simulations for either integral fluence and energy spectra.

Bibliography

[1] URL: https://www.raylab.solutions.

[2] URL: http://www.hamamatsu.com/eu/en/product/category/3100/3003/3044/H10720-110/index.html.

[3] URL: http://www.hamamatsu.com/eu/en/product/category/3100/3001/R9880U-110/index.html.

[4] S. Agosteo et al. "A feasibility study of a solid-state microdosimeter". In: *Applied Radiation and Isotopes* 63 (2005), pp. 529–535.

[5] S. Agosteo et al. "Characterisation of an accelerator-based neutron source for BNCT versus beam energy". In: *Nuclear Instruments and Methods in Physics Research A* 476 (2002), pp. 106–112.

[6] Stefano Agosteo et al. "A telescope detection system for direct and high resolution spectrometry of intense neutron fields". In: *Radiation Measurements* 85 (2016), pp. 1–17.

[7] Stefano Agosteo et al. "Characterization of the energy distribution of neutrons generated by 5 MeV protons on a thick beryllium target at different emission angles". In: *Applied Radiation and Isotopes* 69 (2011), pp. 1664–1667.

[8] Stefano Agosteo et al. "Neutron spectrometry with a monolithic silicon telescope". In: *Radiation Protection Dosimetry* 126 (2007), pp. 210–217.

[9] T. Aihara et al. "BNCT for advanced or recurrent head and neck cancer". In: *Applied Radiation and Isotopes* 88 (2014), pp. 12–15.

[10] M. J. Armishaw et al. *A Transportable Neutron Spectrometer (TNS) for radiological applications*. Tech. rep. United Kingdom Atomic Energy Authority, 1986.

[11] R. F. Barth, P. Mi, and W. Yang. "Boron delivery agents for neutron capture therapy of cancer". In: *Cancer Commun* 38 (2018), p. 35.

[12] R. Bedogni et al. "First test of SP^2: a novel active neutron spectrometer condensing the functionality of Bonner spheres in a single moderator". In: *Nuclear Instruments and Methods in Physics Research A* 767 (2014), pp. 159–162.

[13] John Bettely Birks. "Scintillations from organic crystals: specific fluorescence and relative response to different radiations". In: *Proceedings of the Physical Society* A64.10 (1951).

[14] John Bettely Birks. *The theory and practice of scintillation counting*. Ed. by D. W. Fry, L. Costrell, and K. Kandiah. Pergamon, 1964.

[15] Thomas E. Booth. *A sample problem for variance reduction in MCNP*. Tech. rep. Los Alamos National Laboratory, 1985.

[16] P. D. Bradley, A. B. Rosenfeld, and M. Zaider. "Solid state microdosimetry". In: *Nuclear Instruments and Methods in Physics Research B* 184 (2001), pp. 135–157.

[17] R. L. Bramblett, R. I. Ewing, and T. W. Bonner. "A new type of neutron spectrometer". In: *Nuclear Instruments and Methods* 9 (1960), pp. 1–12.

[18] F. D. Brooks and H. Klein. "Neutron spectrometry - historical review and present status". In: *Nuclear Instruments and Methods in Physics Research A* 476 (2002), pp. 1–11.

[19] C. Ceballos et al. "Towards the final BSA modeling for the accelerator-driven BNCT facility at INFN LNL". In: *Applied Radiation and Isotopes* 69 (2011), pp. 1660–1663.

[20] M. S. Herrera et al. "Evaluation of performance of an accelerator-based BNCT facility for the treatment of different tumor targets". In: *Physica Medica* 29 (2013), pp. 436–446.

[21] W. B. Howard et al. "Measurement of the thick-target ^{9}Be (p, n) neutron energy spectra". In: *Nuclear Science Engineering* 138.2 (2001), pp. 145–160.

[22] G. F. Knoll. *Radiation detection and measurement*. Ed. by Debra Matteson. Second edition. Wiley, 1989.

[23] A. J. Kreiner et al. "Present status of accelerator-based BNCT". In: *Reports of Practical Oncology & Radiotherapy* 21 (2016), pp. 95–101.

[24] G. Locher. "Biological effects and therapeutic possibilities of neutrons". In: *Am. J. Roentgenol* 36 (1936), pp. 1–13.

[25] Michele Lorenzoli. "A novel detection system for direct and high resolution spectrometry of intense neutron fields". PhD thesis. Politecnico di Milano, 2013.

[26] *MCNP a general Monte Carlo N-Particle transport code, version 4C*. 2000.

[27] *MCNP6 user's manual*. 2013.

[28] S. Miyatake et al. "Boron Neutron Capture Therapy for malignant brain tumors". In: *Neurologia medico-chirurgica* 56 (2016), pp. 361–371.

[29] K. Nakai et al. “Boron Neutron Capture Therapy fot glioblastoma: a phase-I/II clinical trial at JRR-4”. In: *European Association of NeuroOncology Magazine* 4 (2014), pp. 116–123.

[30] Ian Postuma. “Clinical application of accelerator-based Boron Neutron Capture Therapy: optimization of procedures, tailoring of a neutron beam and evaluation of its dosimetric performance”. PhD thesis. Università di Pavia, 2015.

[31] A. B. Rosenfeld et al. “A new detector for microdosimetry applications in proton therapy”. In: *IEEE Nuclear Science Symposium and Medical Imaging Conference* 1 (1999), pp. 331–338.

[32] Saint-Gobain Crystals. *BC-404 scintillator*. URL: `http://www.crystals.saint-gobain.com/Plastic_Scintillators.aspx`.

[33] Saint-Gobain Crystals. *Plastic product brochure*. URL: `http://www.crystals.saint-gobain.com/Plastic_Scintillators.aspx`.

[34] W. A. G. Sauerwein et al. *Neutron Capture Therapy, principles and applications*. Ed. by W. A. G. Sauerwein et al. Springer, 2012.

[35] J. R. Taylor. *An introduction to error analysis: the study of uncertainties in physical measurements*. Ed. by Ann McGuire. Second. University Science Books, 1997.

[36] D. J. Thomas. “Neutron spectrometry”. In: *Radiation Measurements* 45 (2010), pp. 1178–1185.

[37] L. Torrisi. “Plastic scintillator investigations for relative dosimetry in proton-therapy”. In: *Nuclear Instruments and Methods in Physics Research B* (2000).

[38] S. Tudisco et al. “A new large area monolithic silicon telescope”. In: *Nuclear Instruments and Methods in Physics Research A* 426 (1999), pp. 436–445.

[39] Jacopo Valsecchi. “Thermal and epithermal neutron beam tailoring for BNCT research at CN proton accelerator of INFN Legnaro National Laboratories”. MA thesis. Università di Pavia, 2014.

[40] S. J. Walker. “Boron neutron capture therapy: principles and prospects”. In: *Radiography* 4 (1996), pp. 211–219.

[41] Y. Yura and Y. Fujita. “Boron neutron capture therapy as a novel modality of radiotherapy for oral cancer: principle and antitumor effect”. In: *Oral Science International* 10 (2013), pp. 9–14.

Appendix A

Monte Carlo simulations post-processing code

Listings of the Matlab code implemented for the post-processing of the Monte Carlo simulations results.

```
clear all
close all

%indications:
% Energy bin file must have the energy bin upper extremes in
% column and in MeV.
% Results must have the form of 'MCTAL' file written by MCNP but
% containing just the results informations!

source_factor=2.58e9; %1/uC
err_sf=0; % absolute error [1/uC]
%simulation results
prompt='How many results dou you want to compare? ';
nc=input(prompt);
prompt='Have they the same energy bins? [y/n]  ';
sameEb=input(prompt, 's');
Ebin=[];
if sameEb=='y'
    prompt='Name of the file in which there are the Energy bins data: ';
    fname=input(prompt, 's');
    Eb_file= fopen(fname);
    Eb_c= textscan(Eb_file, '%f');
    Eb_v= cell2mat(Eb_c);
    Ebin= repmat(Eb_v, [1,1,nc]); % MeV
```

```
end
res_name_m= repmat([' '], nc, 20);
res=[];
for i=1:nc
    prompt='write the name of the file in which there are '...
        'the results data: ';
    res_name=input(prompt, 's');
    for k=1:length(res_name)
        res_name_m(i,k)=res_name(1,k);
    end
    display 'What type of MCNP tally is it?'
    display 'ID    tally'
    display ' 1    f1'
    display ' 2    f4 and f2'
    prompt='write the tally ID number: ';
    tallyt=input(prompt);
    tarea= pi*0.2^2;
    %% general post-ptocessing
    % prompt='tally distance [cm]: ';
    % tdist=input(prompt);
    % "thicker moderator" simulations post processing
    display 'What is the distance of the simulated ACSpect?'
    display 'ID    distance'
    display ' 1    40'
    display ' 2    attached to the bsa'
    prompt='write the tally ID number: ';
    flag_dist=input(prompt);
    if flag_dist==1
        tdist=41.476;
    elseif flag_dist==2
        prompt='bsa thickness [cm]: ';
        tdist=1.476+input(prompt);
    else
        prompt='tally distance [cm]: ';
        tdist=input(prompt);
    end
    res_file(i)= fopen(res_name);
    res_c= textscan(res_file(i), '%f');
    res_v= cell2mat(res_c);
    k=1;
    res_m=[];
    for j=1:2:length(res_v)-1
```

```
    res_m(k,1)=res_v(j);    % particles/cm2/n
    res_m(k,2)=res_v(j+1); % relative error
    k=k+1;
end
if i==1 || size(res_m,1)==size(res,1)
    res(:,:,i)=res_m;
else
    if size(res_m,1)<size(res,1)
        for j=size(res_m,1)+1:size(res,1)
            res_m(j,:)=NaN;
        end
        res(:,:,i)=res_m;
    else
        for j=size(res,1)+1:size(res_m,1)
            res(j,:,:)=NaN;
        end
        res(:,:,i)=res_m;
    end
end
solid_angle=tarea/(tdist^2); %sr
err_sa= 0.1*solid_angle; % absolute error, [sr]
if sameEb=='n'
    prompt='Name of the file in which there are the'...
        'current Energy bins data: ';
    fname=input(prompt, 's');
    Eb_file= fopen(fname);
    Eb_c= textscan(Eb_file, '%f');
    Eb_v= cell2mat(Eb_c);
    if i==1 || length(Eb_v)==size(Ebin,1)
        Ebin(:,1,i)=Eb_v;
    else
        if length(Eb_v)<size(Ebin,1)
            for j=length(Eb_v)+1:size(Ebin,1)
                Eb_v(j)=NaN;
            end
            Ebin(:,1,i)=Eb_v;
        else
            for j=size(Ebin,1)+1:length(Eb_v)
                Ebin(j,:,:)=NaN;
            end
            Ebin(:,1,i)=Eb_v;
        end
```

```
    end
end
% controllo che bin e risultati abbiano le stesse dimensioni,
% altrimenti display a message error
if size(res_m,1)~=size(Eb_v,1)
    display 'ERRORE!! Il vettore del seguente risultato non ha'...
        'la stessa lunghezza del suo bin!'
    display ([res_name ''])
end
% normalizzo per micro-Coulomb di protoni sparati dall'acceleratore
% sul target di Berillio e per unita' di angolo solido
f_norm= @(r,a,b) r.*a/b;
un_res(:,1)=res(:,1,i);
% gli errori sono considerando 2*standard_deviation.
err_un(:,1)=2*res(:,2,i).*res(:,1,i);
if tallyt==1
    res(:,1,i)=res(:,1,i)*source_factor/solid_angle; %n/(uC*sr)
    % error propagation
    e_sf_p=abs(f_norm(un_res, source_factor+err_sf, solid_angle)...
        -res(:,1,i));
    e_sf_m=abs(f_norm(un_res, source_factor-err_sf, solid_angle)...
        -res(:,1,i));
    e_sa_p=abs(f_norm(un_res, source_factor, solid_angle+err_sa)...
        -res(:,1,i));
    e_sa_m=abs(f_norm(un_res, source_factor, solid_angle-err_sa)...
        -res(:,1,i));
    e_un_p=abs(f_norm(un_res+err_un, source_factor, solid_angle)...
        -res(:,1,i));
    e_un_m=abs(f_norm(un_res-err_un, source_factor, solid_angle)...
        -res(:,1,i));
    e_sf=(e_sf_p+e_sf_m)/2;
    e_sa=(e_sa_p+e_sa_m)/2;
    e_un=(e_un_p+e_un_m)/2;
    % relative error
    res(:,2,i)=((e_sf.^2+e_sa.^2+e_un.^2).^(0.5))./res(:,1,i);
elseif tallyt==2
    res(:,1,i)=res(:,1,i)*source_factor*tarea/solid_angle; % n/(uC*s
    % error propagation
    e_sf_p=abs(tarea*f_norm(un_res, source_factor+err_sf, ...
        solid_angle)-res(:,1,i));
    e_sf_m=abs(tarea*f_norm(un_res, source_factor-err_sf, ...
        solid_angle)-res(:,1,i));
```

```
        e_sa_p=abs(tarea*f_norm(un_res, source_factor, ...
            solid_angle+err_sa)-res(:,1,i));
        e_sa_m=abs(tarea*f_norm(un_res, source_factor, ...
            solid_angle-err_sa)-res(:,1,i));
        e_un_p=abs(tarea*f_norm(un_res+err_un, source_factor, ...
            solid_angle)-res(:,1,i));
        e_un_m=abs(tarea*f_norm(un_res-err_un, source_factor, ...
            solid_angle)-res(:,1,i));
        e_sf=(e_sf_p+e_sf_m)/2;
        e_sa=(e_sa_p+e_sa_m)/2;
        e_un=(e_un_p+e_un_m)/2;
        % relative error
        res(:,2,i)=((e_sf.^2+e_sa.^2+e_un.^2).^(0.5))./res(:,1,i);
    end
    % mean error between Ebins of each simulation considered
    mean_rel_err(i)=nansum(res(:,2,i))/size(res,1);
    i_flux(i)=sum(res(:,1,i)); % 1/(uC*sr)
    flag_cut_start=find(Ebin(:,1,i)<=0.298, 1,'last');
    flag_cut_end=find(Ebin(:,1,i)>=3.2, 1, 'first');
    i_flux_cut(i)=0; % 1/(uC*sr)
    for j=flag_cut_start:flag_cut_end
        i_flux_cut(i)=i_flux_cut(i)+res(j,1,i); % 1/(uC*sr)
    end
    clear e_* err_un un_res
end
fclose('all');
% normalizzo per l'energia del bin
Ebin_width=[];
for i=1:size(Ebin,3)
    for j=1:size(Ebin,1)
        if j==1
            Ebin_width(j,1,i)=Ebin(j,1,i);
        else
            Ebin_width(j,1,i)=Ebin(j,1,i)-Ebin(j-1,1,i);
        end
    end
end
res(:,1,:)=res(:,1,:)./Ebin_width(:,1,:); % particles/(uC*sr*MeV)



% Grafici
```

```
% grafico ogni tally singolarmente
for i=1:nc
    xx=Ebin(:,1,i);
    yy=res(:,1,i);
    ee=res(:,2,i).*res(:,1,i);
    figure
    hold on
    plot(xx,yy,'ok', 'MarkerFaceColor', 'k')
    errorbar(xx,yy,ee, 'k')
    title (res_name_m(i,:))
    xlabel 'E_{neutrons} [MeV]'
    ylabel 'neutrons/(\muC*sr*MeV)'
end

% grafico il comparison globale
figure
hold on
title 'Comparison of all results asked'
xlabel 'E_{neutrons} [MeV]'
ylabel 'neutrons/(\muC*sr*MeV)'
LL=[];
for i=1:nc
    xx=Ebin(:,1,i);
    yy=res(:,1,i);
%     ee=res(:,2,i).*res(:,1,i);
%     GR(i)=errorbar(xx,yy,ee,'o', 'MarkerFaceColor', 'k');
    GR(i)=plot(xx,yy,'-');
    LL=[LL; replace(res_name_m(i,:),'_',' ')];
end
legend(GR,LL)

%eventuali comparisons tra specifici risultati
prompt='Would you like some comparisons between specific results? [y/n]
';
more_comp=input(prompt, 's');
if more_comp== 'y'
    prompt='How many specific comparisons dou you want? ';
    n_more_comp=input(prompt);
    for i=1:n_more_comp
        display 'Write the ID numbers of the results you want to compare
        display 'ID    file_name'
```

```
for j=1:nc
    IDres= num2str(j);
    display ([IDres '      ' res_name_m(j,:)])
end
display 'IDs to compare ("enter" after each one and 0 to end: '
flag=1;
j=1;
IDcomp=[];
while flag==1
    IDcomp(j)= input('');
    if IDcomp(j)==0
        flag=0;
    else
        j=j+1;
    end
end
figure
hold on
title 'specific results comparison'
xlabel 'E_{neutrons} [MeV]'
ylabel 'neutrons/(\muC*sr*MeV)'
LL=[];
for j=1:length(IDcomp)-1
    xx=Ebin(:,1,IDcomp(j));
    yy=res(:,1,IDcomp(j));
    ee=res(:,2,IDcomp(j)).*res(:,1,IDcomp(j));
    errorbar(xx,yy,ee,'o', 'MarkerFaceColor', 'k')
    LL=[LL; replace(res_name_m(IDcomp(j),:),'_',' ')];
end
legend(LL)
hold off
figure
hold on
title 'specific results comparison'
xlabel 'E_{neutrons} [MeV]'
ylabel 'neutrons/(\muC*sr*MeV)'
LL=[];
for j=1:length(IDcomp)-1
    xx=Ebin(:,1,IDcomp(j));
    yy=res(:,1,IDcomp(j));
    ee=res(:,2,IDcomp(j)).*res(:,1,IDcomp(j));
    plot(xx,yy)
```

```
            LL=[LL; replace(res_name_m(IDcomp(j),:),'_',' ')];
        end
        legend(LL)
        hold off
    end
end

prompt='Would you like to save some of the spectra?? [y/n]
';
save_spectra=input(prompt, 's');
if save_spectra=='y'
    display 'Write the ID numbers of the spectra you want to save:'
    display 'ID    file_name'
    for j=1:nc
        IDres= num2str(j);
        display ([IDres '     ' res_name_m(j,:)])
    end
    display 'IDs to save ("enter" after each one and 0 to end: '
    flag=1;
    j=1;
    IDsave=[];
    while flag==1
        IDsave(j)=input('');
        if IDsave(j)==0
            flag=0;
        else
            j=j+1;
        end
    end
    for j=1:length(IDsave)-1
        xlswrite([res_name_m(IDsave(j),:) '.xlsx'], ...
            Ebin(:,1,IDsave(j))*1e+6, 'E_bins (eV)','A1');
        xlswrite([res_name_m(IDsave(j),:) '.xlsx'], ...
            res(:,1,IDsave(j)), 'Yield ((MeV uC sr)^-1)', 'A1');
    end
end
```

Appendix B

MCNP6 input files

Listings of some parts of the MCNP6 input files implemented:

1. geometry specification code is presented together with the materials and tally specification and the specification of the importance of each gemoetry cell for the variance reduction technique;
2. neutron source code;
3. energy bins used.

B.1 Geometry, materials, tally and variance reduction

Listings of the geometry, materials and tally specification and variance reduction implementation are reported for the simulation of the ACSpect measurements at INFN's Legnaro National Laboratories, with 2.16 cm of AlF_3 and for the simulation carried out using 30 cm of AlF_3.

B.1.1 LNL set-up with 2.16 cm of AlF_3

```
Simulazione ACSpect set up at LNL, 2.16cm of AlF3
c ************************************************************************
c --CELLS-------------------------------------------------------------------
999 0   -11:20:10.1:10.2                          $ outside world, empty
100  1 -0.001124  11 -21 -20                      $ source region, air
201  6 -3  21 -22 -20                             $ mattonella #1, AIR
202  6 -3  22 10.3 -20                            $ mattonella #2, AIR
103  1 -0.001124  -10 #300                        $ environment, air
300  1 -0.001124  31 -32 -30                      $ converter equivalent
```

```
c ------------------------------------------------------------------------------

c --SURFACES-----------------------------------------------------------------
20 cz 2.5                                          $ bsa shape
30 cz 0.2                                          $ converter shape
10 trc 0 0 2.161  0 0 1.576  2.5  0.21            $ environment cone
11 pz -0.001                                       $ environment start
21 pz  0.001                                       $ bsa, mattonella #1 sta
22 pz  1.011                                       $ bsa, mattonella #2 sta
31 pz  3.636                                       $ converter start
32 pz  3.736                                       $ converter end
c ------------------------------------------------------------------------------

mode n p
c --MATERIALS----------------------------------------------------------------
c --Aria---------
m1 6000.70c .000125 7014.70c .6869 8016.70c .301248 18000.35c .011717
c --BSA----------
c ALF3 + 3% Lithium-7 fluoruro di alluminio litiato sinterizzato (d=3)
m6        13027.70c -30.880
          9019.70c  -66.600
          3006.60c  -0.189  $ Li-6
          3007.60c  -2.331  $ Li-7

[...]

c --TALLY--------------------------------------------------------------------
f3001:n 31 30 T
fc3001 tally f1, neutron current over the converter surfaces
f3002:n 31
fc3002 tally f2, neutron flux through the converter sensitive area
f3004:n 300
fc3004 tally f4, neutron flux in the converter volume

[...]

c --Variance reduction-------------------------------------------------------
# imp:n
0
1
1.7
3.0
```

```
5.3
5.3
imp:p 0 1 4r
```

B.1.2 30 cm of AlF_3

```
30cm of AlF3, front, point source
c ************************************************************************
c --CELLS-------------------------------------------------------------------
999 0   -11:20:10.1:10.2                          $ outside world, empty
500  1 -0.001124  11 -201 -30                     $ v.r. cell 0
600  1 -0.001124  11 -201 30 -60                  $ v.r. cell 0b
100  1 -0.001124  11 -201 60 -20                  $ source region, air
501  6 -3         201 -202 -30                     $ air cell a1
601  6 -3         201 -202 30 -60                  $ air cell b1
101  6 -3         201 -202 60 -20                  $ air cell c1
502  6 -3         202 -203 -30                     $ air cell a2
602  6 -3         202 -203 30 -60                  $ air cell b2
102  6 -3         202 -203 60 -20                  $ air cell c2
503  6 -3         203 -204 -30                     $ air cell a3
603  6 -3         203 -204 30 -60                  $ air cell b3
103  6 -3         203 -204 60 -20                  $ air cell c3
504  6 -3         204 -205 -30                     $ air cell a4
604  6 -3         204 -205 30 -60                  $ air cell b4
104  6 -3         204 -205 60 -20                  $ air cell c4
505  6 -3         205 -206 -30                     $ air cell a5
605  6 -3         205 -206 30 -60                  $ air cell b5
105  6 -3         205 -206 60 -20                  $ air cell c5
506  6 -3         206 -207 -30                     $ air cell a6
606  6 -3         206 -207 30 -60                  $ air cell b6
106  6 -3         206 -207 60 -20                  $ air cell c6
507  6 -3         207 -208 -30                     $ air cell a7
607  6 -3         207 -208 30 -60                  $ air cell b7
107  6 -3         207 -208 60 -20                  $ air cell c7
508  6 -3         208 -209 -30                     $ air cell a8
608  6 -3         208 -209 30 -60                  $ air cell b8
108  6 -3         208 -209 60 -20                  $ air cell c8
509  6 -3         209 -210 -30                     $ air cell a9
609  6 -3         209 -210 30 -60                  $ air cell b9
109  6 -3         209 -210 60 -20                  $ air cell c9
510  6 -3         210 -211 -30                     $ air cell a10
610  6 -3         210 -211 30 -60                  $ air cell b10
110  6 -3         210 -211 60 -20                  $ air cell c10
```

```
511   6 -3          211 -212 -30                    $ air cell a11
611   6 -3          211 -212 30 -60                 $ air cell b11
111   6 -3          211 -212 60 -20                 $ air cell c11
512   6 -3          212 -213 -30                    $ air cell a12
612   6 -3          212 -213 30 -60                 $ air cell b12
112   6 -3          212 -213 60 -20                 $ air cell c12
513   6 -3          213 -214 -30                    $ air cell a13
613   6 -3          213 -214 30 -60                 $ air cell b13
113   6 -3          213 -214 60 -20                 $ air cell c13
514   6 -3          214 -215 -30                    $ air cell a14
614   6 -3          214 -215 30 -60                 $ air cell b14
114   6 -3          214 -215 60 -20                 $ air cell c14
515   6 -3          215 10.3 -30                    $ air cell a15
615   6 -3          215 10.3 30 -60                 $ air cell b15
115   6 -3          215 10.3 60 -20                 $ air cell c15
521   1 -0.001124   -10.3 -10.2 -30 #300 #301       $ environment, air
621   1 -0.001124   -10 -14 30                      $ environment, air
721   1 -0.001124   -13 14                          $ environment, air
821   1 -0.001124   -12 13                          $ environment, air
121   1 -0.001124   -10 12                          $ environment, air
300   1 -0.001124   31 -32 -30                      $ converter 40cm
301 like 300 but trcl (0 0 -10)                     $ converter 30cm
c ------------------------------------------------------------------------------

c --SURFACES-----------------------------------------------------------------
20 cz 2.5                                           $ bsa shape
30 cz 0.2                                           $ converter shape
60 cz 0.5                                           $ source shape (Be target
10 trc 0 0 30  0 0 11.5761  2.5  0.21               $ environment cone
12 trc 0 0 30  0 0 11.5761  2.0  0.21               $ environment cone 2
13 trc 0 0 30  0 0 11.5761  1.0  0.21               $ environment cone 3
14 trc 0 0 30  0 0 11.5761  0.5  0.21               $ environment cone 4
11 pz -0.001                                        $ environment start
201 pz  0.001                                       $ bsa, start
202 pz  2                                           $ bsa
203 pz  4                                           $ bsa
204 pz  6                                           $ bsa
205 pz  8                                           $ bsa
206 pz  10                                          $ bsa
207 pz  12                                          $ bsa
208 pz  14                                          $ bsa
209 pz  16                                          $ bsa
```

```
210 pz   18                                                    $ bsa
211 pz   20                                                    $ bsa
212 pz   22                                                    $ bsa
213 pz   24                                                    $ bsa
214 pz   26                                                    $ bsa
215 pz   28                                                    $ bsa
31 pz   41.476                                                 $ converter start
32 pz   41.576                                                 $ converter end
c ------------------------------------------------------------------------------

mode n p
c --MATERIALS-----------------------------------------------------------------
c --Aria---------
m1 6000.70c .000125 7014.70c .6869 8016.70c .301248 18000.35c .011717
c --BSA----------
c ALF3 + 3% Lithium-7 fluoruro di alluminio litiato sinterizzato (d=3)
m6         13027.70c  -30.880
           9019.70c   -66.600
           3006.60c   -0.189   $ Li-6
           3007.60c   -2.331   $ Li-7

[...]

c --TALLY--------------------------------------------------------------------
f3001:n 31
fc3001 tally f1, neutron current over the converter surfaces, at 40cm
f3011:n 301031
fc3011 tally f1, neutron current over the converter surfaces, at bsa end
f3002:n 31
fc3002 tally f2, neutron flux through the converter sensitive area, at 40
f3012:n 301031
fc3012 tally f2, neutron flux through the converter sensitive area, bsa e
f3004:n 300
fc3004 tally f4, neutron flux in the converter volume, at 40cm
f3014:n 301
fc3014 tally f4, neutron flux in the converter volume, at bsa end
c ------------------------------------------------------------------------------

[...]

c --Variance reduction-------------------------------------------------------
imp:n 0 1 0.5m 0.5m
```

```
       8m 0.5m 0.5m
       8m 0.5m 0.5m
       8m 0.5m 0.5m
       8m 0.5m 0.5m
       8m 0.5m 0.5m
       8m 0.5m 0.5m
       8m 0.5m 0.5m
       8m 0.5m 0.5m
       8m 0.5m 0.5m
       8m 0.5m 0.5m
       8m 0.5m 0.5m
       8m 0.5m 0.5m
       8m 0.5m 0.5m
       8m 0.5m 0.5m
       8m 0.5m 0.5m
       8m 0.5m 0.5m 0.5m 0.5m 16m 1r
imp:p 0 1 54r
```

B.2 Neutron source

```
c --SOURCE-------------------------------------------------------------------
c ************************
c Neutron source Be-9(p,n) (see heading for reference)
c beam energy = 5 MeV
c yielding emission directions : 120 , 100 , 90 , 80 , 60 , 40 , 20 ,0
c Yield reported in neutron/(sr*microC)
c Parabolic distribution (si1,sp1) along X axis of absolute ref system
c ************************
c
sdef pos 0 0 0 vec=0 0 1 dir=d4 erg fdir =d5
c ----------------------------------------------------------------------------
c ----------------------------------------------------------------------------
c 130 120 110 100 95 90 85 80
si4 A -0.6428 -0.5 -0.342 -0.17365 -0.087156 0 0.087156 0.17365
      0.342 0.5 0.6428 0.766 0.866 0.9397 0.98481 1
c 70 60 50 40 30 20 10 0
c
c yileding direction probability (% total )
c 130 120 110 100 95 90 85 80
sp4   5.6151097499 5.5640632976 5.5130168453 5.4619703931 5.3088310362
      5.1556916794 5.1301684533 5.1046452272 4.8494129658 4.5941807044
      5.6661562021 6.7381316998 7.6569678407 8.5758039816 9.213884635
```

```
      9.8519652884
c 70 60 50 40 30 20 10 0
c
c source spectra in 8 yileding directions
c
ds5 S 31 31 32 32 33 33 34 34 35 35 36 36 37 37 38
c
c energy bin ( MeV ) and yielding
c
c ------------------------------------------------------
si31 A     0.298 0.328 0.358 0.391 0.426 0.464 0.503
           0.543 0.585 0.627 0.67 0.714 0.758 0.802
           0.847 0.891 0.936 0.982 1.027 1.074 1.12
           1.166 1.212 1.259 1.306 1.353 1.4 1.448
           1.495 1.542 1.59 1.638 1.685 1.733 1.781
           1.829 1.877 1.925 1.973 2.021 2.069 2.118
sp31       114600 90240 99160 117300 125500 132300 129900
           129300 127900 125300 121900 117900 114100 111200
           110000 110800 113000 115900 118200 121000 123800
           127300 131700 137700 144300 151300 158700 166500
           172700 177000 178900 177700 173100 165500 152700
           132300 106400 78360 51220 27620 9915 170.783
si32 A     0.298 0.328 0.358 0.391 0.426 0.464 0.503
           0.543 0.585 0.627 0.67 0.714 0.758 0.802
           0.847 0.891 0.936 0.982 1.027 1.074 1.12
           1.166 1.212 1.259 1.306 1.353 1.4 1.448
           1.495 1.542 1.59 1.638 1.685 1.733 1.781
           1.829 1.877 1.925 1.973 2.021 2.069 2.118
           2.166 2.214 2.263 2.311
sp32       38440 30970 71370 120000 148300 148800 147900
           144700 141400 137000 130800 124100 118300 114000
           111500 110800 111500 112800 113500 114500 115400
           116000 116800 118400 120200 121700 122600 123700
           124200 124400 124900 125900 126700 127900 128300
           127900 126100 122500 115800 103600 85980 65280
           43680 24090 8909 119.127
si33 A     0.263 0.297 0.331 0.37 0.411 0.454 0.499
           0.545 0.592 0.639 0.687 0.736 0.785 0.834
           0.883 0.933 0.983 1.034 1.084 1.135 1.185
           1.237 1.288 1.339 1.391 1.442 1.494 1.546
           1.598 1.65 1.702 1.754 1.806 1.858 1.91
           1.963 2.015 2.067 2.12 2.172 2.225 2.277
```

```
          2.33 2.383 2.435
sp33      51530 48330 74410 102900 115500 127600 133000
          133600 131700 128600 124700 120800 117400 114700
          113000 111900 110600 109400 108400 107700 107200
          107400 107900 108400 108800 108600 108200 108000
          107700 107500 106900 106000 104500 102800 100500
          97220 91520 84190 74040 61470 47220 32570
          18750 8621 1594
si34 A    0.298 0.328 0.358 0.391 0.426 0.464 0.503
          0.543 0.585 0.627 0.67 0.714 0.758 0.802
          0.847 0.891 0.936 0.982 1.027 1.074 1.12
          1.166 1.212 1.259 1.306 1.353 1.4 1.448
          1.495 1.542 1.59 1.638 1.685 1.733 1.781
          1.829 1.877 1.925 1.973 2.021 2.069 2.118
          2.166 2.214 2.263 2.311 2.359 2.408 2.456
          2.505 2.554
sp34      158000 126100 168400 177000 166400 151600 138900
          128000 119200 113000 109000 106200 104700 104200
          104300 104400 104300 103800 103200 103100 103000
          102700 102100 101000 99300 97370 95310 93220
          91060 89060 87150 85240 83360 81900 80420
          78790 76890 74750 72540 70120 66770 62240
          56430 49410 41120 32080 23130 14920 7958
          2861 57.499
si35 A    0.298 0.328 0.358 0.391 0.426 0.464 0.503
          0.543 0.585 0.627 0.67 0.714 0.758 0.802
          0.847 0.891 0.936 0.982 1.027 1.074 1.12
          1.166 1.212 1.259 1.306 1.353 1.4 1.448
          1.495 1.542 1.59 1.638 1.685 1.733 1.781
          1.829 1.877 1.925 1.973 2.021 2.069 2.118
          2.166 2.214 2.263 2.311 2.359 2.408 2.456
          2.505 2.554 2.602 2.651 2.699 2.748 2.797
sp35      129600 103700 137700 152700 167000 163600 161600
          156100 147800 137200 125500 117300 111900 106600
          102500 99910 98460 97630 96750 95970 95070
          93970 92570 90720 88310 85420 82210 78820
          75300 71730 68210 64820 61510 58400 55610
          53160 51130 49280 47590 46060 44680 43550
          42440 41530 40680 39570 37860 34730 30330
          25240 19760 14260 9224 4932 1779 35.616
si36 A    0.298 0.328 0.358 0.391 0.426 0.464 0.503
          0.543 0.585 0.627 0.67 0.714 0.758 0.802
```

```
            0.847 0.891 0.936 0.982 1.027 1.074 1.12
            1.166 1.212 1.259 1.306 1.353 1.4 1.448
            1.495 1.542 1.59 1.638 1.685 1.733 1.781
            1.829 1.877 1.925 1.973 2.021 2.069 2.118
            2.166 2.214 2.263 2.311 2.359 2.408 2.456
            2.505 2.554 2.602 2.651 2.699 2.748 2.797
            2.845 2.894 2.942 2.991
sp36        205800 165700 263000 318200 285700 257000 223400
            211400 198900 181300 163100 149100 134400 122000
            111900 104800 99920 96550 93870 91640 89650
            87800 86070 84540 83100 81650 80080 78430
            76640 74840 73120 71460 69840 68480 67350
            66440 65790 65440 65320 65630 66600 68330
            70330 72880 76400 80650 85440 90830 95620
            100200 103100 103600 100100 90670 76600 59140
            40280 22660 8370 52.247
si37 A      0.298 0.328 0.358 0.391 0.426 0.464 0.503
            0.543 0.585 0.627 0.67 0.714 0.758 0.802
            0.847 0.891 0.936 0.982 1.027 1.074 1.12
            1.166 1.212 1.259 1.306 1.353 1.4 1.448
            1.495 1.542 1.59 1.638 1.685 1.733 1.781
            1.829 1.877 1.925 1.973 2.021 2.069 2.118
            2.166 2.214 2.263 2.311 2.359 2.408 2.456
            2.505 2.554 2.602 2.651 2.699 2.748 2.797
            2.845 2.894 2.942 2.991 3.04 3.089 3.138
sp37        99170 79918.8 128122 214508 235282 226634 235564
            236598 228044 212628 192042 169764 150306 134984
            123892 116466 111108 106596 102366 98230 94376
            90644.2 87344.8 84543.6 82212.4 80266.6 78781.4 77879
            77409 77333.8 77672.2 78386.6 79411.2 80990.4 82992.6
            85474.2 88557.4 92289.2 96350 100768 105374 110450
            115902 121918 129062 136206 143538 151904 159800
            168354 177002 183206 187342 185368 177472 161398
            138368 111390 82438 54491.8 29816.8 10922.8 213.6432
si38 A      0.298 0.328 0.358 0.391 0.426 0.464 0.503
            0.543 0.585 0.627 0.67 0.714 0.758 0.802
            0.847 0.891 0.936 0.982 1.027 1.074 1.12
            1.166 1.212 1.259 1.306 1.353 1.4 1.448
            1.495 1.542 1.59 1.638 1.685 1.733 1.781
            1.829 1.877 1.925 1.973 2.021 2.069 2.118
            2.166 2.214 2.263 2.311 2.359 2.408 2.456
            2.505 2.554 2.602 2.651 2.699 2.748 2.797
```

```
           2.845 2.894 2.942 2.991 3.04 3.089 3.138
           3.186
sp38       84790 69520 237900 266000 270600 266900 256700
           254800 227700 189200 165800 141800 128800 120100
           115100 113100 111400 109700 107700 105300 102500
           98950 95270 91980 89420 87450 85840 84580
           83640 83290 83850 85270 87270 90110 93570
           97560 101900 106500 111200 116200 121900 129000
           136500 145100 155100 165600 177400 190400 202600
           215100 226400 234000 238700 237300 229000 210000
           183100 152200 118900 86040 55620 29810 10640
           21.166
c ****************
c sdef end
c ****************
```

B.3 Energy bins

Listings of the two energy binning used for the simulations carried out in this thesis.

B.3.1 Uniform energy bins

```
c --ENERGY BINS-----------------------------------------------------------------
# e0
1E-06
2E-06
3E-06
4E-06
5E-06
6E-06
7E-06
8E-06
9E-06
1E-05
2E-05
3E-05
4E-05
5E-05
6E-05
7E-05
8E-05
9E-05
```

1E−04
2E−04
3E−04
4E−04
5E−04
6E−04
7E−04
8E−04
9E−04
1E−03
2E−03
3E−03
4E−03
5E−03
6E−03
7E−03
8E−03
9E−03
0.01
0.04
0.08
0.12
0.16
0.2
0.24
0.28
0.32
0.36
0.4
0.44
0.48
0.52
0.56
0.6
0.64
0.68
0.72
0.76
0.8
0.84
0.88
0.92

```
0.96
1
1.04
1.08
1.12
1.16
1.2
1.24
1.28
1.32
1.36
1.4
1.44
1.48
1.52
1.56
1.6
1.64
1.68
1.72
1.76
1.8
1.84
1.88
1.92
1.96
2
2.04
2.08
2.12
2.16
2.2
2.24
2.28
2.32
2.36
2.4
2.44
2.48
2.52
2.56
2.6
```

```
2.64
2.68
2.72
2.76
2.8
2.84
2.88
2.92
2.96
3
3.04
3.08
3.12
3.16
3.2
3.24
3.28
3.32
3.36
3.4
3.44
3.48
3.52
3.56
3.6
3.64
3.68
3.72
3.76
3.8
3.84
3.88
3.92
3.96
4
c ---------------------------------------------------------------------
```

B.3.2 Energy bins per decades

```
c ----Energy bins---------------------------------------------------------
# e0
1.00E-10
1.26E-10
```

1.59E−10
2.00E−10
2.51E−10
3.16E−10
3.98E−10
5.01E−10
6.31E−10
7.94E−10
1.00E−09
1.26E−09
1.59E−09
2.00E−09
2.51E−09
3.16E−09
3.98E−09
5.01E−09
6.31E−09
7.94E−09
1.00E−08
1.26E−08
1.59E−08
2.00E−08
2.51E−08
3.16E−08
3.98E−08
5.01E−08
6.31E−08
7.94E−08
1.00E−07
1.26E−07
1.59E−07
2.00E−07
2.51E−07
3.16E−07
3.98E−07
5.01E−07
6.31E−07
7.94E−07
1.00E−06
1.26E−06
1.59E−06
2.00E−06

2.51E−06
3.16E−06
3.98E−06
5.01E−06
6.31E−06
7.94E−06
1.00E−05
1.26E−05
1.59E−05
2.00E−05
2.51E−05
3.16E−05
3.98E−05
5.01E−05
6.31E−05
7.94E−05
1.00E−04
1.26E−04
1.59E−04
2.00E−04
2.51E−04
3.16E−04
3.98E−04
5.01E−04
6.31E−04
7.94E−04
1.00E−03
1.26E−03
1.59E−03
2.00E−03
2.51E−03
3.16E−03
3.98E−03
5.01E−03
6.31E−03
7.94E−03
1.00E−02
1.26E−02
1.59E−02
2.00E−02
2.51E−02
3.16E−02

```
3.98E-02
5.01E-02
6.31E-02
7.94E-02
1.00E-01
1.26E-01
1.59E-01
2.00E-01
2.51E-01
3.16E-01
3.98E-01
5.01E-01
6.31E-01
7.94E-01
1.00E+00
1.26E+00
1.59E+00
2.00E+00
2.51E+00
3.16E+00
3.20E+00
c ------------------------------------------------------------------------------
```

Appendix C

Weight Windows

The weight window is a space-energy-dependent splitting and Russian roulette technique [15]. Figure C.1 shows a schematic of the weight window technique. Desired

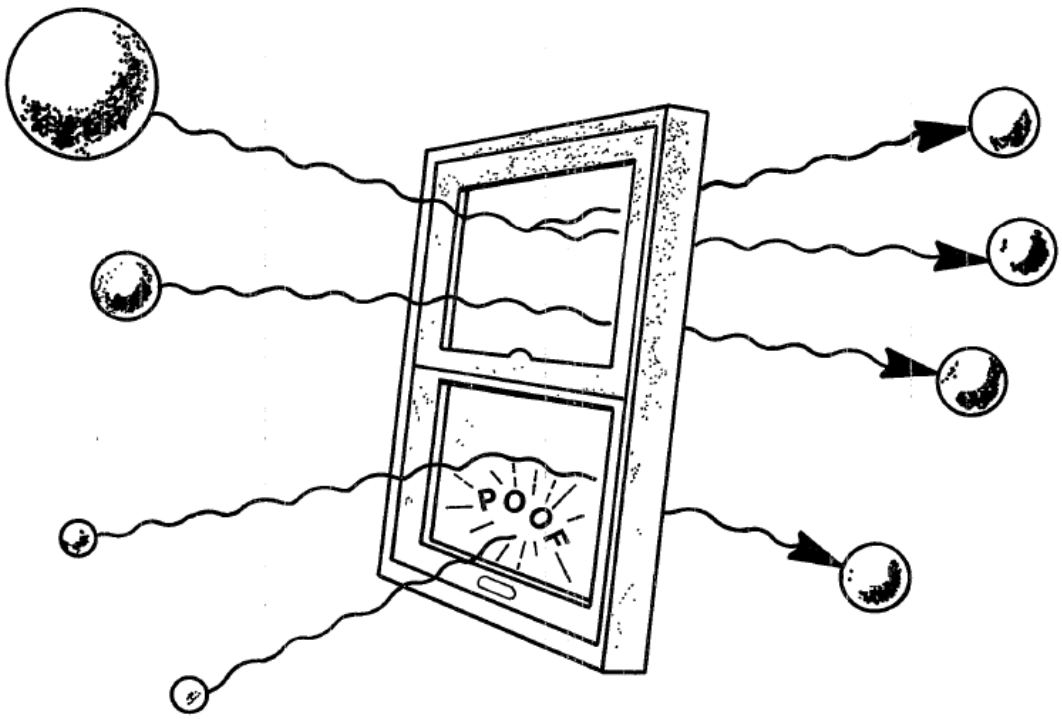

Figure C.1. The weight window technique. [15]

energy interval are defined and for each space cell for each energy interval a window of acceptable weight is defined. The principle of weight window is very simple.

Tracks entering a phase-space cell with weight within the window bounds pass through the windows without any action. Instead if a particle is below the lower weight bound, Russian roulette is played: following the same principle as for the geometric Russian roulette, the particle is either terminated or its weight is increased to be within the window. If the track weight is above the upper bound, the particle is split so that all the split particles are within the window.
Three weights must be defined to correctly perform this variance reduction technique:

- the lower weight bound W_L
- the survival weight for particles playing Russian roulette W_S, through the definition of a constant C_S such that $W_S = C_S W_L$
- the upper weight bound W_U, through the definition of a constant C_U such that $W_U = C_S W_L$

The technique works with a similar principle with respect to the geometry splitting and Russian roulette. The two main advantages are the fact that weight window is space-energy dependent whilst geometry splitting is only space dependent and the fact that weight window can control weight fluctuations introduced by other biasing techniques whereas geometry splitting preserve any weight fluctuation because it is weight independent. Weight window is therefore more appropriate to use if also other biasing techniques are used.